

**A Theoretical Study**  
**on Electronic Structures and Optical Absorption Spectra**  
**of II-VI Semiconductor Strained-Layer Superlattices**

**Satoshi Hohnoki**

**Course of Industrial Science**  
**Graduate School of Science and Technology**  
**Niigata University**

# Contents

<b>1</b>	<b>Introduction</b>	<b>1</b>
1.1	General introduction . . . . .	1
1.2	II-VI strained-layer superlattices consisting of ZnSe, ZnS and ZnTe . . . . .	6
<b>2</b>	<b>Superlattice</b>	<b>11</b>
2.1	Kind of superlattice . . . . .	11
2.2	Strained-layer superlattice . . . . .	13
2.2.1	Mismatch and critical thickness . . . . .	13
<b>3</b>	<b>Electronic Structures for the Strained-Layer Superlattices</b>	<b>18</b>
3.1	Strain effect . . . . .	18
3.2	Electronic structure of the conduction band . . . . .	23
3.3	Electronic structure of the valence band . . . . .	25
<b>4</b>	<b>Theory of Optical Absorption</b>	<b>27</b>
<b>5</b>	<b>Electronic Structures and Absorption Spectrum of ZnSe(27Å)-ZnS(27Å) Strained-Layer Superlattice</b>	<b>31</b>
5.1	Introduction . . . . .	31
5.2	Results for the electronic structures . . . . .	32
5.3	Total absorption spectra . . . . .	34
5.4	Analysis of each transition . . . . .	39

5.5	Dependence on the polarization . . . . .	44
5.6	Conclusions . . . . .	47
<b>6</b>	<b>Electronic Structures and Absorption spectrum of ZnTe(10Å)-ZnSe(10Å) Strained-Layer Superlattice</b>	<b>48</b>
6.1	Introduction . . . . .	48
6.2	Results for the electronic structures . . . . .	49
6.3	Total absorption spectra . . . . .	52
6.4	Dependence on the polarization and analysis of each transition . . . . .	52
6.5	Conclusions . . . . .	59
<b>7</b>	<b>Calculated Results for Absorption Spectra of ZnSe(22Å)-ZnS(23Å) Strained-Layer Superlattice and Comparison with Experiment</b>	<b>61</b>
7.1	Introduction . . . . .	61
7.2	Results for the electronic structures . . . . .	62
7.3	Absorption spectra . . . . .	64
7.4	Conclusions . . . . .	69
<b>8</b>	<b>Calculated Results for Absorption Spectra of Type I ZnSe(20Å)- ZnS(20Å) and Type II ZnTe(20Å)-ZnSe (20Å) Strained-Layer Su- perlattice</b>	<b>70</b>
8.1	Introduction . . . . .	70
8.2	Results for the electronic structures . . . . .	72
8.3	Characteristic differences between absorption spectra of Type I and Type II strained-layer superlattice . . . . .	78
8.4	Dependence on the incident-photon polarization . . . . .	83
8.5	Conclusions . . . . .	84

<b>9</b>	<b>Conclusions</b>	<b>85</b>
	<b>Appendix</b>	<b>90</b>
A	Formalism of optical absorption coefficient . . . . .	90
	<b>Acknowledgments</b>	<b>97</b>
	<b>References</b>	<b>98</b>

# Chapter 1 Introduction

## 1.1 General introduction

The semiconductor superlattice which has a one-dimensional periodic structure consisting of alternating ultra-thin layers was proposed and constructed in 1969-1970 by Esaki and Tsu.<sup>1,2)</sup> They proposed the superlattice to examine the possibility of resonant tunnelling which arises from the interaction of electron waves in potential barriers.<sup>3)</sup> On account of the birth of this new man-made semiconductor superlattice, we had come to be able to control the period of this material which is determined by the thickness of well and barrier layers. The important property of this material is as follows. This new man-made material can be controlled so as to have the thickness of a well layer which is comparable to the de Broglie wavelength and, therefore, gives us very interesting quantum properties (i.e. quantum size effects). Accordingly, when the superlattice has the thickness of a well layer which is comparable to the de Broglie wavelength, the characteristic dimension along the growth direction of a superlattice is reduced, and the entire electron system turns into a quasi-two-dimensional system with the assumption of the presence of ideal interfaces. Here the de Broglie wavelength  $\lambda$  is calculated by the equation,  $\lambda = h(2m^*E)^{-\frac{1}{2}}$ , and becomes 123Å for electrons with an energy  $E$  of 0.1eV and an effective mass  $m^*$  of  $0.1m_0$ , where  $h$  is Planck's constant and  $m_0$  is the free-electron mass.

After Esaki and Tsu's proposal<sup>1,2)</sup> of semiconductor superlattices, many early experimental studies on various properties such as the electron tunnelling,<sup>4-6)</sup> the electrical transport,<sup>7,8)</sup> the interband optical absorption,<sup>9-12)</sup> and the Raman scatterings<sup>13,14)</sup> were carried out in this new field.

As for the electron tunnelling, Tsu and Esaki firstly computed the tunnelling transmission coefficient in multibarrier structure as a function of the electron energy, and derived the current-voltage characteristics.<sup>4)</sup> This multibarrier tunneling model provided a useful insight into the transport mechanism. Chan, Esaki and Tsu subsequently succeeded in observing resonant tunnelling in double barriers,<sup>5)</sup> and Esaki and Tsu measured quantum transport properties for a superlattice.<sup>6)</sup>

Chan *et al.* reported the first observation of the Shubnicov-de Haas effect in GaAs-Ga<sub>1-x</sub>Al<sub>x</sub>As superlattices with the current flowing in the plane of layers.<sup>7)</sup> The superlattice provides an opportunity of controlling the Fermi surfaces by changing the energy and bandwidth of the subbands which is determined by the barrier and the well thicknesses as well as the barrier height. The observed oscillations show the electronic subband structure, which becomes increasingly to have the two-dimensional property as the bandwidth is narrowed.

Optical absorption spectra were observed by Dingle *et al.*<sup>9,10)</sup> They revealed the structures in the optical absorption spectra observed in isolated<sup>9)</sup> and coupled<sup>10)</sup> quantum wells. For the former, GaAs well widths in the range between 70Å and 500Å were prepared. The GaAs wells were separated by Ga<sub>1-x</sub>Al<sub>x</sub>As barriers which were normally thicker than 250Å. In low-temperature measurements for such structures, several exciton peaks which are associated with bound-electron states and bound-hole states in the quantum well were resolved. For the latter study, superlattices which consist of GaAs well widths in the range between 50Å and 200Å and Ga<sub>1-x</sub>Al<sub>x</sub>As (0.19 <  $x$  < 0.27) barrier widths between 12Å and 18Å were grown by molecular beam epitaxy (MBE) on GaAs substrates. The spectra at low temperatures clearly indicated resonantly discrete states in the vicinity of the absorption edge.

As for Raman scatterings, Manuel *et al.*<sup>13)</sup> reported the observation of enhancement in the Raman cross section for photon energies near electronic resonance in

GaAs-Ga<sub>1-x</sub>Al<sub>x</sub>As superlattice of a variety of configurations. Both the energy positions and the general shape of the resonant curves agree well with the theory taking account of the two-dimensional quantum states in such superlattices.

In the last few years we have witnessed great progress towards a better evaluation of the complex physical situations found in these man-made semiconductor superlattices. The superlattices are now grown to meet specific device requirements. The application to devices, however, was restricted, because the early experiments of superlattice concentrated almost on III-V compound semiconductors, and the physical properties were explicated only for such materials. As superlattices have been found to be applicable to a variety of devices, we need to examine also the properties of other semiconductor compounds. Especially we pay attention to the optical properties, and think of the materials having the optical spectra in the blue-green spectral regions.

Advances of the control technique for optical devices changed our life environment drastically. Especially, optical devices affected our life largely. They are long-distance fibre-optic communications, laser printers and compact disk players which all depend on the optical device technology i.e. the semiconductor laser. These efficient materials are based on Si, GaAs and other III-V compounds related with GaAs. As they operate at infrared and red wavelengths, we cannot use these semiconductors as the optical devices in the blue-green spectral regions. But the physicists, materials scientists, and electrical engineers in 1960's have tried to find semiconductors with shorter visible wavelengths, since such semiconductors have many possible applications for light-emitting diodes (LEDs) and compact lasers in the blue-green spectral regions.<sup>15,16)</sup> These studies brought recent proposals as follows: high-density optical memories and display devices, medical diagnostics, communications through seawater, *etc.*

The materials which are most likely to emit light with such short wavelengths were

direct-bandgap II-VI compound semiconductors. II-VI compound semiconductors are unique and interesting materials with respect to their optical properties as compared to those of III-V compounds because of the large energy scale provided by their fundamental optical gap ranging from zero for CdHgTe to 3.5eV for ZnS at room temperature (RT). Especially ZnS, ZnSe and ZnTe are expected to be useful materials for blue LEDs and short wavelength lasers<sup>17-23)</sup> because of their wide bandgaps at RT which are 3.5, 2.7 and 2.3eV, respectively.

The original concept to realize the applications to visible-light optical devices was to use the direct-bandgap recombination in those II-VI semiconductors. However, semiconductors in this system had had two principal problems i.e. achieving electrical control of the semiconductors by doping, and removing the impurity state which exists within the bandgap due to impurities and defects. As for the problem of doping, though it was easy to make some compounds p-type (such as ZnTe) and others n-type (ZnSe, ZnS), it was impossible to obtain low electrical resistivity in both polarities of a given compound, so that the formation of the p-n junction was difficult. The existence of impurity state obstructs to emit light with short wavelengths, and the problem of the doping also often directly contributed to the impurity state. To avoid these difficulties, our attention came to be attracted to the growth of superlattices in this system.

Novel growth techniques such as MBE and metalorganic vapour phase epitaxy (MOVPE) made progress to be successfully extended to the growth of II-VI strained-layer superlattices (SLSs) and quantum wells (QWs). Growth of the CdTe-HgTe superlattice by MBE was first achieved in 1982,<sup>24,25)</sup> and, as for the growth of materials with a wide gap, ZnSe-ZnS superlattices which were grown by using hot-wall epitaxy were reported in 1984.<sup>26)</sup> II-VI compound semiconductors started to be proposed as a superlattice and QW devices to realize many applications stated above and

other wide ability in relation to quantum states (i.e. blue LEDs, injection lasers and photodetectors based on quantum well). The advances<sup>15-30)</sup> of growth technology such as MBE and MOVPE for this system now allow the growth of high-quality heterostructures and superlattices with background impurities reduced in the range from  $10^{14}\text{cm}^{-3}$  to  $10^{15}\text{cm}^{-3}$  and doping levels ranging from mid  $10^{17}\text{cm}^{-3}$  to low  $10^{18}\text{cm}^{-3}$  using plasma sources, and lead to realization of p-n junction lasers in the blue-green spectrum as demonstrated by Hasse *et al.*<sup>29)</sup> of 3M and other groups.<sup>30)</sup>

II-VI SLSs have not only visible energy gap but also large strain effect. In strained-layer structures, the II-VI compound semiconductor SLSs consist primarily of different two materials which have lattice mismatches of above 4.5% and a critical layer thickness that approaches atomic dimensions. The strain effect resulting from lattice-mismatched materials offers advantages that do not exist in lattice-matched materials. These advantages are the splitting of the degenerate hole bands, the transfer of the impurity state due to impurities and defects outside the bandgap, *etc.* By using these properties positively, we will come to be able to design novel and unique optoelectronic devices which cover the visible and ultraviolet spectral regions. Accordingly, new possibilities resulting from II-VI SLSs have been opened up for new optoelectronics devices with large strains which cannot be prepared from III-V superlattices. However, except for wide optical gap and large strain in II-VI SLSs, fundamental electronic energy band structures for superlattice resemble those for III-V superlattices. In general, like III-V superlattices, II-VI SLSs are divided into three categories, type I, type II and type III, which correspond typically to ZnSe-ZnS, ZnTe-ZnSe and CdTe-HgTe, respectively. We account for the difference between these types in Chap. 2.

As the growth technologies such as MBE and MOVPE for II-VI SLSs advance, the basic research for the optical properties of excitons and the control of conductiv-

ity in both the wide gap and narrow gap materials has also advanced significantly. Especially, physical properties understood by optical experiments have been deeply explored by many scientists, and many interesting results for the optical absorption including exciton effects, photoluminescences, Raman scattering, *etc.* are now being accumulated.

## 1.2 II-VI strained-layer superlattices consisting of ZnSe, ZnS and ZnTe

The development of the recent crystal growth techniques such as MBE and MOVPE has successfully made it possible to grow II-VI SLSs. Since II-VI SLSs have characteristic optical gaps which can be controlled from zero to the region of ultraviolet, they are expected to provide unique quantum devices in comparison with III-V superlattices. Especially, an attention has been attracted to their application to optoelectronic devices in the blue-green spectral regions. To examine the aptitude for optoelectronic devices, many optical experiments have been carried out,<sup>31-44)</sup> and many interesting physical properties have been revealed. Theoretical studies which were accompanied by such experimental studies, therefore, also started to be reported.<sup>45-51)</sup> In these optical studies, experiments on the optical absorption which faithfully reflects the two-dimensional density of states and electronic structures play a very important role to explore the fundamental electronic structures and physical processes. For the future application, it is important to study optical absorption spectra and explore their origins theoretically.

The purpose of this thesis is to construct a reliable theoretical method for an investigation of the optical absorption spectrum of new SLSs on the basis of a detailed knowledge on electronic structures. The electronic structure is derived within

the framework of an effective-mass approximation, and the absorption spectrum is calculated by taking the dependence of the transition matrix on the wave vector  $\mathbf{k}$  fully into account. To investigate an efficacy of our theory, we apply it to typical new SLSs of type I and type II in this thesis.

Recently, the absorption spectra of ZnSe-ZnS and ZnTe-ZnSe SLSs which consist of II-VI semiconductors and belong to type I and type II superlattices, respectively, have come to be reported. The characters of band structures for these SLSs are explained in Chap. 2. For ZnSe-ZnS SLSs, many optical absorption experiments<sup>31-40)</sup> have been carried out, and some interpretations for the origin of the absorption spectra have been proposed. Since these SLSs have the very small conduction band-offset due to the common-cation rule in contrast to the very large valence band-offset, we have a great interest in the structure of the conduction and valence subbands and the optical absorption which may be influenced by these properties. The absorption spectra have two strong absorption peaks in the vicinity of the fundamental absorption edge, in addition to a few broad bands in the high-energy regime.<sup>35,39,40)</sup> For ZnTe-ZnSe SLSs, though many optical experiments<sup>40-44)</sup> have been carried out, optical absorption experiments are but few, and the work by Shen *et al.*<sup>40)</sup> is notable. The absorption spectrum has been measured at RT, and has been found to consist of a small bump in the low-energy side and a large bump in the high-energy side.<sup>40)</sup>

We carry out the theoretical calculations for ZnSe-ZnS and ZnTe-ZnSe SLSs to explicate these optical properties. A calculation of the electronic structure of the conduction and valence subbands is carried out by using the Luttinger-Kohn Hamiltonian<sup>52,53)</sup> in the Kronig-Penney model, in which the periodic change of the effective mass and the strain in the well and barrier layers is taken into account. The absorption coefficients due to the direct valence-band-to-conduction-band transitions are evaluated by taking the electronic structure fully into account.

To explore the origin of absorption spectra, we decompose the total absorption spectrum into the band-to-band absorption spectra, and pick up main components. The electronic structures are calculated by including the mixing of heavy- and light-hole states. The mixing effects mean that the valence bands which consist mainly of the heavy-hole state and the light-hole state become to contain the light-hole state and the heavy-hole state by the hybridization, respectively, if the wave vector is finite. The absorption spectra are influenced by the mixing effects through the energy dispersion and the overlap of envelope functions in the conduction and valence bands. The energy dispersion influences the absorption spectra, because the band gap varies with  $\mathbf{k}$ . To examine the mixing effects in detail, we take into account the overlap of envelope functions which depends also on  $\mathbf{k}$ .

The band-to-band absorption spectrum consists of two structures which originate from the transitions from the heavy- and light-hole states. Since these structures are different for different incident-photon polarizations, a change of the polarization influences the band-to-band absorption spectrum drastically. We calculate two cases for it, (i.e. transverse electric field ( $TE$ ) and transverse magnetic field ( $TM$ ) in which the electric field vector of incident light is oriented perpendicular to and along the growth direction, respectively), and examine the dependence of the optical absorption on it in detail.

Further, it is expected that the type I and the type II SLSs have different characteristic properties in the absorption spectra, because the band structures of type I and type II SLSs are clearly different, and these absorption spectra reflect the electronic structure very sensitively. Therefore, we also examine and predict the difference between them.

As an application of our theory, we actually calculate the electronic structures and the absorption spectra neglecting excitonic effects for ZnSe(27Å)-ZnS(27Å), ZnTe

(10Å)-ZnSe(10Å) and ZnSe(22Å)-ZnS(23Å) SLSs, and compare theoretical results with experiments by Shen *et al.*<sup>39,40)</sup> and Fan *et al.*<sup>35)</sup> Similar calculations are carried out for ZnSe(27Å)-ZnS(27Å) SLS,<sup>48,49)</sup> ZnTe(10Å)-ZnSe(10Å)<sup>49)</sup> and ZnSe(22Å)-ZnS(23Å)<sup>51)</sup> SLSs at low temperature and at RT, respectively. The calculations at low temperature and at RT are carried out by using the band gaps measured at low temperature and RT for each bulk material, respectively, and on only that particular point these calculations are different each other. For ZnSe(27Å)-ZnS(27Å) SLS,<sup>48,49)</sup> we found that theoretical absorption spectra can explain origins of fine structures in the experimental absorption spectra reasonably well. At low temperatures, however, it is not easy to test the validity of our theoretical results, because the experimental absorption spectra may be influenced by excitonic effects which are not taken into account in our calculation of the absorption spectra.

Though a study on excitonic effects<sup>54–66)</sup> is itself important physics, we want to explore characteristic properties of the optical absorption which originates from the vertical valence-band-to-conduction-band transitions in SLSs without being disturbed by excitonic effects. So, we expect that it can be achieved by carrying out the calculation at RT and comparing theoretical absorption spectra with experimental ones observed at high temperatures where excitonic effects are much reduced. We have already carried out calculations on the type I ZnSe(22Å)-ZnS(23Å) SLS<sup>51)</sup> and type II ZnTe(10Å)-ZnSe(10Å) SLS,<sup>49)</sup> and tried to compare theoretical results with the absorption spectra observed at RT by Fan *et al.*<sup>35)</sup> and Shen *et al.*<sup>40)</sup> As a result, origins of fine structures in the observed absorption spectra can be clarified reasonably well. Thus, we judge that the reliability of our theory is confirmed, so that we next apply it to the prediction of a marked difference between absorption spectra of type I and type II SLSs with the well and barrier layers of the same thickness.

The SLSs for which we calculate absorption spectra are the type I ZnSe(20Å)-

ZnS(20Å) and ZnTe(20Å)-ZnSe(20Å) SLSs whose well and barrier layers have the same thickness. As a result of a detailed analysis, a marked difference is found between absorption spectra in these type I and type II SLSs, and an origin of the main difference can be clarified on the basis of their electronic structures. We also examine the dependence of the absorption spectra on the incident-photon polarization.

Organization of this thesis is as follows. In the next chapter, we explain the kind and the character of superlattices. In Chap. 3, we explain how to calculate the electronic structures of the valence and conduction subbands within the framework of a multiband effective-mass approximation by taking the strain effects into account. In Chap. 4, we describe the calculation of the interband optical absorption spectra. In Chaps. 5~8, results calculated for ZnSe-ZnS and ZnTe-ZnSe SLSs are analyzed in detail. Finally, conclusions are summarized, and new experiments are suggested in Chap. 9.

## Chapter 2 Superlattice

### 2.1 Kind of superlattice

Superlattices are new type of materials which consist of epitaxially grown alternating ultra-thin layers, and have its period less than the electron mean free path. The superlattices which are created by nearly one-dimensional periodic potential are characterized by the presence of many minibands and exhibiting very strong anisotropy. Minibands (or subbands) in superlattice creat new electronic properties such as negative differential conductivity, interband transitions, nonlinearoptical response of conduction electron, fractional quantization of the hall effect *etc.*

In such superlattice, three kinds of superlattices appears due to the difference of the bottom of the conduction band ( $E_c^b$ ) and the top of the valence band ( $E_v^t$ ) between layers. These are shown in Fig. 2.1.

#### 1). type I

Superlattices of this type have that the  $E_c^b$  and the  $E_v^t$  of one semiconductor layer lie inside the energy gap of the other semiconductor layer. (GaAs/AlGaAs, ZnSe/ZnS, *etc.*)

#### 2). type II

Superlattices of this type have that  $E_c^b$  of one semiconductor layer lies in the energy gap of second semiconductor layer while  $E_v^t$  of the latter lies in the energy gap of the first semiconductor layer. (InGaAs/GaSbAs, ZnTe/ZnSe, ZnTe/ZnS *etc.*)

#### 3). type III

Superlattices of this type that  $E_c^b$  of one semiconductor layer lies below  $E_v^t$  of the other semiconductor layer. (InAs/GaAs, CdTe/HgTe, *etc.*)

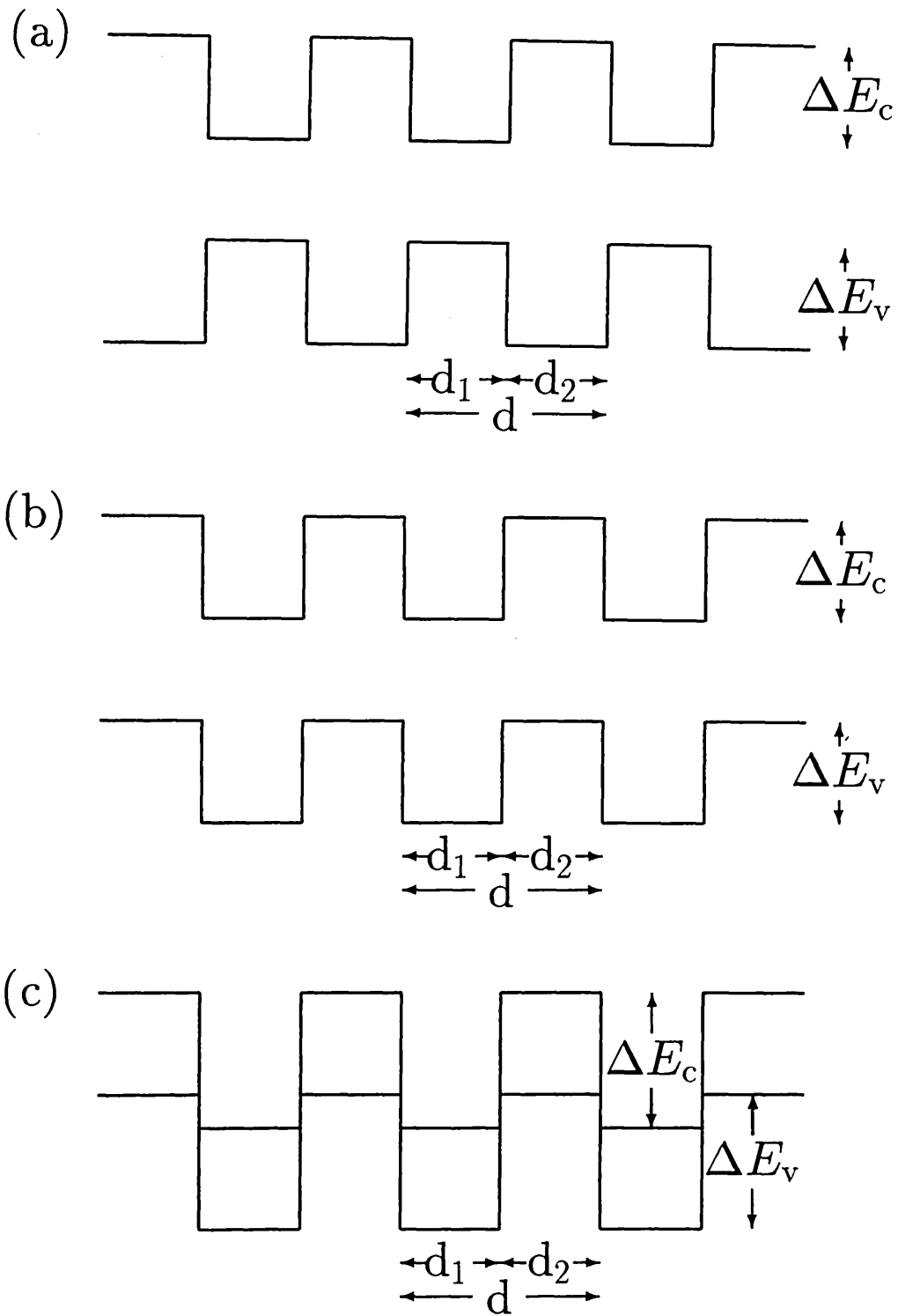


Fig. 2.1. Schematic band diagrams of (a) type I, (b) type II and (c) type III superlattices.

In these types, we show what kinds type I ZnSe-ZnS and type II ZnTe-ZnSe SLSs which we use in this thesis belong to. The schematic band diagrams for type I ZnSe-ZnS and type II ZnTe-ZnSe SLSs which we use in this thesis also are shown in Fig. 2.2. The type I SLS has ZnSe well and ZnS barrier layers in both conduction and valence bands, while the type II SLS has ZnTe barrier and ZnSe well layers in the conduction band, and ZnTe well and ZnSe barrier layers in the valence band. In the type II SLS, ZnTe well in the valence band and ZnSe well in the conduction band do not overlap with each other. Further, ZnSe-ZnS SLSs have very small conduction band offset and very large valence band offset, while ZnTe-ZnSe SLSs have large band offset in both conduction and valence bands.

## 2.2 Strained-layer superlattice

Up to now the most investigated SLS has been made from the less-mismatched semiconductor materials such as Si-SiGe, GaAsP-GaP, InAlAs-InGaAs, ZnSe-ZnS and CdTe-CdMnTe systems etc. The investigations have been concentrated on the growth method, the effect of strain on the thickness of epitaxial layers, the superlattice band structure and zone-folding phenomena. A number of theoretical models have been developed in order to explain particular properties of SLS.

### 2.2.1 Mismatch and critical thickness

For single-layer critical thickness, Mathews and Blakeslee<sup>67)</sup> developed a model for critical layer thickness wherein  $h_c$  is determined by that thickness for which a segment of threading dislocation bows and elongates, under the influence of the misfit stress, to form a segment of interfacial dislocation line. Although in their original work the

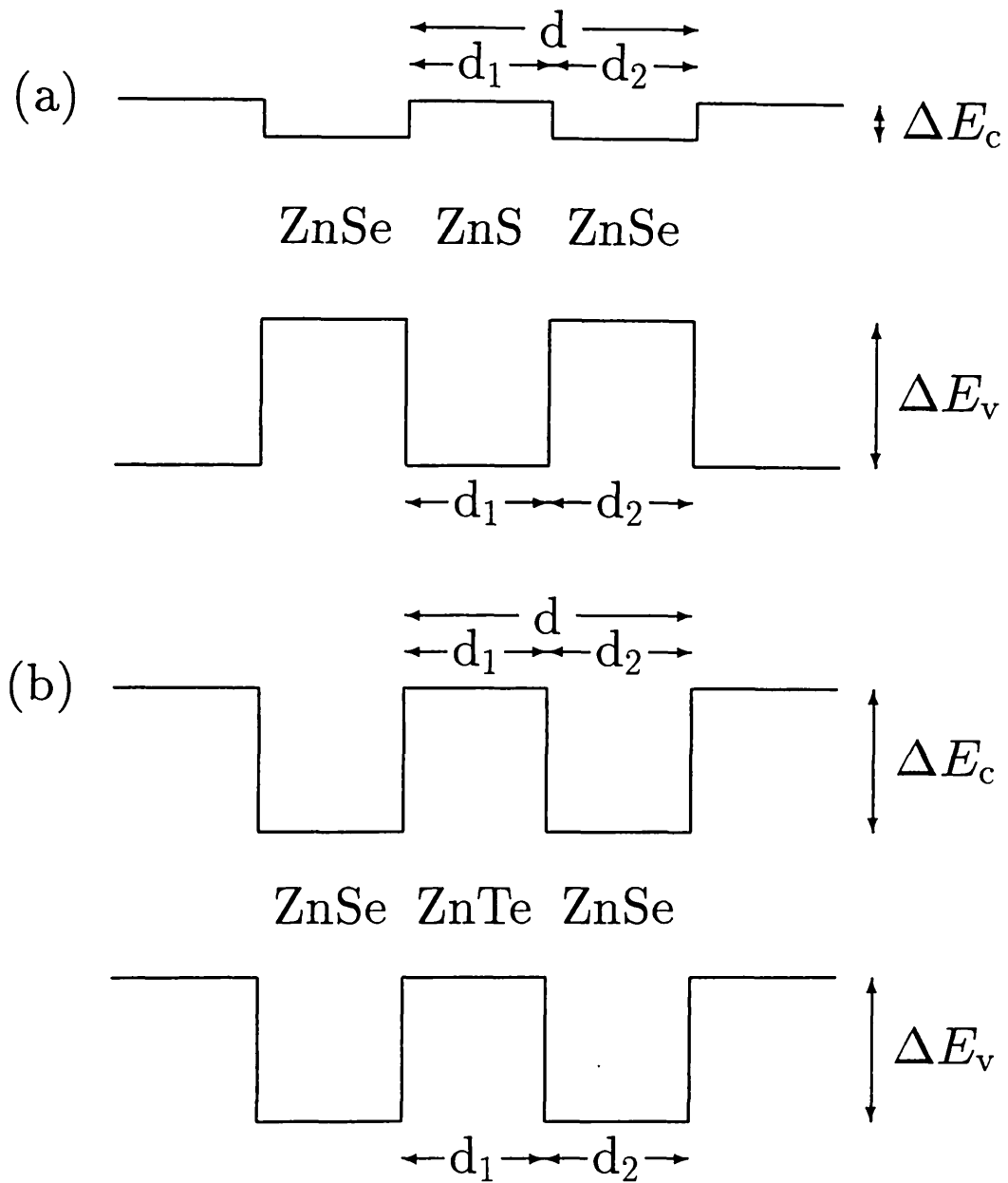


Fig. 2.2. Schematic band diagrams of (a) type I ZnSe-ZnS and (b) type II ZnTe-ZnSe superlattices.  $\Delta E_c$  and  $\Delta E_v$  are conduction and valence barrier potentials, respectively, and  $d$  is the periodicity of superlattice, and  $d_i$  ( $i=1,2$ ) shows the thickness for each layer.

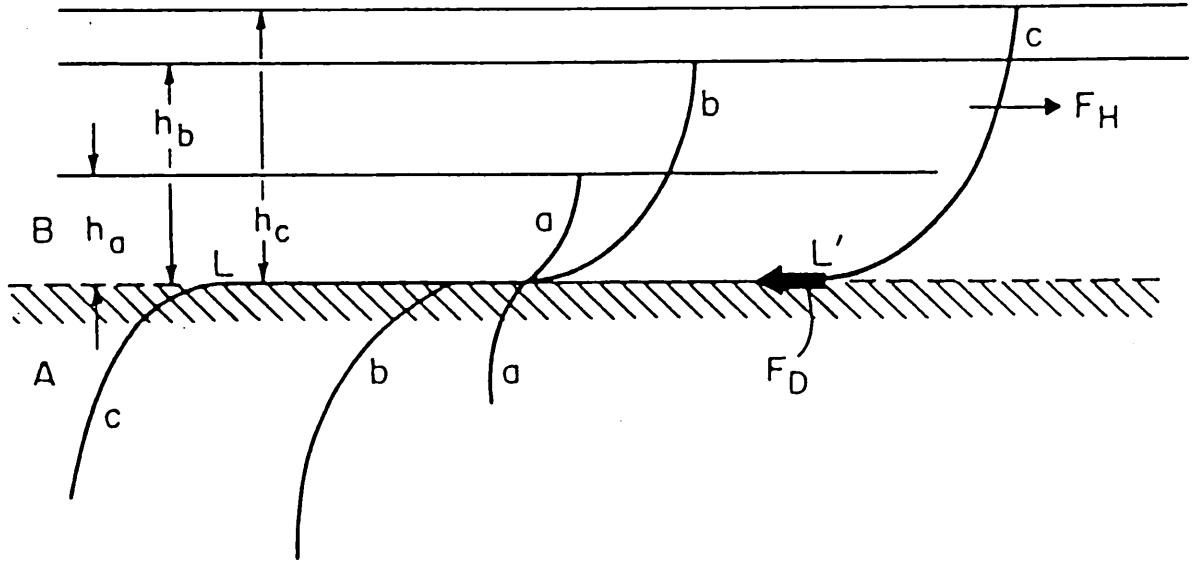


Fig. 2.3. Transformation of a coherent interface to an incoherent interface via the elongation of a pre-existing segment of threading dislocation. Initially the interface is assumed coherent (a). For film thickness  $h_b$ , the interface is critical (i.e.  $F_H = F_D$ ), whereas for film thickness  $h_c$ ,  $F_H > F_D$ , allowing the dislocation to elongate in the interface plane, thereby generating the length  $LL'$  of misfit dislocation line. (ref. 68)

segment of threading dislocation was assumed to be grown in, the analysis applies equally well to threading dislocation segments that may be associated with critical half-loops. The process is illustrated in Fig. 2.3 for the case of a grown-in threading dislocation.<sup>68)</sup> The misfit strain ( $e_{\parallel}$ ) exerts a force  $F_H$  on the threading dislocation, where  $F_H$  is given by

$$F_H = 2G \left( \frac{1+\nu}{1-\nu} \right) b h e_{\parallel} \cos \lambda. \quad (2.1)$$

Where  $\cos \lambda = 0.5$  for  $60^\circ$  dislocations. The tension in the segment,  $LL'$  of the dislocation line, which is generated by the motion of the threading segment, is denoted by

$F_1$ .

$$F_1 = \frac{Gb^2 (1 - \nu \cos^2 \Theta)}{4\pi (1 - \nu)} \left[ 1 + \ln \frac{h}{b} \right], \quad (2.2)$$

where  $\cos^2 \Theta = 0.25$  for  $60^\circ$  dislocations. For single epitaxial layer, the equilibrium critical thickness  $h_c$  is determined by eqs.(2.1) and (2.2). One thus obtains

$$h_c = \left( \frac{b}{f_0} \frac{1 - \nu \cos^2 \Theta}{8\pi(1 + \nu) \cos \lambda} \left[ 1 + \ln \left( \frac{h}{b} \right) \right] \right), \quad (2.3)$$

where  $b = a_0/\sqrt{2}$  and  $a_0$  is the bulk lattice parameter of epilayer.

We subsequent think of multilayer critical thickness. If coherently strained multilayers are grown on a substrate having lattice parameter  $a_s$ , then misfit-free growth is expected if  $a_s = a_{\parallel}$ , where  $a_{\parallel}$  is the equilibrium in-plane lattice parameter. It is implicitly assumed that the layer thicknesses  $h_A$  and  $h_B$  are less than the single-layer critical thickness for the given strain they experience. Such equilibrium structures may be repeated ad infinitum. If the substrate contains threading dislocations, however, then such threading dislocations may traverse the multilayers and undergo the elongation process shown in Fig. 2.3, thereby generating interfacial misfit dislocation lines that destroy interfacial coherence.<sup>67)</sup> The equilibrium critical layer thickness for such threading dislocation-limited coherent growth is obtained by the same procedure used to obtain eq.(2.3), with the exception that in thos multilayer case, it is now required that

$$F_H = 2F_1. \quad (2.4)$$

The factor of 2 aries due to the fact that in a multilayer structure, each interface may support a segment of line dislocation. It should also bec noted that  $e_{\parallel}$  in eq.(2.1) now corresponds to the larger one of strains  $e_{\parallel}^A$  and  $e_{\parallel}^B$ , whereasin a single layer,  $e_{\parallel} = f^0$ . It is perhaps worth emphazing that the critical thickness  $h_c$  so obtained for the multilayer film corresponds to the maximum thickness that an individual layer (not the multilayer as a whole) may be grown.

Recently, these models are used to evaluate single-layer and multilayer critical thicknesses, and the calculated results are in good agreement with a tendency which is given by experimental results.<sup>69-73)</sup>

## Chapter 3 Electronic Structures for the Strained-Layer Superlattices

In the present study, the electronic structures of the valence and conduction subbands are calculated within the framework of a multiband effective-mass approximation in the vicinity of the  $\Gamma$  point by taking the strain effects into account. We assume that the conduction and valence bands are decoupled completely. When the optical energy gap is much larger than the subband energy spacings, this is a good approximation. Electronic states are calculated by using the Kronig-Penney model in the Luttinger-Kohn Hamiltonian.<sup>52,53)</sup> We take account of the strain effects through the appropriate deformation potentials since the lattice mismatch in II-VI SLSs exceeds 4.5%. Such physical quantities as envelope functions, potentials, effective masses<sup>46)</sup> and strains are expanded into Fourier series, because they have the periodicity of superlattices along the growth direction which we choose as  $z$ -axis. Envelope functions and energies are evaluated by means of the numerical diagonalizations of an  $n \times n$  matrix for the conduction band and a  $4n \times 4n$  matrix for the valence band,<sup>74)</sup> where  $n$  is the number of plane waves used in the Fourier expansion.

### 3.1 Strain effect

We treat the effect of strain as a uniaxial stress applied in  $[0,0,1]$  growth direction, as is usually assumed. The whole conduction and valence bands are lifted up through the dilational deformation potentials, and the heavy- and light-hole states in the valence band are split by the shear deformation potential. The heavy- and light-hole

states which are influenced by compressive and tensile stresses,<sup>66,75)</sup> respectively, are shifted to the top of the valence band by the effect of a splitting which results from the shear deformation potential. In ZnSe-ZnS SLSs, as the lattice constant of ZnSe (5.6676Å) is larger than that of ZnS (5.4093Å), ZnSe and ZnS layers are influenced by compressive and tensile stresses, respectively. In ZnTe-ZnSe SLSs, ZnTe(6.103Å) and ZnSe(5.6676Å) layers are influenced also by compressive and tensile stresses, respectively. The lattice constant and other bulk parameters are shown in Table 3.1.

Hamiltonians<sup>91-95)</sup> are given by

$$H_e^c = H_0^c + D_d^c(z)(2e_{xx}(z) + e_{zz}(z)), \quad (3.1)$$

for the conduction bands, and by

$$H_e^v = H_0^v + D_d^v(z)(2e_{xx}(z) + e_{zz}(z)) - \zeta(z)(J_z^2 - \frac{J^2}{3}), \quad (3.2)$$

for the valence bands, where the shear deformation potential is

$$\zeta(z) = -\frac{2}{3}D_u(z)(e_{zz}(z) - e_{xx}(z)). \quad (3.3)$$

Following Hasegawa's method<sup>95)</sup> which includes the spin-orbit split-off energy  $\Lambda(z)$ , the third term of eq.(3.2) is expressed explicitly by

$$-\zeta(z)(J_z^2 - \frac{J^2}{3}) = - \begin{bmatrix} \zeta(z) & 0 & 0 & 0 & 0 & 0 \\ 0 & -\zeta(z) & 0 & 0 & \sqrt{2}\zeta(z) & 0 \\ 0 & 0 & -\zeta(z) & 0 & 0 & -\sqrt{2}\zeta(z) \\ 0 & 0 & 0 & \zeta(z) & 0 & 0 \\ 0 & \sqrt{2}\zeta(z) & 0 & 0 & -\Lambda(z) & 0 \\ 0 & 0 & -\sqrt{2}\zeta(z) & 0 & 0 & -\Lambda(z) \end{bmatrix}. \quad (3.4)$$

$H_0$ 's are Hamiltonians in the absence of strain,  $D_d(z)$ 's are dilational deformation potential coefficients,  $D_u(z)$  is the shear deformation potential coefficient,  $\hbar\mathbf{J}$  is the angular momentum of the hole, and  $e(z)$ 's are homogeneous strain tensors. Index c

Table 3.1. Bulk parameters of ZnSe, ZnS and ZnTe.

		ZnSe	ZnS	ZnTe
Lattice constant	(Å)			
$a_0$		5.6676 <sup>a)</sup>	5.412 <sup>b)</sup>	6.103 <sup>b)</sup>
Energy gap	(meV)			
$E_{g0}$	(4.4K)	2822 <sup>c)</sup>	3842 <sup>c)</sup>	2390 <sup>d)</sup>
$E_{g0}$	(77K)	2820 <sup>b)</sup>	3640 <sup>b)</sup>	2370 <sup>b)</sup>
$E_{g0}$	(RT)	2580 <sup>e)</sup>	3540 <sup>e)</sup>	2260 <sup>e)</sup>
Effective mass				
$m^*/m_0$		0.160 <sup>f)</sup>	0.390 <sup>g)</sup>	0.120 <sup>h)</sup>
Luttinger parameter				
$\gamma_1$		3.77 <sup>i)</sup>	2.54 <sup>i)</sup>	3.74 <sup>i)</sup>
$\gamma_2$		1.24 <sup>i)</sup>	0.75 <sup>i)</sup>	1.07 <sup>i)</sup>
$\gamma_3$		1.67 <sup>i)</sup>	1.09 <sup>i)</sup>	1.64 <sup>i)</sup>
Elastic constant	(dyn/cm <sup>2</sup> )			
$C_{11}$		$8.1 \times 10^{11a)}$	$10.0 \times 10^{11a)}$	$7.1 \times 10^{11a)}$
$C_{12}$		$4.9 \times 10^{11j)}$	$6.5 \times 10^{11k)}$	$4.1 \times 10^{11k)}$
The dependence of energy gap on hydrostatic pressure	(eV cm <sup>2</sup> /kg)			
$dE_g/dP$		$7 \times 10^{-6l)}$	$5.7 \times 10^{-6e)}$	$7 \times 10^{-6l)}$
Shear deformation potential coefficient	(eV)			
$D_u$		1.8 <sup>m)</sup>	1.2 <sup>m)</sup>	2.2 <sup>h)</sup>
Spin-orbit splitting	(eV)			
$\Lambda$		0.43 <sup>n)</sup>	0.07 <sup>m)</sup>	0.92 <sup>o)</sup>

a) Reference 76

b) Reference 77

c) Reference 78

d) Reference 79

e) Reference 80

f) Reference 81

g) Reference 82

h) Reference 83

i) Reference 84

j) Reference 85

k) Reference 86

l) Reference 87

m) Reference 88

n) Reference 89

o) Reference 90

and  $v$  denote the conduction and valence bands, respectively. In this equation, it is clear that the shear deformation potential acts with a contrary sign for heavy- and light-hole states.  $\zeta$ , therefore, split the heavy- and light-hole states in the valence band into a spacing of  $2\zeta$ .

We assume that  $D_d(z)$ 's,  $D_u(z)$  and  $\Lambda(z)$  have the value for bulk in each layer, and that the strains  $e_{xx}(z)$  and  $e_{zz}(z)$  take the constant values  $e_{xx}^w$  and  $e_{zz}^w$  for the well layer and  $e_{xx}^b$  and  $e_{zz}^b$  for the barrier layer, respectively. The magnitude of the strain is estimated by

$$e_{xx}^i = \frac{a_{\parallel} - a_i}{a_i}, \quad (3.5)$$

and

$$e_{zz}^i = -2 \frac{C_{12}^i}{C_{11}^i} e_{xx}^i, \quad (3.6)$$

where  $i = w, b$ , which correspond to well and barrier layers, respectively. In type II SLSs,  $w$  and  $b$  are conformed to well and barrier layers in the valence band, respectively.  $a_{\parallel}$  is the lattice constant parallel to the interface, and is given by Osbourn's equation<sup>96)</sup>

$$a_{\parallel} = a_w \left[ 1 - \frac{d_b D_b}{d_w D_w + d_b D_b} f \right] + O(f^2), \quad (3.7)$$

where

$$D_i = (C_{11}^i + C_{12}^i - 2 \frac{(C_{12}^i)^2}{C_{11}^i} f) + O(f^2), \quad (3.8)$$

and  $f$  is a misfit

$$f = \frac{a_w - a_b}{a_w}. \quad (3.9)$$

In the above,  $a_i$  is the lattice constant,  $d_i$  is the layer thickness, and  $C_{11}^i$  and  $C_{12}^i$  are elastic constants for  $i = w, b$ .

We determine the optical gap in each layer ( $E_g$ ), the conduction band-offset ( $\Delta E_c$ ) and the valence band-offset ( $\Delta E_v$ ) by using eqs.(3.1) and (3.2). The optical gap is

given by the equation

$$E_g = E_g^0 + (D_d^c(z) - D_d^v(z))(2e_{xx}(z) + e_{zz}(z)) + \begin{cases} \zeta(z), & (M_J = \pm\frac{3}{2}) \\ \frac{\Lambda(z) - \zeta(z)}{2} - \sqrt{(\frac{\Lambda(z) + \zeta(z)}{2})^2 + 2\zeta(z)^2}, & (M_J = \pm\frac{1}{2}) \end{cases} \quad (3.10)$$

where  $E_g^0$  is the optical gap in the absence of strain. We also use some parameters of strain (i.e. shear deformation potential, difference of the dilational deformation potential between the conduction and valence bands, and elastic constants), which are given by Fujiyasu and Mochizuki.<sup>76)</sup> To estimate the barrier height, we assume that the conduction band-offset in the absence of strains agrees with a difference between the electron affinities in ZnSe and ZnS or ZnTe and ZnSe, and that the center of energies for the heavy-hole, light-hole and spin-orbit splitt-off bands does not change due to strain.<sup>36,97)</sup>

Thus, we estimate some parameters for ZnSe(27Å)-ZnS(27Å) SLS, ZnSe(22Å)-ZnS(23Å) SLS, ZnSe(20Å)-ZnS(20Å) SLS, ZnTe(10Å)-ZnSe(10Å) SLS and ZnTe(20Å)-ZnSe(20Å) SLS. ZnSe(27Å)-ZnS(27Å) SLS and the other are evaluated by using the band gap measured at 4K and at RT,0 respectively. ZnSe(27Å)-ZnS(27Å) SLS and ZnTe(10Å)-ZnSe(10Å) SLS, and ZnSe(22Å)-ZnS(23Å) SLS are SLSs used by Shen *et al.*<sup>39,40)</sup> and Fan *et al.*<sup>35)</sup> respectively.

The shear deformation potentials (i.e.  $\zeta(\text{ZnSe})$ ,  $\zeta(\text{ZnS})$  and  $\zeta(\text{ZnTe})$ ), the optical gaps (i.e.  $E_g(\text{ZnSe})$ ,  $E_g(\text{ZnS})$  and  $E_g(\text{ZnTe})$ ) for the bulk under the strain, the optical gap  $E_g$  in SLSs, and the barrier height of the conduction-band state ( $\Delta E_c$ ) and valence-band state ( $\Delta E_v$ ) which we calculated are shown in Table 3.2.

In above numerical results, the splitting energies due to the shear deformation potential between heavy- and light-hole states are 127meV for the ZnSe well layer in the ZnSe(27Å)-ZnS(27Å) SLS and 236meV for the ZnTe well layer in the ZnTe(10Å)-ZnSe(10Å) SLS. As compared with the representative III-V compound superlattices,

Table 3.2. The shear deformation potential  $\zeta$ , the optical gaps  $E_g(\text{ZnSe})$ ,  $E_g(\text{ZnS})$  and  $E_g(\text{ZnTe})$  for the bulk under the strain and  $E_g$  for the SLSs, and the barrier height of the conduction-band state ( $\Delta E_c$ ) and valence-band state ( $\Delta E_v$ ).

		ZnSe(27Å)- ZnS(27Å) SLS	ZnSe(20Å)- ZnS(20Å) SLS	ZnSe(22Å)- ZnS(23Å) SLS
$\Delta E_c$	(meV)	40.3	40.3	40.3
$\Delta E_v$	(meV)	-828.1	-678.1	-681.2
$\zeta(\text{ZnSe})$	(meV)	-63.7	-63.7	-65.0
$\zeta(\text{ZnS})$	(meV)	40.6	40.6	39.7
$E_g(\text{ZnSe})$	(meV)	2837.1	2687.1	2687.5
$E_g(\text{ZnS})$	(meV)	3705.5	3405.5	3409.0
$E_g$	(meV)	2837.1	2687.1	2687.5

		ZnTe(20Å)-ZnSe(20Å) SLS ZnTe(10Å)-ZnSe(10Å) SLS
$\Delta E_c$	(meV)	896.1
$\Delta E_v$	(meV)	-896.8
$\zeta(\text{ZnTe})$	(meV)	-117.8
$\zeta(\text{ZnSe})$	(meV)	97.3
$E_g(\text{ZnTe})$	(meV)	2324.9
$E_g(\text{ZnSe})$	(meV)	2325.5
$E_g$	(meV)	1428.7

the strain effects are very large, and thus influence the electronic states significantly.

### 3.2 Electronic structure of the conduction band

For the conduction band, we use the Kronig-Penney model with periodic potentials  $V_c(z)$  and effective masses  $m^*(z)$ . For the effective-mass equation, we adopt the

form,

$$\left[ -\nabla \frac{\hbar^2}{2m^*(z)} \nabla + V_c(z) \right] f_c^{(n)}(\mathbf{k}, \mathbf{r}) = E_c^{(n)}(\mathbf{k}) f_c^{(n)}(\mathbf{k}, \mathbf{r}), \quad (3.11)$$

where  $f_c^{(n)}(\mathbf{k}, \mathbf{r})$  is the envelope function

$$f_c^{(n)}(\mathbf{k}, \mathbf{r}) = e^{i\mathbf{k}_{\parallel} \cdot \mathbf{r}_{\parallel}} e^{ik_z z} \sum_{l=-\infty}^{\infty} C_{cl}^{(n)}(\mathbf{k}) e^{i\frac{2\pi l}{d} z}, \quad (3.12)$$

with the expansion coefficient  $C_{cl}^{(n)}(\mathbf{k})$ ,  $m^*(z)$  is

$$m^*(z) = \begin{cases} m_w^*, & \dots & (\text{well}) \\ m_b^*, & \dots & (\text{barrier}) \end{cases} \quad (3.13)$$

in superlattices, and  $V_c(z)$  is

$$V_c(z) = \begin{cases} 0, & \dots & (\text{well}) \\ \Delta E_c^{(n)}, & \dots & (\text{barrier}) \end{cases} \quad (3.14)$$

In the above,  $\mathbf{k} = (\mathbf{k}_{\parallel}, k_z)$  and  $\mathbf{r} = (\mathbf{r}_{\parallel}, z)$ , where  $\mathbf{k}_{\parallel}$  and  $\mathbf{r}_{\parallel}$  are components of the wave vector and the position vector perpendicular to the  $z$ -axis,  $d$  is the periodicity of SLSs, and  $n$  indicates the  $n$ th conduction subband. For the effective masses of the conduction band, we select  $m_w^* = 0.16m_0$  (ZnSe)<sup>81)</sup> and  $m_b^* = 0.39m_0$  (ZnS)<sup>82)</sup> in ZnSe-ZnS SLSs, and  $m_w^* = 0.12m_0$  (ZnTe)<sup>83)</sup> and  $m_b^* = 0.16m_0$  (ZnSe)<sup>81)</sup> in ZnTe-ZnSe SLSs, where  $m_0$  is the free-electron mass. These are shown in Table 3.1.

Since in eq.(3.11) the potential and the effective mass are different in the well and the barrier, the envelope function itself is continuous and its first derivative is discontinuous at the boundary.<sup>98)</sup> Although we do not impose any boundary conditions explicitly on the envelope function,<sup>99-105)</sup> it will approach a correct form as closely as possible, if the sufficiently large number of terms are used in eq.(3.12). In the calculation for the conduction band, we have found that about 40 terms are sufficient for the eigenvalues and the envelope functions to converge well.

### 3.3 Electronic structure of the valence band

For the valence band, we use the effective-mass equation with the Luttinger-Kohn Hamiltonian<sup>52,53)</sup>

$$- \begin{bmatrix} P(z) + Q(z) - V_v(z) & L(z) & M(z) & 0 \\ L^\dagger(z) & P(z) - Q(z) - V_v(z) & 0 & M(z) \\ M^\dagger(z) & 0 & P(z) - Q(z) - V_v(z) & -L(z) \\ 0 & M^\dagger(z) & -L^\dagger(z) & P(z) + Q(z) - V_v(z) \end{bmatrix} \times \begin{bmatrix} f_{1v}^{(m)}(\mathbf{k}, \mathbf{r}) \\ f_{2v}^{(m)}(\mathbf{k}, \mathbf{r}) \\ f_{3v}^{(m)}(\mathbf{k}, \mathbf{r}) \\ f_{4v}^{(m)}(\mathbf{k}, \mathbf{r}) \end{bmatrix} = E_v^{(m)}(\mathbf{k}) \begin{bmatrix} f_{1v}^{(m)}(\mathbf{k}, \mathbf{r}) \\ f_{2v}^{(m)}(\mathbf{k}, \mathbf{r}) \\ f_{3v}^{(m)}(\mathbf{k}, \mathbf{r}) \\ f_{4v}^{(m)}(\mathbf{k}, \mathbf{r}) \end{bmatrix}, \quad (3.15)$$

which contains the periodic potentials  $V_v(z)$ , effective masses ( Luttinger parameters  $\gamma_1(z)$ ,  $\gamma_2(z)$  and  $\gamma_3(z)$ <sup>53)</sup> ) and strains  $\zeta(z)$ . In eq.(3.15), the spin-orbit split-off states are ignored.  $P(z)$ ,  $Q(z)$ ,  $L(z)$  and  $M(z)$  are

$$P(z) = G_1(z)k_{\parallel}^2 + k_z G_1(z)k_z, \quad (3.16)$$

$$Q(z) = G_2(z)k_{\parallel}^2 - 2k_z G_2(z)k_z + \zeta(z), \quad (3.17)$$

$$L(z) = \frac{i}{2}(k_x - ik_y)\{G_3(z)k_z + k_z G_3(z)\}, \quad (3.18)$$

$$M(z) = G_4(z)(k_x^2 - k_y^2) - iG_3(z)k_x k_y, \quad (3.19)$$

where  $Q(z)$  includes the uniaxial stress applied in [001] direction (i.e.  $\zeta(z)$ ),  $G_i(z)$  are

$$G_1(z) = \frac{\hbar^2 \gamma_1(z)}{2m_0}, \quad (3.20)$$

$$G_2(z) = \frac{\hbar^2 \gamma_2(z)}{2m_0}, \quad (3.21)$$

$$G_3(z) = -\frac{\sqrt{3}\hbar^2 \gamma_3(z)}{m_0}, \quad (3.22)$$

$$G_4(z) = \sqrt{3}G_2(z), \quad (3.23)$$

and  $V_v(z)$  is

$$V_v(z) = \begin{cases} 0, & \dots & (\text{well}) \\ \Delta E_v, & \dots & (\text{barrier}) \end{cases} \quad (3.24)$$

The envelope functions are given by

$$f_{jv}^{(m)}(\mathbf{k}, \mathbf{r}) = e^{i\mathbf{k}_{\parallel} \cdot \mathbf{r}_{\parallel}} e^{ik_z z} \sum_{l=-\infty}^{\infty} C_{jvl}^{(m)}(\mathbf{k}) e^{i\frac{2\pi l}{d} z}, \quad (3.25)$$

with the expansion coefficient  $C_{jvl}^{(m)}(\mathbf{k})$ , where  $m$  indicates the  $m$ th valence subband, and the four components  $j=1,2,3,4$  are casted into two groups, i.e. the heavy-hole ( $j=1,4$ ) and light-hole ( $j=2,3$ ) states. As in the conduction band, we do not impose any boundary conditions on the envelope function,<sup>107-108)</sup> and have found that about 160 terms are necessary in eq.(3.25) for the eigenvalues and the envelope function to converge well.

In ZnSe-ZnS and ZnTe-ZnSe SLSs, the Luttinger parameters  $\gamma_1(z)$ ,  $\gamma_2(z)$  and  $\gamma_3(z)$  are taken to be 3.77, 1.24 and 1.67 for ZnSe layer, 2.54, 2.75 and 1.09 for ZnS layer, and also 3.74, 1.07, and 1.64 for ZnTe layer.<sup>84)</sup> These Luttinger parameters for bulk materials are shown in Table 3.1.

## Chapter 4 Theory of Optical Absorption

Here a formalism of the optical absorption coefficient is described. Though the absorption coefficient on the basis of a similar formalism was calculated by Sanders and Chang,<sup>61)</sup> the  $k_z$  dependence was neglected in their calculation completely. We fully take account of the  $\mathbf{k}$  dependence of the transition matrix in our theory, and explore not only the dependence of absorption coefficient on  $k_{\parallel}$  but also that on  $k_z$ .

We assume that the conduction- and valence-band Bloch states consist of two and four states, respectively. The former's two states are given by

$$u_{1c}(\mathbf{r}) = |s \rangle \alpha, \quad (4.1a)$$

$$u_{2c}(\mathbf{r}) = |s \rangle \beta, \quad (4.1b)$$

where  $\alpha$  and  $\beta$  denote the up and down spin state of an electron, respectively, and  $|s \rangle$  is the  $s$ -like conduction-band Bloch state. The wave function of the conduction-band state is expressed as

$$\Psi_c^{(n)}(\mathbf{k}, \mathbf{r}) = f_c^{(n)}(\mathbf{k}, \mathbf{r}) \sum_{i=1}^2 u_{ic}(\mathbf{r}). \quad (4.2)$$

For the hole states in the valence band, the four Bloch states consist of the linear combinations of the products of the electron spinor and the  $p$ -like states  $|X \rangle$ ,  $|Y \rangle$  and  $|Z \rangle$ . They are given by

$$\begin{aligned} u_{1v}(\mathbf{r}) &= \left| \frac{3}{2}, \frac{3}{2} \right\rangle \\ &= \frac{1}{\sqrt{2}}(X + iY)\alpha, \end{aligned} \quad (4.3a)$$

$$\begin{aligned} u_{2v}(\mathbf{r}) &= \left| \frac{3}{2}, \frac{1}{2} \right\rangle \\ &= \frac{i}{\sqrt{6}}[(X + iY)\beta - 2Z\alpha], \end{aligned} \quad (4.3b)$$

$$u_{3v}(\mathbf{r}) = \left| \frac{3}{2}, -\frac{1}{2} \right\rangle$$

$$= \frac{1}{\sqrt{6}}[(X + iY)\alpha + 2Z\beta], \quad (4.3c)$$

$$\begin{aligned} u_{4v}(\mathbf{r}) &= \left| \frac{3}{2}, -\frac{3}{2} \right\rangle \\ &= \frac{1}{\sqrt{2}}(X - iY)\beta, \end{aligned} \quad (4.3d)$$

where  $|J, M_j\rangle$  means the  $p$ -like wave function with the total angular momentum  $J = \frac{3}{2}$  and the magnetic quantum number  $M_j = -\frac{3}{2}, -\frac{1}{2}, \frac{1}{2}, \frac{3}{2}$ . The wave function of the valence-band state is expressed as

$$\Psi_v^{(m)}(\mathbf{k}, \mathbf{r}) = \sum_{j=1}^4 f_{jv}^{(m)}(\mathbf{k}, \mathbf{r}) u_{jv}(\mathbf{r}), \quad (4.4)$$

where the bulk Bloch functions with  $j = 1, 2, 3, 4$  mean the Bloch states with  $M_j = \frac{3}{2}, \frac{1}{2}, -\frac{1}{2}, -\frac{3}{2}$ , respectively.

The total absorption coefficient  $\alpha^P(\omega)$  is given by summing over all of the individual band-to-band absorption coefficients. Thus,

$$\alpha^P(\omega) = \sum_{nm} \alpha_{nm}^P(\omega), \quad (4.5)$$

where  $P$  indicates two incident-photon polarizations, i.e.  $TE$  and  $TM$ , and  $\alpha_{nm}^P(\omega)$  indicates the absorption coefficient from valence subband  $m$  to conduction subband  $n$ . This absorption coefficient can be derived by following the calculation of Asada *et al.*<sup>109)</sup> as

$$\alpha_{nm}^P(\omega) = \sum_{j=1}^4 \alpha_{nmj}^P(\omega), \quad (4.6)$$

with

$$\begin{aligned} \alpha_{nmj}^P(\omega) &= \frac{4\pi e^2}{\epsilon m_0^2 c^2 \omega} \sum_{k_z} \int dk_{\parallel} k_{\parallel} W_{nmj}(\mathbf{k}) \\ &\quad \times |p_{cv}|^2 G_{Pj}(k_{\parallel}, k_z) \delta(E_{cv}^{(n,m)}(\mathbf{k}) - \hbar\omega), \end{aligned} \quad (4.7)$$

where

$$W_{nmj}(\mathbf{k}) = \left| \sum_l C_{cl}^{(n)*}(\mathbf{k}) C_{jvl}^{(m)}(\mathbf{k}) \right|^2, \quad (4.8)$$

which indicates the overlap of envelope functions between the conduction and valence subbands, and

$$G_{TEj=1,4}(k_{\parallel}, k_z) = \frac{1}{4} \left( 1 + \frac{k_z^2}{k^2} \right), \quad (4.9a)$$

$$G_{TEj=2,3}(k_{\parallel}, k_z) = \frac{1}{6} \left( 1 + \frac{3k_{\parallel}^2}{2k^2} \right), \quad (4.9b)$$

for  $P=TE$ , and

$$G_{TMj=1,4}(k_{\parallel}, k_z) = \frac{1}{2} \frac{k_{\parallel}^2}{k^2}, \quad (4.10a)$$

$$G_{TMj=2,3}(k_{\parallel}, k_z) = \frac{1}{6} \left( 1 + \frac{3k_z^2}{k^2} \right), \quad (4.10b)$$

for  $P=TM$ . The derivation of this equation is fully shown in Appendix A.

In eq.(4.7),  $\epsilon$  is the dielectric constant of SLSs, and  $p_{cv}$  is the transition momentum matrix element between the conduction- and valence-band states

$$p_{cv} = \langle X | p_x | S \rangle = \langle Y | p_y | S \rangle = \langle Z | p_z | S \rangle, \quad (4.11)$$

which is introduced by using the orthonormality of the spin states  $\alpha$  and  $\beta$  and the symmetry properties of the group  $O_h$ .  $p_x$ ,  $p_y$  and  $p_z$  are  $x$ ,  $y$  and  $z$  components of the momentum operator  $\mathbf{p}$ , respectively. We assume that  $p_{cv}$  in ZnSe has the same constant value as those in ZnS and ZnTe. It is also assumed that the in-plane dispersions of hole-subbands are isotropic, which is confirmed by a calculation of the dispersion relation along the [1,0] and [1,1] direction, as is shown in Figs. 4.2 and 4.2.  $E_{cv}^{(n,m)}(\mathbf{k})$  which indicates the band gap between the conduction and valence subbands at  $\mathbf{k}$  is given by

$$E_{cv}^{(n,m)}(\mathbf{k}) = E_g + E_c^{(n)}(\mathbf{k}) - E_v^{(m)}(\mathbf{k}). \quad (4.12)$$

The absorption coefficients are calculated by taking account of the entire dispersions shown in Chaps. 5~8 as well as the numerical values of the wave functions.

# Chapter 5 Electronic Structures and Absorption Spectrum of ZnSe(27Å)-ZnS(27Å) Strained-Layer Superlattice

## 5.1 Introduction

In this chapter, we show the electronic structures and the absorption spectrum for ZnSe(27Å)-ZnS(27Å) SLS calculated by theoretical method. ZnSe-ZnS SLSs consist of II-VI semiconductors and belong to type I superlattice, which have ZnSe well and ZnS barrier layers in both conduction and valence bands.

For ZnSe-ZnS SLSs, many optical absorption experiments<sup>31-40)</sup> have been carried out, and some interpretations for the origin of the absorption spectra have been proposed. Since these SLSs have the very small conduction band-offset due to the common-cation rule in contrast to the very large valence band-offset, we have a great interest in the structure of the conduction and valence subbands and the optical absorption which may be influenced by these properties. The absorption spectra have two strong absorption peaks in the vicinity of the fundamental absorption edge, in addition to a few broad bands in the high-energy regime.<sup>35,39,40)</sup>

As an application of our theory, we calculate the electronic structures and the absorption spectra neglecting excitonic effects for ZnSe(27Å)-ZnS(27Å) SLS. The electronic structures are derived within the framework of an effective-mass approximation, and are evaluated by including the mixing of heavy- and light-hole states in the valence band. The absorption spectrum is calculated by taking the dependence of the transition matrix on the wave vector  $\mathbf{k}$  fully into account, and the calculated

absorption spectra are compared with the experimental results by Shen *et al.*<sup>39,40)</sup> The calculation on ZnSe(27Å)-ZnS(27Å) SLS has already been reported elsewhere.<sup>48,49)</sup> To explore the origin of absorption spectra, further, we decompose the total absorption spectrum into the band-to-band absorption spectra, and pick up main components. We also examine the dependence of the optical absorption on incident-photon polarizations in detail.

Organization of this chapter is as follows. In section 5.2, we show the results calculated for the electronic structures of the valence and conduction subbands within the framework of a multiband effective-mass approximation by taking the strain effects into account. In section 5.3, we show the result calculated for the total absorption spectra, and compare with the experimental result. Analysis of each transition and the dependence on the polarization are shown in section 5.4 and section 5.5, respectively. Finally, conclusions are summarized in section 5.6.

## 5.2 Results for the electronic structures

Figures 5.1(a) and 5.1(b) show the conduction- and valence-subband dispersions in the ZnSe(27Å)-ZnS(27Å) SLS for  $k_{\parallel}=0$  as a function of  $k_z$ . In the conduction band, the  $i$ th subband is named as  $C_i$ . In the valence band,  $HH_i$  or  $LH_i$  means the subband which is reduced at  $\mathbf{k}=0$  to the  $i$ th heavy- or  $i$ th light-hole state, respectively. It is seen that the higher conduction subband has the larger dispersion, while the valence subbands are almost dispersionless. These band structures imply an extended nature of the conduction subbands in the SLS and a confinement of the valence-band states within the ZnSe quantum well. The optical interband transitions from the confined hole states to the free-electron-like high conduction subbands may lead to the continuous-absorption background, so that the observed structureless in-

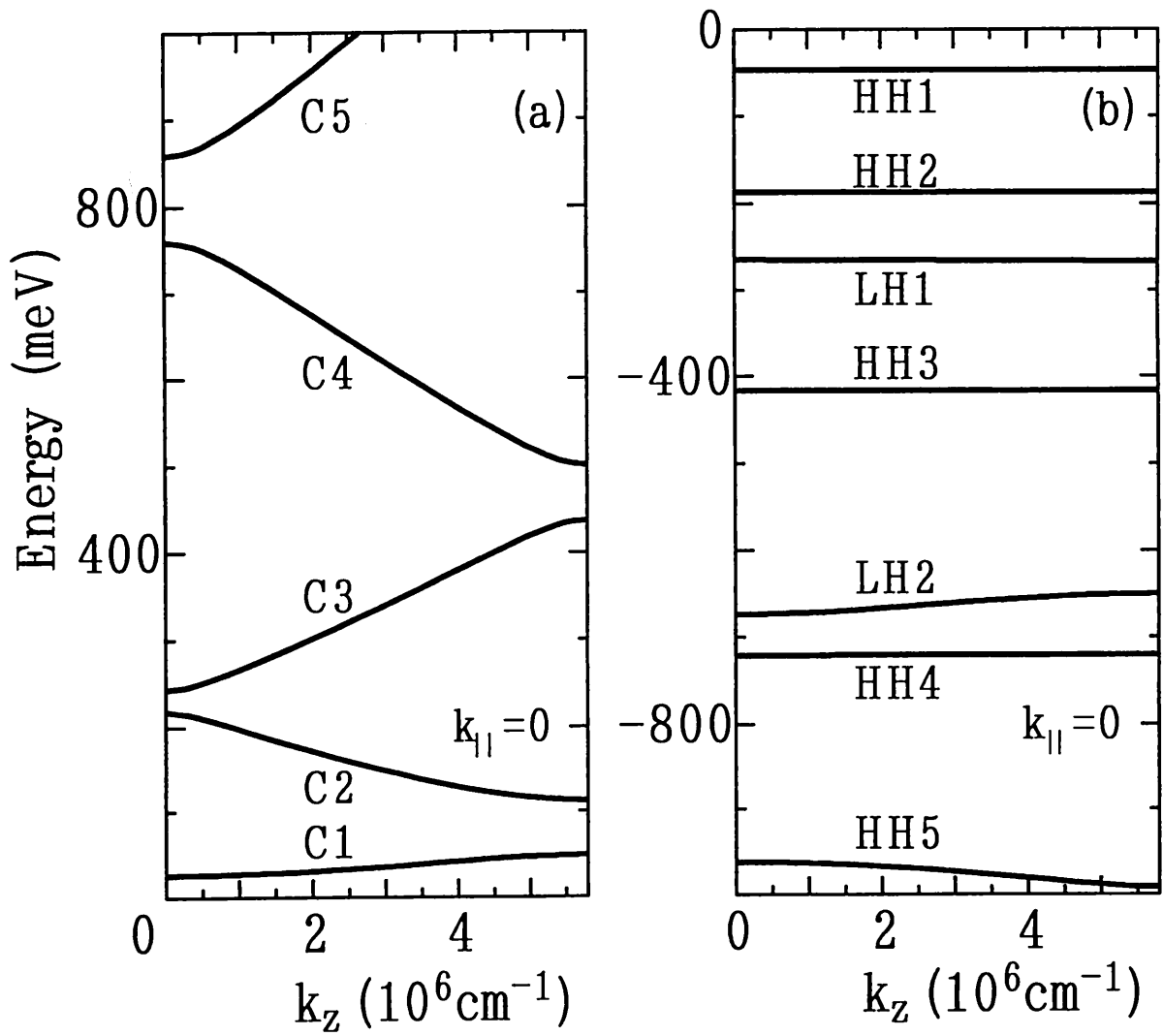


Fig. 5.1. The energy dispersions of conduction subbands (a) and valence subbands (b) in the ZnSe(27Å)-ZnS(27Å) SLS for  $k_{\parallel}=0$  as a function of  $k_z$ . The assumed barrier potentials are 59.2meV for the conduction band and -830.0meV for the valence band.

crease of the absorption in a high-energy regime reflects the minibands nature of the conduction-band states in the ZnSe-ZnS SLS. This is similar to the optical joint density of states in a three-dimensional semiconductor where both the conduction- and valence-band states are described by the parabolic energy dispersions. Further, the HH2 subband state becomes higher than the LH1 subband state, because the shear deformation potential in the valence band state has the large value, as explained in section 3.1.

Figure 5.2 shows the in-plane dispersion of the valence subband at  $k_z=0$  as a function of  $k_{\parallel}$  for ZnSe(27Å)-ZnS(27Å) SLS, respectively. The solid and dashed curves correspond to the dispersion in the [1,0] and [1,1] direction, respectively. This figure confirms the isotropic feature of the in-plane dispersions in the valence subbands.

### 5.3 Total absorption spectra

Figure 5.3(a) shows the experimental result observed at 16K on the  $TE$  polarization condition by Shen *et al.*<sup>39)</sup> Figs. 5.3(b) and 5.3(c) show the total absorption coefficients calculated for ZnSe(27Å)-ZnS(27Å) SLS for  $TE$  and  $TM$  polarizations, respectively. The calculated absorption spectrum in Fig. 5.3(b) reproduces the overall features of the experimental result.<sup>39)</sup> A detailed comparison between Figs. 5.3(a) and 5.3(b) reveals some discrepancies, which may be attributed to excitonic effects.<sup>45)</sup> Apart from excitonic effects, the first observed line can be assigned to the HH1-C1 transition.

We have confirmed that the HH2-C2 and HH1-C2 transitions appear near the second experimental peak E(LH1-C1) which Shen *et al.*<sup>39)</sup> assigned to the excitonic LH1-C1 transition. The strength for the HH2-C2 transition is, however, one order of magnitude less than that of the HH1-C1 band, so that it cannot contribute appreciably to the second peak. Though the HH1-C2 transition is neglected usually in a simplified

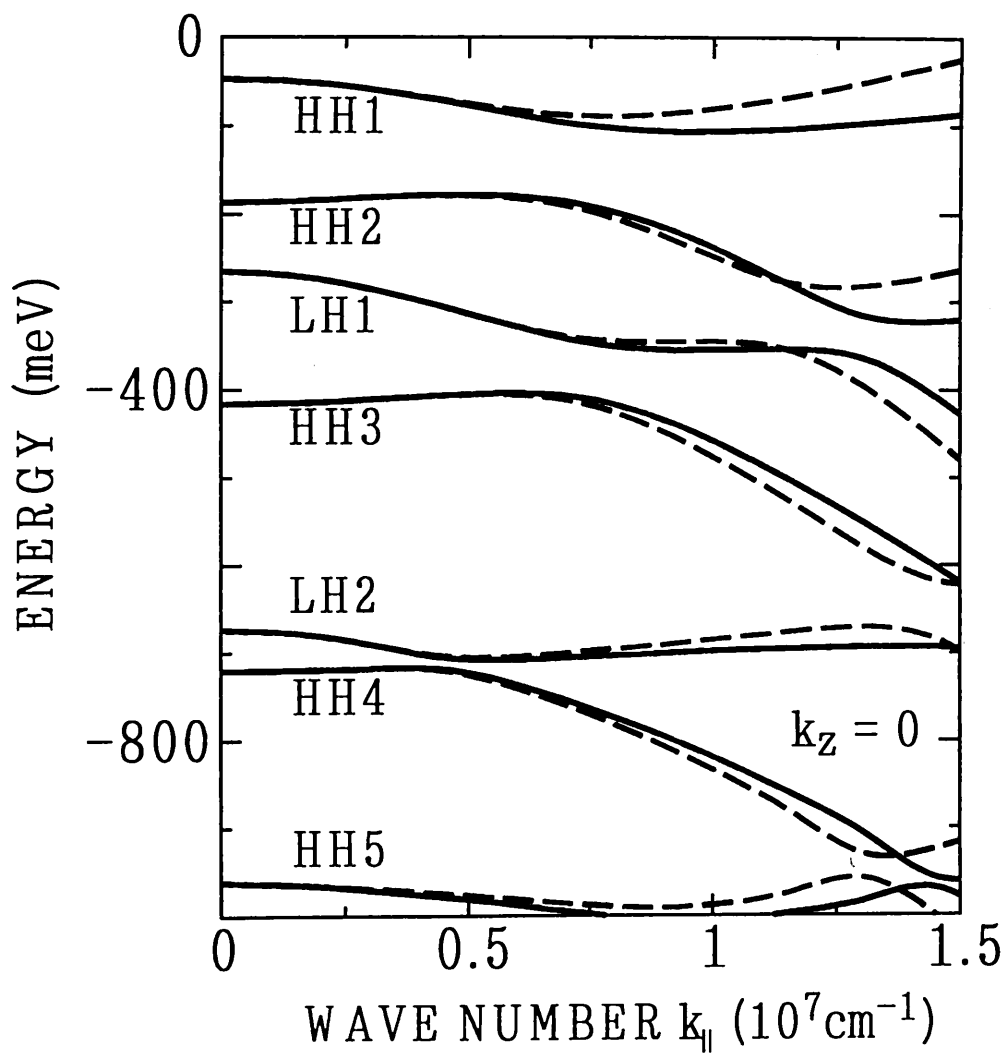


Fig. 5.2. The in-plane dispersions of valence subbands in the ZnSe (27Å)-ZnS(27Å) SLS as a function of  $k_{||}$  for  $k_z=0$ . The solid and dashed lines represent subband energies in the [1,0] and [1,1] direction, respectively.

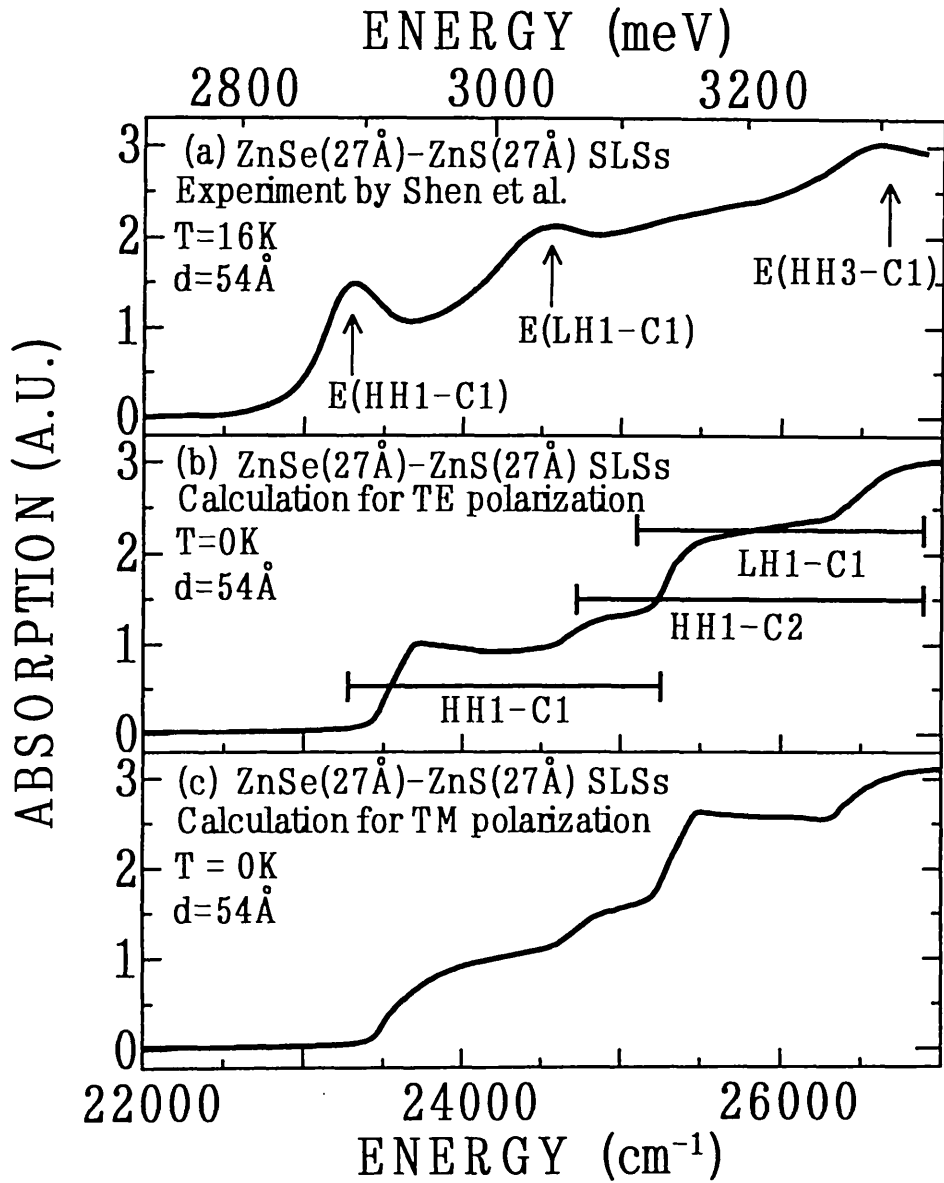


Fig. 5.3. (a) Observed absorption spectra for ZnSe(27Å)-ZnS(27Å) SLS at 16K by Shen *et al.*, and calculated absorption spectra for (b) *TE* and (c) *TM* incident-photon polarizations at 0K. HH $j$ -C $i$  and LH $j$ -C $i$  denote the transitions from the  $j$ th heavy- and light-hole subband levels to  $i$ th conduction-subband level, respectively. E(HH $j$ -C $i$ ) and E(LH $j$ -C $i$ ) indicate the excitonic HH $j$ -C $i$  and LH $j$ -C $i$  transitions assigned by Shen *et al.*(ref. 39) The horizontal bar stands for the width of the absorption band associated with each HH1(LH1)-C $j$  transition.

model, its existence is clearly seen in Figs. 5.3(a) and 5.3(b). If excitonic effects are taken into account properly, the LH1-C1 transition will dominate the second experimental peak, because the LH1 and C1 states are confined in the quantum well, and the C2 state is not. Our present result supports the assignment by Shen *et al.*<sup>39)</sup>

In Figs. 5.4(a) and 5.4(b), the total absorption spectra are decomposed into main band-to-band absorption spectra for *TE* and *TM* incident-photon polarizations, respectively. The solid, dashed and dot-dashed curves show the HH1-C1, LH1-C1 and HH1-C2 transitions, respectively. These absorption spectra form four main bumps in the total absorption spectra. The left and right shoulders in the HH1-C1 absorption spectra correspond to the first and the second bumps in Figs. 5.3(b) and 5.3(c), and the left and right shoulders in the LH1-C1 absorption spectra correspond to the third and the fourth bumps in Figs. 5.3(b) and 5.3(c), respectively. Further, the HH1-C2 absorption spectra influence the bumps from the second to the fourth in the total absorption spectra. These spectra start to appear in the second bump, increase the strength at the start of the third bump drastically, and form a peak at the start of the fourth bump. The right shoulders of the HH1-C1 and LH1-C1 transitions consist of the mixing of the light-hole state with heavy-hole state and the heavy-hole state with light-hole state, respectively, and the HH1-C2 absorption spectra also are greatly influenced by the mixing effects.

Further, these absorption spectra are influenced by large strain effects. The energy spacing between HH1-C1 and LH1-C1 transitions exceeds 200meV, because the splitting energy between the heavy- and light-hole states and the difference between the potential barriers which result from the shear deformation potential are very large.

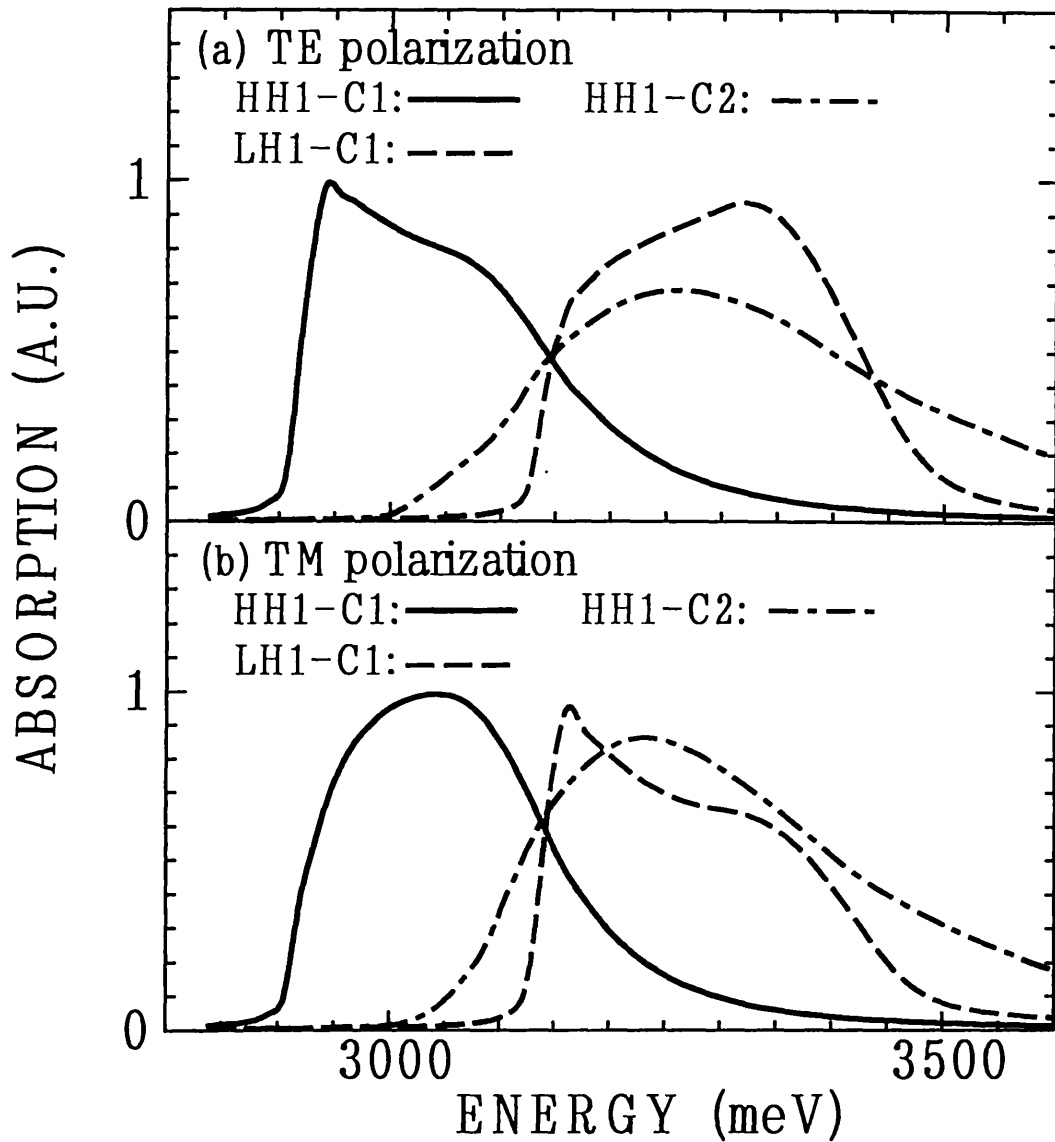


Fig. 5.4. Three subband-to-subband absorption spectra for transitions from the first heavy-hole (HH1) and light-hole (LH1) subband states to the first (C1) and second (C2) conduction-subband states in ZnSe(27Å)-ZnS(27Å) SLS, which have (a) *TE* and (b) *TM* incident-photon polarizations. HH1-C1, LH1-C1 and HH1-C2 absorption spectra are shown by solid, dashed and dot-dashed curves, respectively.

## 5.4 Analysis of each transition

Figures 5.5, 5.6 and 5.7, which are related to the HH1-C1, LH1-C1 and HH1-C2 transitions, respectively, show (a) the overlap of envelope functions between the conduction and valence subbands  $W_{nmj}(\mathbf{k})$  and (b) the band gap  $E_{cv}^{(n,m)}(\mathbf{k})$  as a function of  $k_{\parallel}$  and  $k_z$ . The in-plane wave number ( $k_{\parallel}$ ) is drawn in the horizontal axis, and  $k_z$  increases in the direction of the arrow in the figures. The mixing effects are expressed by HH and LH in these figures, which indicate the transitions from the heavy- and light-hole states to the conduction-subband states, respectively. Further, the joint densities of states are shown in Fig. 5.8, in which the solid, dot-dashed and dashed curves show the HH1-C1, HH1-C2 and LH1-C1 transitions, respectively.

In the vicinity of  $k_{\parallel} \approx 1.0 \times 10^7 \text{cm}^{-1}$ , Fig. 5.5 shows the peak of LH and the swell of  $E_{cv}^{(n,m)}(\mathbf{k})$  which result from the mixing effects in the valence band. The  $E_{cv}^{(n,m)}(\mathbf{k})$  is about 3100meV~3200meV, increase the joint density of states largely, and corresponds to the right shoulders of the HH1-C1 absorption spectrum.

In the vicinity of  $k_{\parallel} \approx 1.0 \times 10^7 \text{cm}^{-1}$  and  $2.1 \times 10^7 \text{cm}^{-1}$  in Fig. 5.6, the HH peak appears, and  $E_{cv}^{(n,m)}(\mathbf{k})$  corresponding to these  $k_{\parallel}$  is swollen. Thus the joint density of states shown in Fig. 5.8 increases at about 3350meV and 4150meV. Though  $E_{cv}^{(n,m)}(\mathbf{k})$  in the vicinity of 3350meV makes a right shoulder of the LH1-C1 absorption spectrum, those of about 4150meV which we do not show in Fig. 5.3 are not important.

In the HH1-C2 transition  $W_{nmj}(\mathbf{k})$  is not small, although it is neglected usually in a simplified model. As for HH,  $W_{nmj}(\mathbf{k})$  for small  $k_{\parallel}$  and  $k_z$  is only one third of those of HH1-C1 and LH1-C1 at the same  $\mathbf{k}$ . But, around  $k_{\parallel} \approx 1.0 \times 10^7 \text{cm}^{-1}$ , those of HH1-C2 transition have either nearly the same or a little large strength depending on  $k_z$ , as compared with those of two other transitions. As for LH,  $W_{nmj}(\mathbf{k})$  for HH1-C2 transition is a little larger than those of two other transitions. Therefore, the ratio of

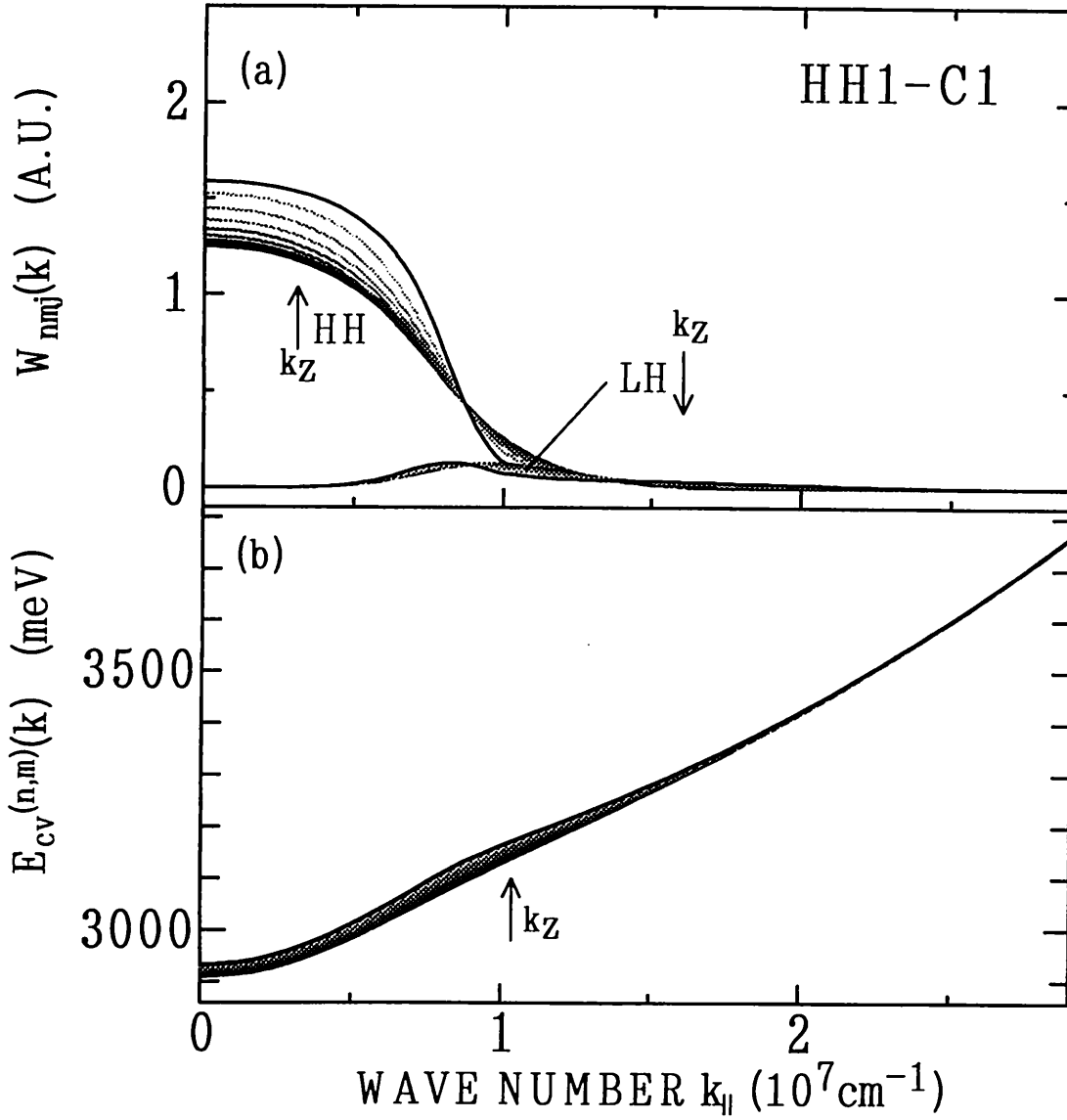


Fig. 5.5. (a) Overlap of envelope functions  $W_{nmj}(\mathbf{k})$  and (b) band gap  $E_{cv}^{(n,m)}(\mathbf{k})$  for HH1-C1 transition in the ZnSe(27Å)-ZnS(27Å) SLS as a function of  $k_{||}$  and  $k_z$ .  $k_z$  increases in the direction of the arrow.

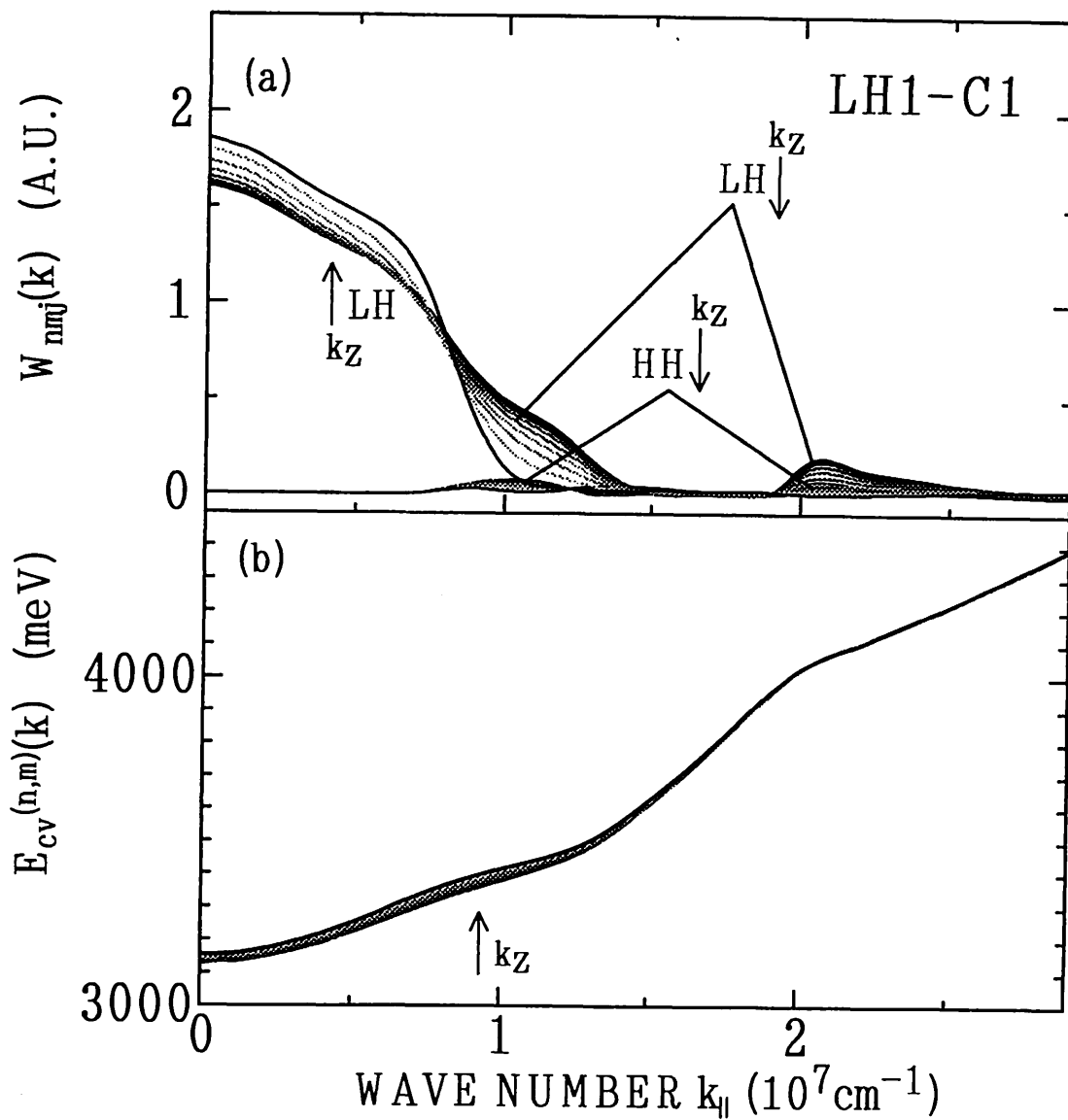


Fig. 5.6. (a) Overlap of envelope functions  $W_{nmj}(\mathbf{k})$  and (b) band gap  $E_{cv}^{(n,m)}(\mathbf{k})$  for LH1-C1 transition in the ZnSe(27Å)-ZnS(27Å) SLS as a function of  $k_{||}$  and  $k_z$ .  $k_z$  increases in the direction of the arrow.

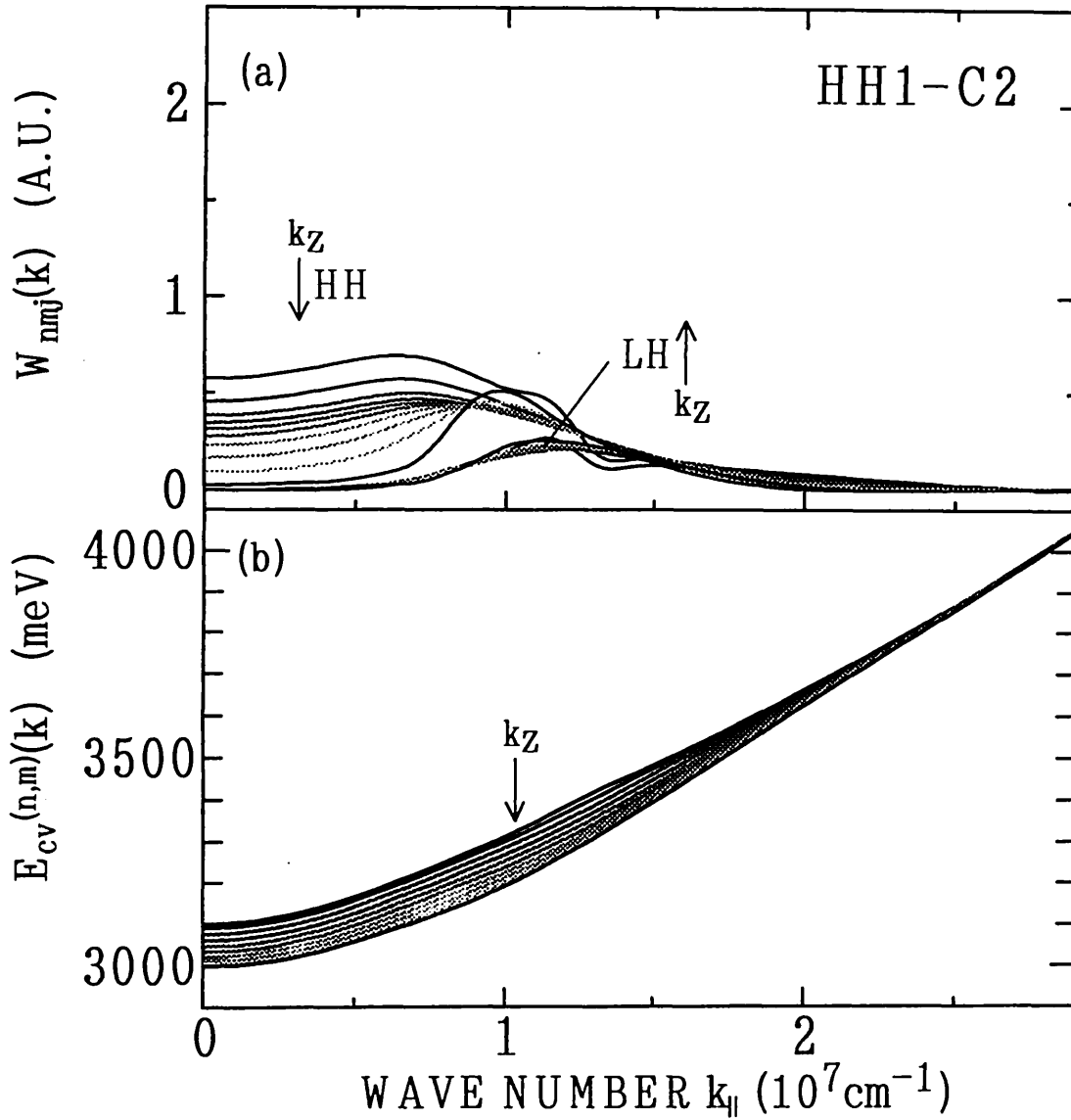


Fig. 5.7. (a) Overlap of envelope functions  $W_{nmj}(\mathbf{k})$  and (b) band gap  $E_{cv}^{(n,m)}(\mathbf{k})$  for HH1-C2 transition in the ZnSe(27Å)-ZnS(27Å) SLS as a function of  $k_{\parallel}$  and  $k_z$ .  $k_z$  increases in the direction of the arrow.

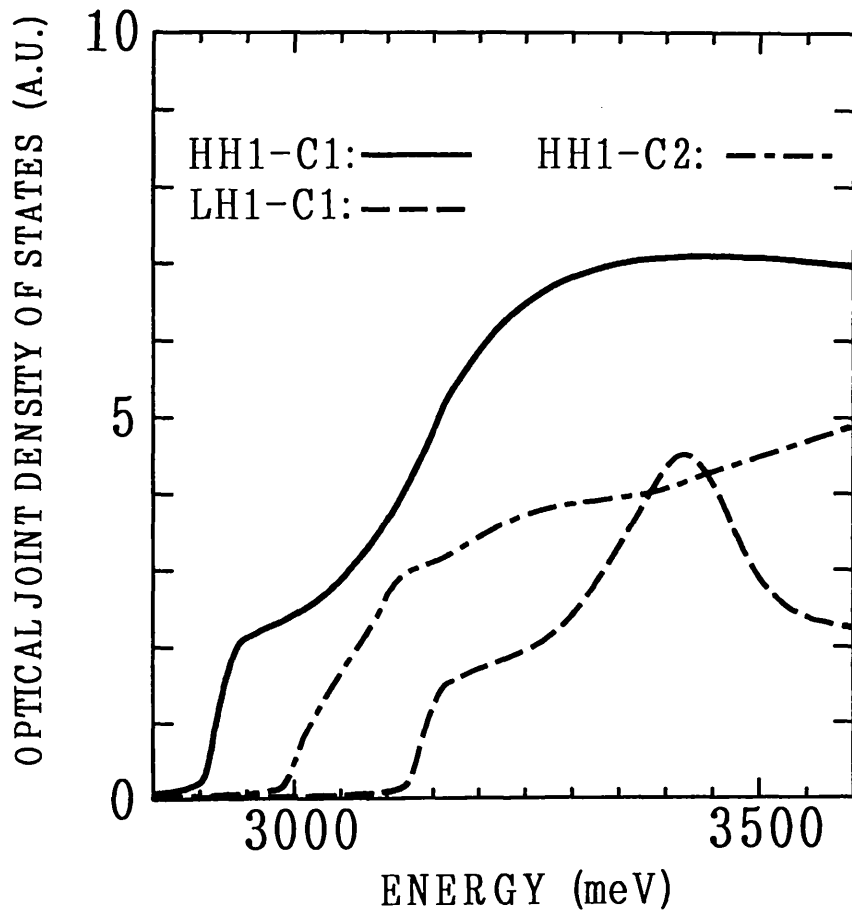


Fig. 5.8. Optical joint density of states for ZnSe(27Å)-ZnS(27Å) SLS. Solid, dashed and dot-dashed curves correspond to HH1-C1, LH1-C1 and HH1-C2 transitions.

LH to HH is larger than those of two other transitions, and the transitions from two hole states are mixed with each other comparably.

## 5.5 Dependence on the polarization

We also examine the dependence of the main absorption components on the polarization. It is evident from Figs. 5.3(b) and 5.3(c) that the overall profile of the absorption spectrum is modified greatly by changing the polarization from  $TE$  to  $TM$ . In the first absorption band around 2920meV, the intensity for  $TM$  polarization is smaller than that for  $TE$  polarization. In the shoulder-like third absorption band above 3100meV, the absorption spectrum for  $TM$  polarization is enhanced more than that for  $TE$  polarization. These drastic changes are driven by  $G_{Pj}$  in the integrand of eq.(4.7).

To understand these results deeply, we decompose the band-to-band absorption spectra shown in Fig. 5.4 into  $k_z$ -component, as  $G_{Pj}$  depend on  $\mathbf{k}$ , and results are shown in Fig. 5.9. In spite of the use of the same  $E_{cv}^{(n,m)}(\mathbf{k})$  and  $W_{nmj}(\mathbf{k})$ , we find some characteristic differences between the two polarizations. As for the behavior with increasing  $k_z$  in the HH1-C1 component, the left shoulders which originate dominantly from the transition from the heavy-hole state stand up sharply for  $TE$  polarization and gradually for  $TM$  polarization, and the right shoulders which include the light-hole state in the main heavy-hole state increase a little for  $TE$  polarization and decrease, changing from a swell to one peak for  $TM$  polarization. In the LH1-C1 component, the tendency is nearly inverse. When  $k_z$  increases, the left shoulders which consist of the light-hole state decrease gradually for  $TE$  polarization and stand up sharply for  $TM$  polarization, and the right shoulders which include the heavy-hole state in the main light-hole state decrease, changing from a small swell to a large one for  $TE$  polarization and increase a little for  $TM$  polarization. In the HH1-C2

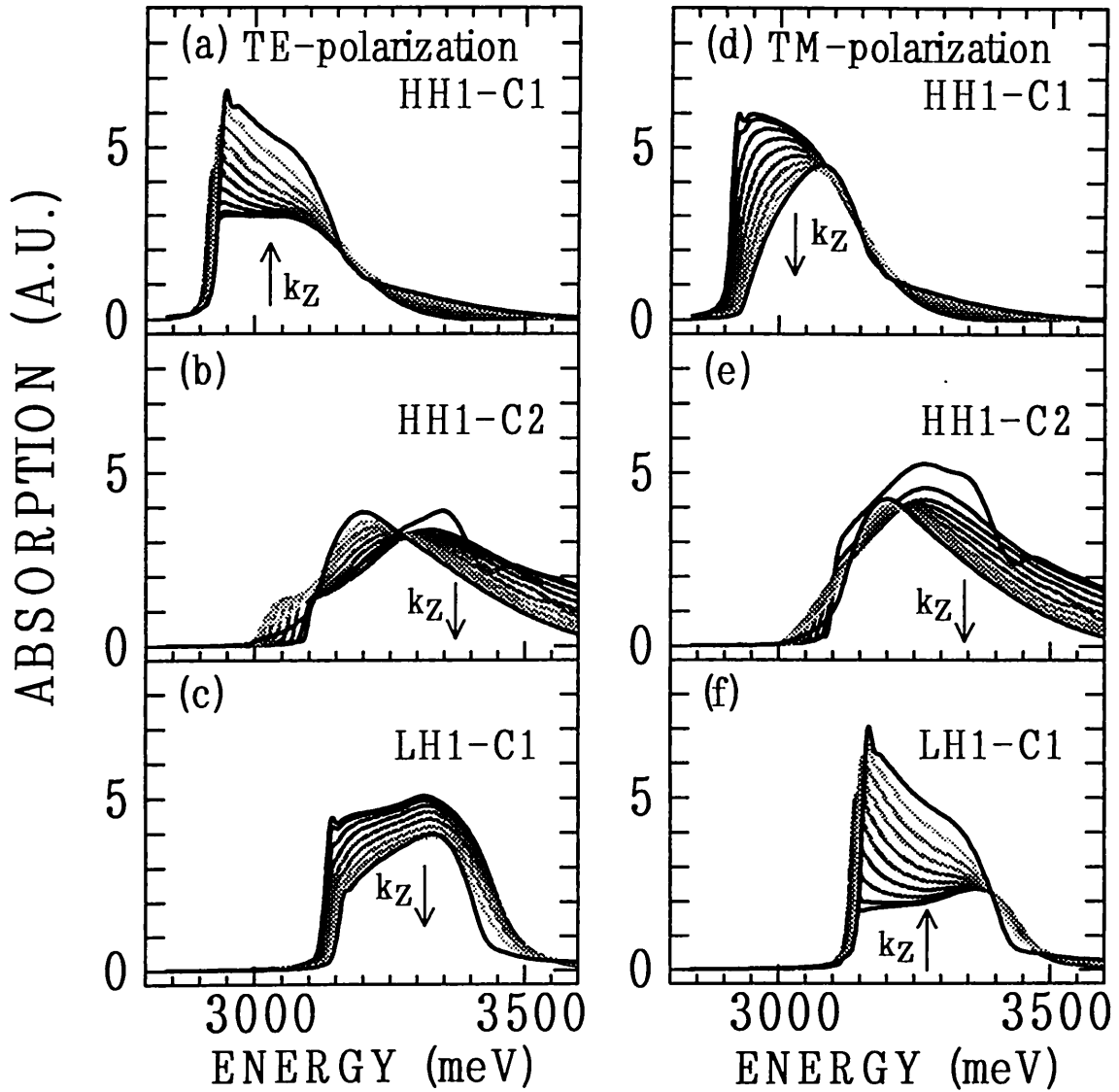


Fig. 5.9. Subband-to-subband absorption spectra decomposed into  $k_z$ -components. (a)~(c) and (d)~(f) denote the  $TE$  and  $TM$  incident-photon polarizations, respectively.  $HHj-Ci$  and  $LHj-Ci$  denote the transitions from the  $j$ th heavy- and light-hole subband levels to  $i$ th conduction-subband level, respectively.  $k_z$  increases in the direction of the arrow.

component, the absorption spectra for the two polarizations are not different largely from each other.

In the HH1-C1 and LH1-C1 absorption spectra, the left shoulders which do not include the mixing of the heavy- and light-hole states are influenced by the transition from only one state (i.e. either heavy- or light-hole state) in the valence subband.  $G_{P_j}$  in the absorption coefficients is proportional to either  $k_z^2$  or  $k_{\parallel}^2$ , and a marked difference between  $TE$  and  $TM$  polarizations appears. However, the right shoulders in the HH1-C1 and LH1-C1 absorption spectra consist of two kinds of the absorption coefficient which have different  $G_{P_j}$  for the transition from the heavy- and light-hole states. While one ( $G_{P_j=1,4}$  or  $G_{P_j=2,3}$ ) increases as  $k_z^2$ , the other ( $G_{P_j=2,3}$  or  $G_{P_j=1,4}$ ) increases as  $k_{\parallel}^2$ . In other words, when the transition from one state (heavy- or light-hole state) in the mixing of the heavy- and light-hole states increases as  $k_z^2$ , the transition from other state (light- or heavy-hole state) increases as  $k_{\parallel}^2$ . Since the right shoulders in HH1-C1 and LH1-C1 absorption spectra include the transitions from both states, a marked difference between  $TE$  and  $TM$  polarizations does not appear.

The HH1-C2 absorption spectra also do not have such a marked difference between  $TE$  and  $TM$  polarizations. This is because the ratio of LH to HH is large as is shown in Fig. 5.7, and the absorption spectra from two states are mixed comparably. As is shown in Figs. 5.3(b) and 5.3(c), therefore, both of the first and the third bumps which are connected with the onset of the HH1-C1 and LH1-C1 transitions depend sensitively on the polarization, but the second and the fourth bumps do not. Thus we can suggest that a careful study on the polarization dependence of the absorption spectrum may lead to a decisive assignment of the origin of the absorption bands.

## 5.6 Conclusions

On the basis of a detailed calculation of the electronic structure in an effective-mass approximation, the optical absorption coefficient is evaluated carefully for the SLS of type I by taking explicitly the  $\mathbf{k}$  dependence of the transition matrix into account. The absorption spectrum is fully examined except for excitonic effects by an analysis of the mixing of the heavy- and light-hole states, and its dependence on the incident-photon polarization is clarified. The theoretical results are compared with the recent experiment on ZnSe-ZnS SLSs by Shen *et al.*<sup>39,40)</sup>

In ZnSe(27Å)-ZnS(27Å) SLS, the mixing effects in the main HH1-C1 and LH1-C1 transitions contribute another swell in higher energy side (i.e. right shoulder) as well as initial start (i.e. left shoulder). It is clarified that the observed second absorption peak is composed of the transitions such as LH1-C1 and HH1-C2, and it is suggested that excitonic effects may give rise to a large enhancement of the absorption on the LH1-C1 transition. Due to large strain effects, the energy spacing between HH1-C1 and LH1-C1 transitions exceeds 200meV. The characteristic differences between  $TE$  and  $TM$  polarizations are determined mainly by HH1-C1 and LH1-C1 transitions. Therefore, experiments for the two different polarizations can provide a key to explore the nature of the optical absorption bands in ZnSe-ZnS SLSs.

# Chapter 6 Electronic Structures and Absorption Spectrum of ZnTe(10Å)-ZnSe(10Å) Strained-Layer Superlattice

## 6.1 Introduction

In this chapter, we show the electronic structures and the absorption spectrum for ZnTe(10Å)-ZnSe(10Å) SLS calculated by theoretical method. ZnTe-ZnSe SLSs consist of II-VI semiconductors and belong to type II superlattice, which have ZnTe barrier and ZnSe well layers in the conduction band, and ZnTe well and ZnSe barrier layers in the valence band. The ZnTe well in the valence band and the ZnSe well in the conduction band do not overlap.

For ZnTe-ZnSe SLSs, though many optical experiments<sup>40-44)</sup> have been carried out, optical absorption experiments are but few, and the work by Shen *et al.*<sup>40)</sup> is notable. The absorption spectrum has been measured at room temperature, and found to consist of a small bump in the low-energy side and a large bump in the high-energy side.<sup>40)</sup>

We calculate the electronic structures and the absorption spectra neglecting excitonic effects for ZnTe(10Å)-ZnSe(10Å) SLSs. The electronic structures are derived within the framework of an effective-mass approximation, and are evaluated by including the mixing of heavy- and light-hole states in the valence band. The absorption spectrum is calculated by taking the dependence of the transition matrix on the wave vector  $\mathbf{k}$  fully into account, and the calculated absorption spectra are compared with the experimental results by Shen *et al.*<sup>40)</sup> The calculation on ZnTe(10Å)-ZnSe(10Å)

SLS has already been reported elsewhere.<sup>49)</sup> To explore the origin of absorption spectra, further, we decompose the total absorption spectrum into the band-to-band absorption spectra, and pick up main components. We also examine the dependence of the optical absorption on incident-photon polarizations in detail.

Organization of this chapter is as follows. In the next section, we show the results calculated for the electronic structures of the valence and conduction subbands within the framework of a multiband effective-mass approximation by taking the strain effects into account. In section 6.3, we show the result calculated for the total absorption spectra, and compare with the experimental result. The dependence on the polarization is shown in section 6.4. Finally, conclusions are summarized in section 6.5.

## 6.2 Results for the electronic structures

Figures 6.1(a) and 6.1(b) show the conduction- and valence-subband dispersions in the ZnTe(10Å)-ZnSe(10Å) SLS for  $k_{\parallel} = 0$  as a function of  $k_z$ . Though the conduction band-offset of the ZnTe-ZnSe SLS is very large in contrast to those of ZnSe-ZnS SLSs, only one band (C1) with large dispersion is confined in the ZnSe quantum well. This is because the thickness of barrier layer is very thin, and the influence of the wave function in the next well layer is large. In the valence band, the subbands which are named as HH1, LH1 and HH2 are also confined in the ZnTe quantum well as in ZnSe(27Å)-ZnS(27Å) SLS.

Figure 6.2 shows the in-plane dispersion of the valence subband at  $k_z=0$  as a function of  $k_{\parallel}$  for ZnTe(10Å)-ZnSe(10Å) SLS, respectively. The solid and dashed curves correspond to the dispersion in the [1,0] and [1,1] direction, respectively. This figure confirms the isotropic feature of the in-plane dispersions in the valence subbands.

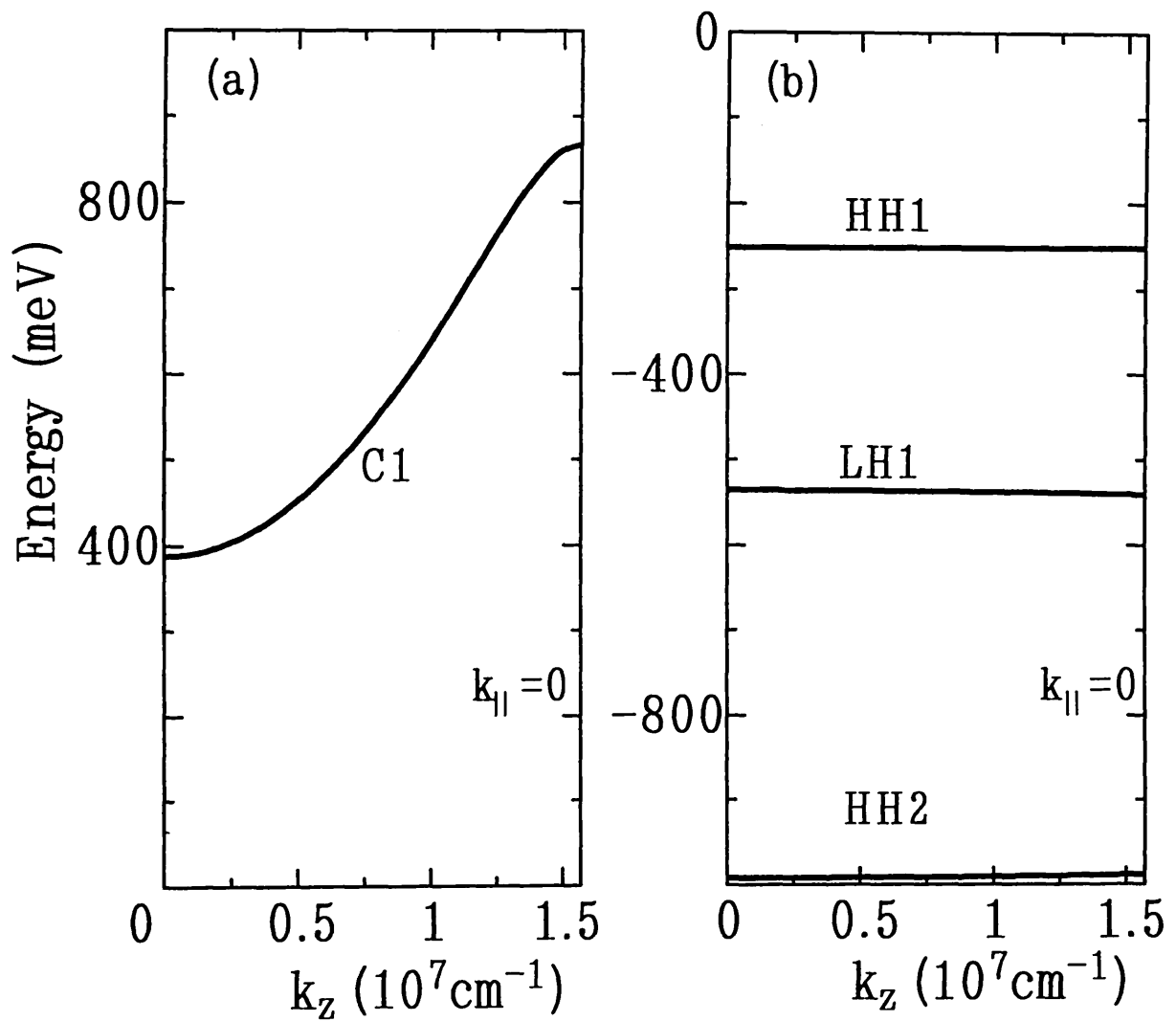


Fig. 6.1. The energy dispersions of conduction subbands (a) and valence subbands (b) in the ZnTe(10Å)-ZnSe(10Å) SLS for  $k_{\parallel} = 0$  as a function of  $k_z$ . The assumed barrier potentials are 896.1 meV for the conduction band and -896.8 meV for the valence band.

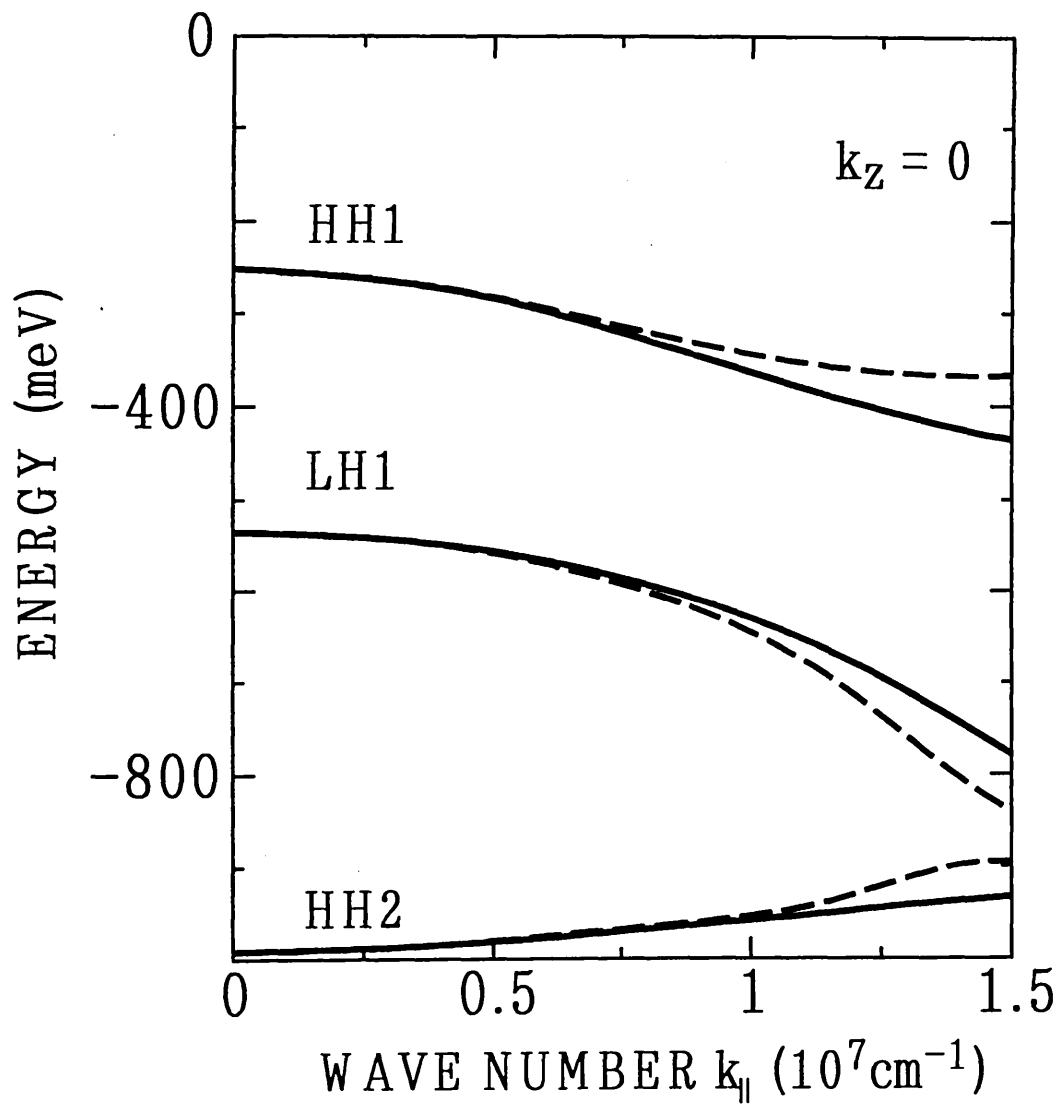


Fig. 6.2. The in-plane dispersions of valence subbands in the ZnTe (10Å)-ZnSe(10Å) SLS as a function of  $k_{||}$  for  $k_z=0$ . The solid and dashed lines represent subband energies in the [1,0] and [1,1] direction, respectively.

### 6.3 Total absorption spectra

Figure 6.3(a) shows the absorption spectrum observed for ZnTe(10Å)-ZnSe(10Å) SLS at room temperature by Shen *et al.*,<sup>40)</sup> and Figs. 6.3(b) and 6.3(c) show the absorption spectra calculated for *TE* and *TM* incident-photon polarizations, respectively. They assigned the first and second experimental bumps to the HH1-C1 and LH1-C1 transition, respectively. Figs. 6.3(b) and 6.3(c) show that our theoretical result supports the validity of their assignment. Since the experiment was carried out at room temperature, excitonic effects are suppressed. Actually, small bumps are found on the experimental HH1-C1 and LH1-C1 spectra, and may be ascribed to weak excitonic effects. Except for these weak excitonic effects, the theoretical absorption spectrum agrees fairly well with the experimental result. These absorption spectra are influenced by strain effects which is larger than that of the ZnSe-ZnS SLS. The energy spacing between HH1-C1 and LH1-C1 transitions amounts to about 300meV.

In Figs. 6.4(a) and 6.4(b), the total absorption spectra for *TE* and *TM* polarizations are decomposed into the band-to-band absorption spectra, respectively. The solid and dashed curves show the band-to-band absorption spectra, which originate from the HH1-C1 and LH1-C1 transitions, respectively, and correspond to the first and second bumps in the total absorption spectra.

### 6.4 Dependence on the polarization and analysis of each transition

In this system, it is remarkable that the total absorption spectra do not show a large difference between *TE* and *TM* polarizations. It is clear that this property results from the band-to-band transitions which do not make a marked difference, as shown in Figs. 6.4(a) and 6.4(b). We explore the reason for this property for the

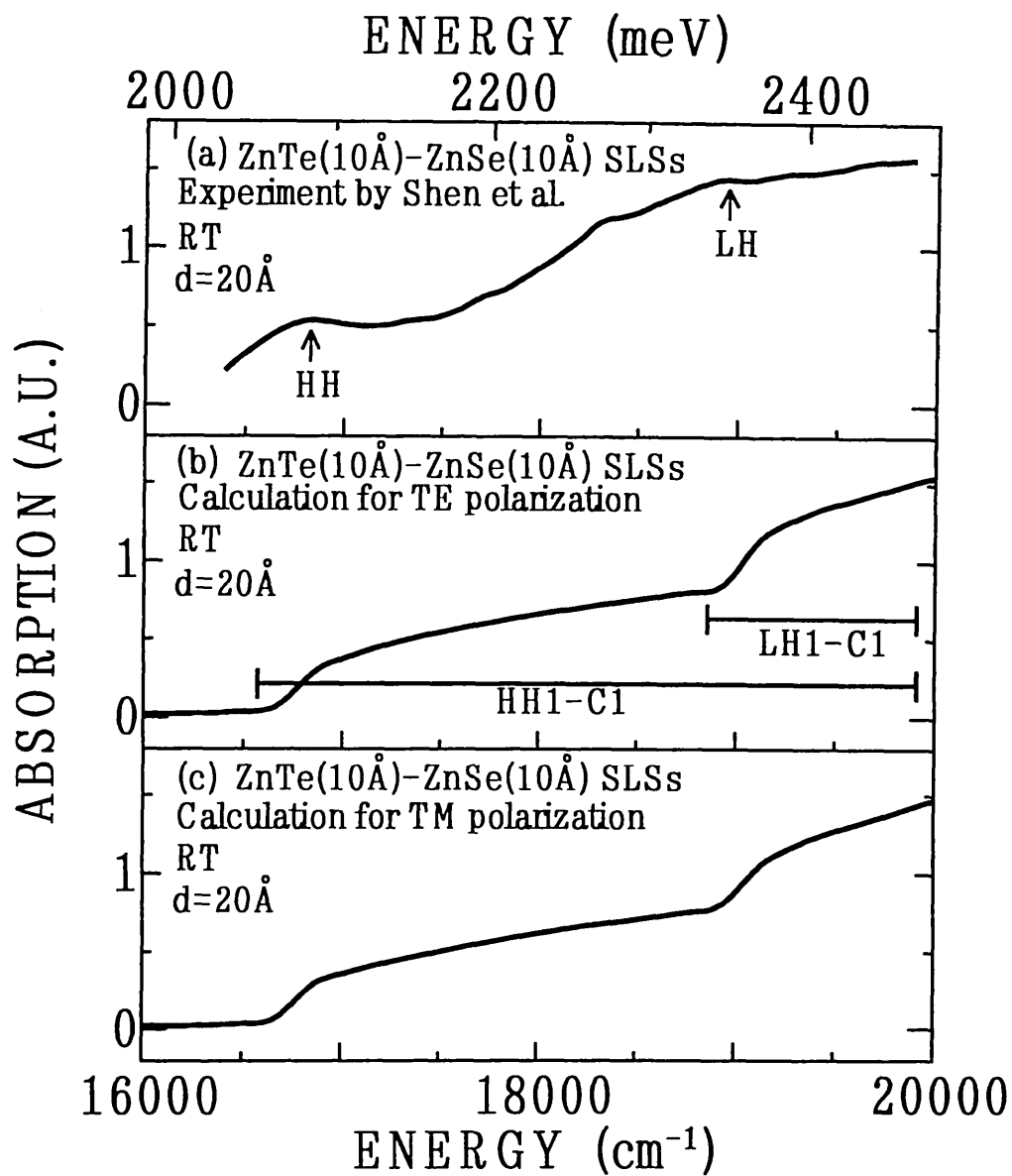


Fig. 6.3. (a) Observed absorption spectra for ZnTe(10Å)-ZnSe(10Å) SLS at room temperature (RT) by Shen *et al.*, and calculated absorption spectra for (b) *TE* and (c) *TM* incident-photon polarizations at RT. HH1-C1 and LH1-C1 denote the transitions from the first heavy- and light-hole subband levels to the first conduction-subband level, respectively. HH and LH indicate the excitonic HH1-C1 and LH1-C1 transitions assigned by Shen *et al.*(ref. 40) The horizontal bar stands for the width of the absorption band associated with each HH1(LH1)-C1 transition.

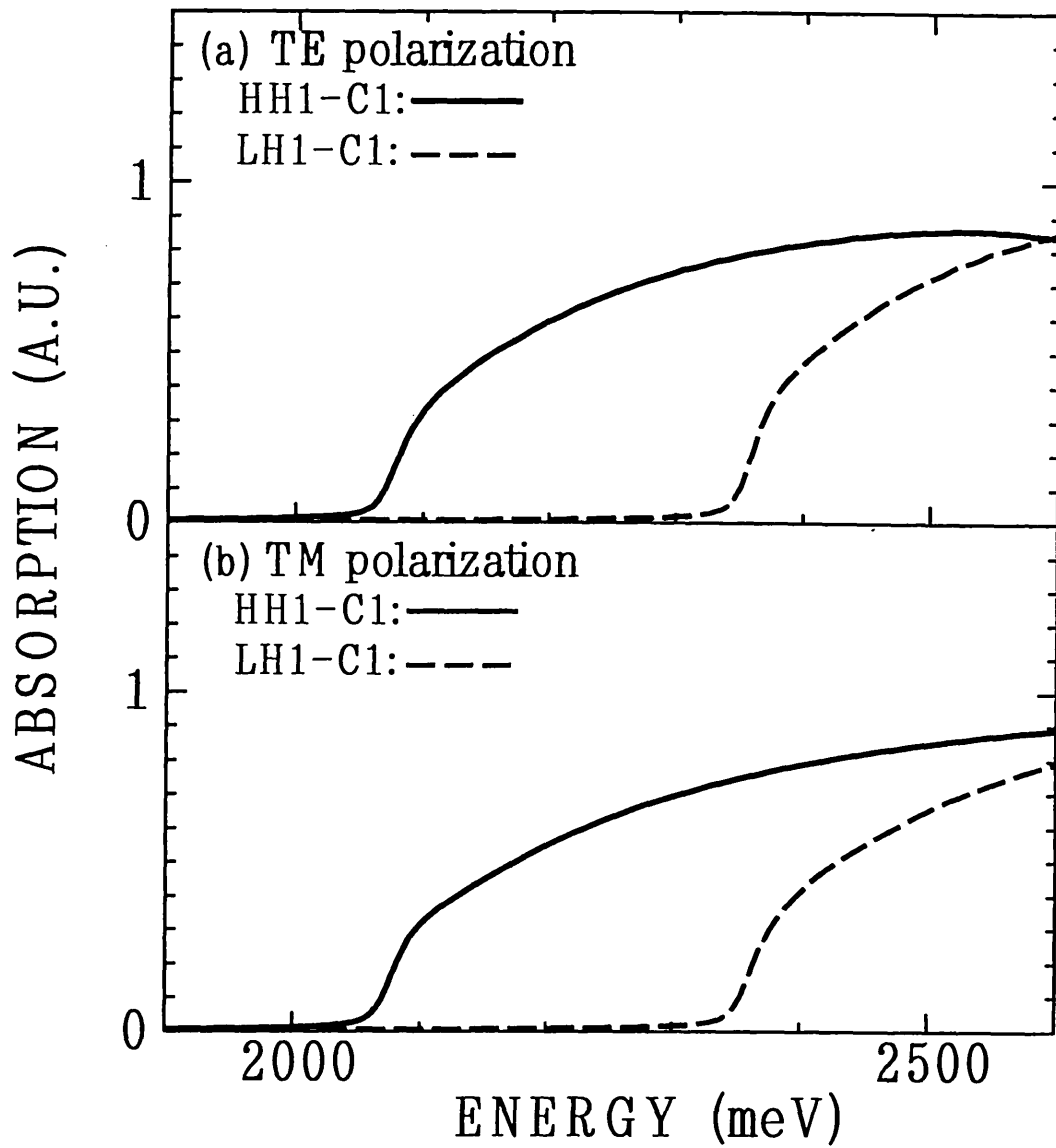


Fig. 6.4. Two subband-to-subband absorption spectra for transitions from the first heavy-hole (HH1) and light-hole (LH1) subband states to the first conduction-subband state (C1) in ZnTe(10Å)-ZnSe(10Å) SLS, which have (a) *TE* and (b) *TM* incident-photon polarizations. HH1-C1 and LH1-C1 absorption spectra are shown by solid and dashed curves.

incident-photon polarizations.

The remarkable character is that the ZnTe(10Å)-ZnSe(10Å) SLS has very thin barrier and well layers. Especially, in the conduction band, the envelope function extends into barrier layers considerably because they are very thin, and the dispersion for  $k_z$  direction is very large as shown in Fig. 6.1(a). This large dispersion makes  $E_{cv}^{(n,m)}(\mathbf{k})$  change considerably as a function of  $k_z$ .  $E_{cv}^{(n,m)}(\mathbf{k})$  for the ZnTe-ZnSe SLS is shown in Figs. 6.5(b) and 6.6(b), which correspond to HH1-C1 and LH1-C1 transitions, respectively. As compared with  $E_{cv}^{(n,m)}(\mathbf{k})$  of ZnSe-ZnS SLS in Figs. 5.5(b) and 5.6(b), it is clear that  $E_{cv}^{(n,m)}(\mathbf{k})$  of the ZnTe-ZnSe SLS depends on  $k_z$  more strongly.

$E_{cv}^{(n,m)}(\mathbf{k})$  determines the form of onset in each band-to-band absorption spectrum. In Fig. 6.7, we decompose the band-to-band absorption spectra into  $k_z$  components. Figures 6.7(a) and 6.7(b), and Figs. 6.7(c) and 6.7(d) correspond to  $TE$  and  $TM$  polarizations, respectively. As compared with those of the ZnSe-ZnS SLS in Fig. 5.9, since the onset energy changes largely with  $k_z$ , the band-to-band absorption spectra do not stand up sharply even for the transition from heavy-hole state which results from the  $TE$  polarization. Therefore, in a specific narrow energy range, the band-to-band absorption spectra do not show a marked difference for the change of the incident-photon polarization.

Figure 6.5(a) and 6.6(a) show  $W_{nmj}(\mathbf{k})$  as a function of  $k_{\parallel}$  and  $k_z$  in the HH1-C1 and LH1-C1 transitions, respectively. Various notations are the same as used in Figs. 5.5~5.7. As shown in Fig. 6.6(a), the ratio of LH to HH is large, and LH and HH components are nearly equivalent above  $2.0 \times 10^7 \text{cm}^{-1}$ . However the behavior of HH and LH components is in sharp contrast. As  $k_{\parallel}$  increases, the HH component decreases, while the LH component increases. In LH1-C1 transition, the ratio of HH to LH also is not negligibly small.

Further,  $W_{nmj}(\mathbf{k})$  for both HH1-C1 and LH1-C1 transitions depends on  $k_z$  largely,

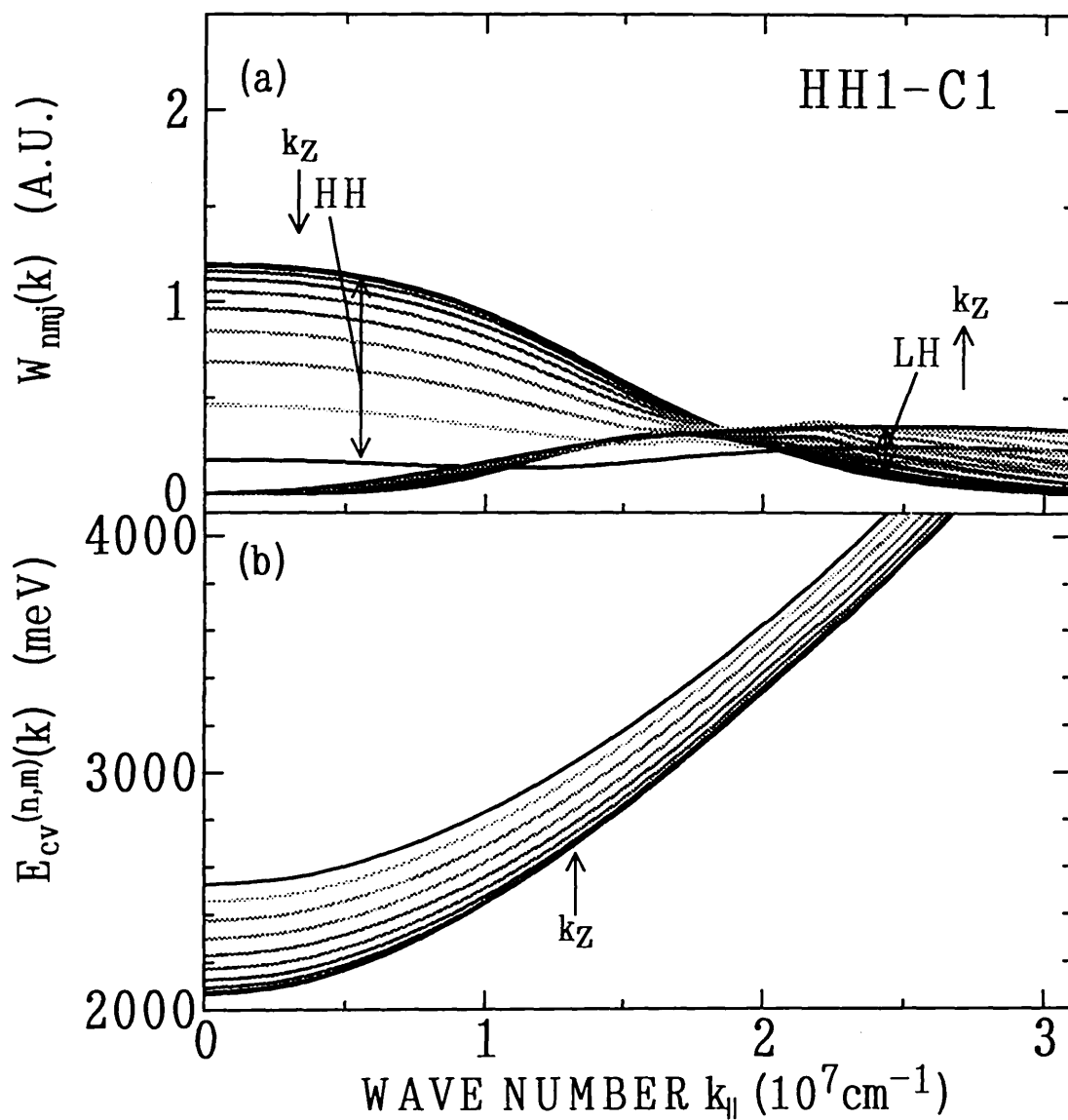


Fig. 6.5. (a) Overlap of envelope functions  $W_{nmj}(k)$  and (b) band gap  $E_{cv}^{(n,m)}(k)$  for HH1-C1 transition in the ZnTe(10Å)-ZnSe(10Å) SLS as a function of  $k_{||}$  and  $k_z$ .  $k_z$  increases in the direction of the arrow.

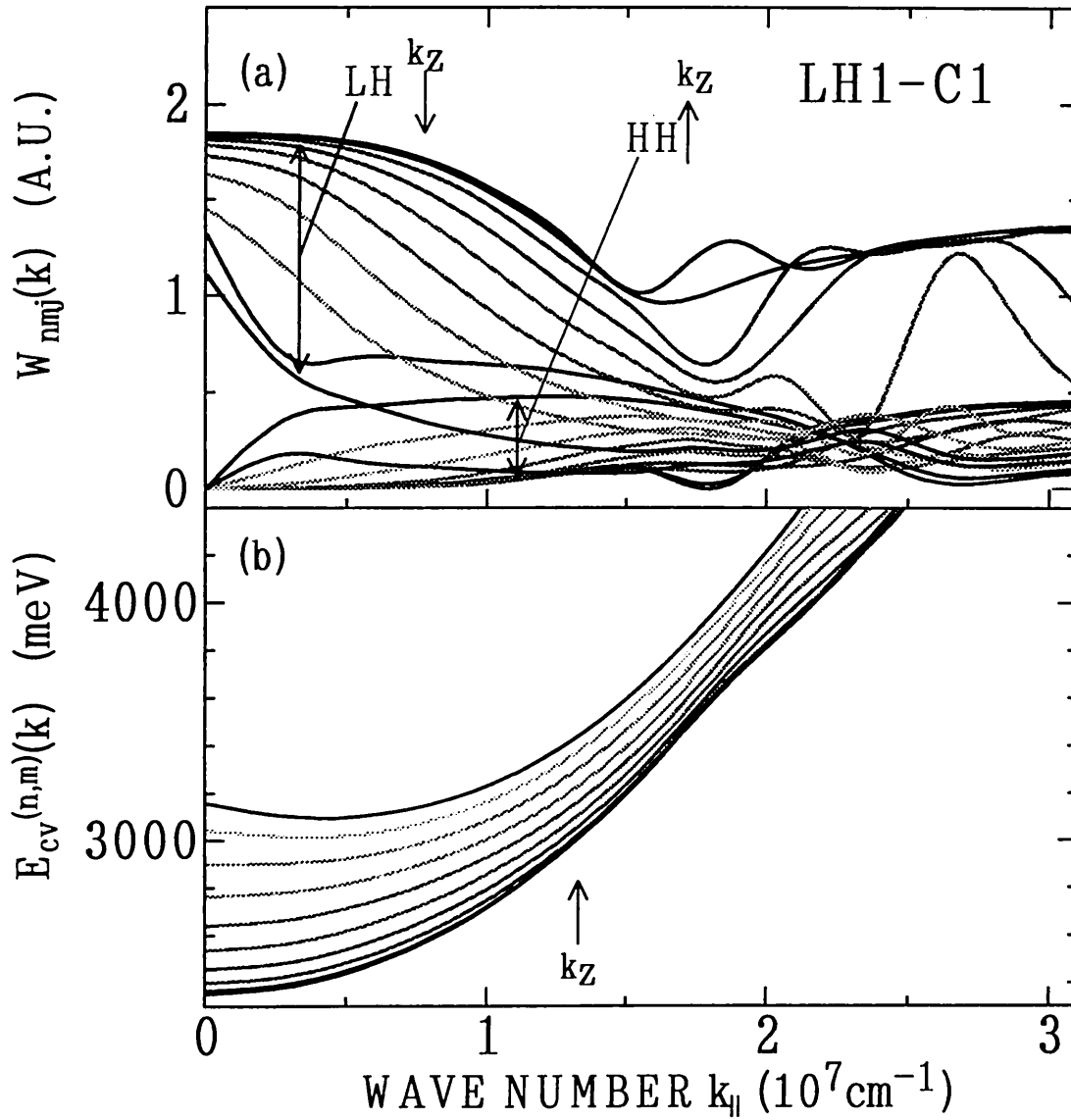


Fig. 6.6. (a) Overlap of envelope functions  $W_{nmj}(\mathbf{k})$  and (b) band gap  $E_{cv}^{(n,m)}(\mathbf{k})$  for LH1-C1 transition in the ZnTe(10Å)-ZnSe(10Å) SLS as a function of  $k_{\parallel}$  and  $k_z$ .  $k_z$  increases in the direction of the arrow.

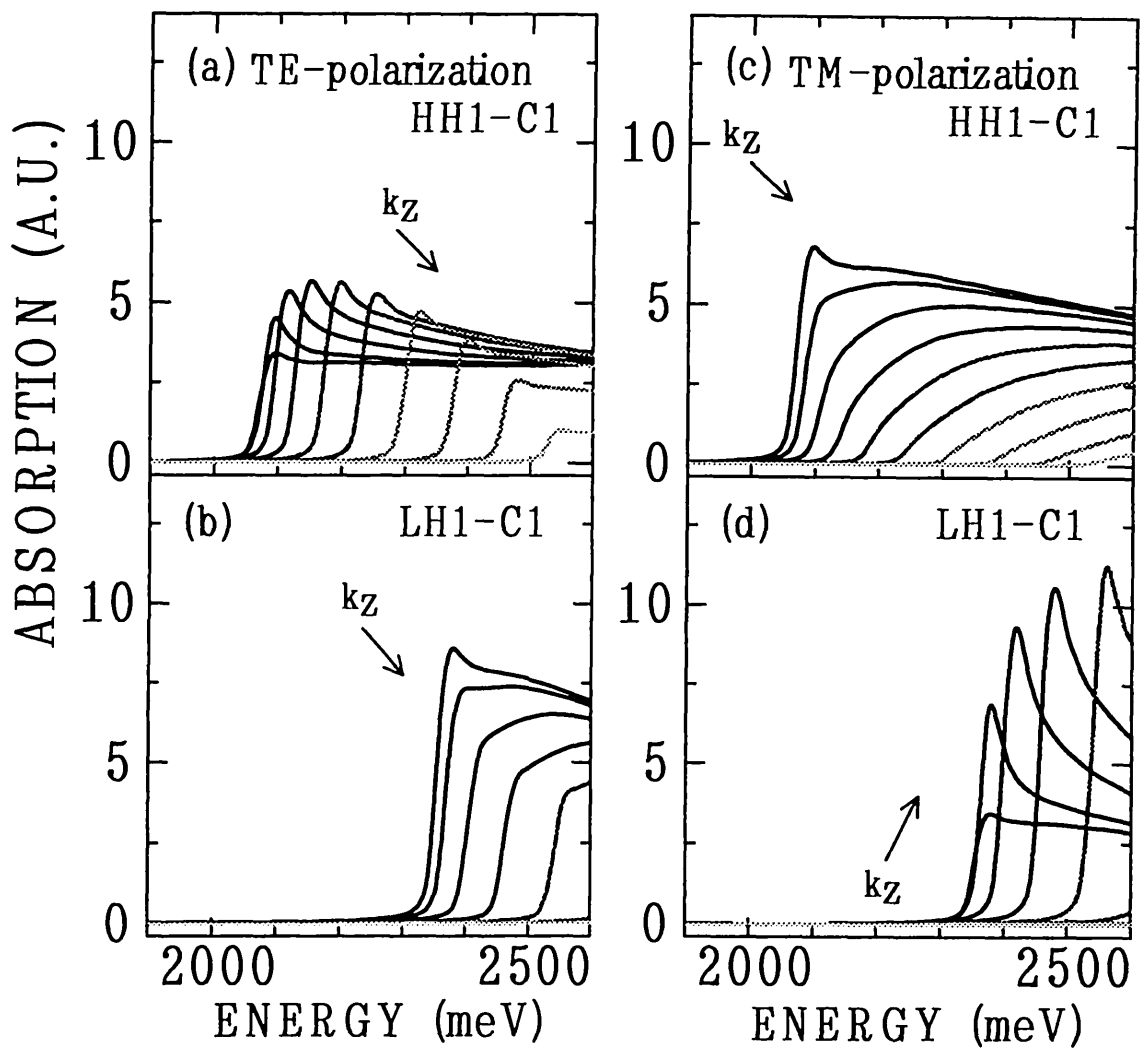


Fig. 6.7. Subband-to-subband absorption spectra decomposed into  $k_z$ -components. (a) and (b), and (c) and (d) denote the *TE* and *TM* incident-photon polarizations, respectively. HH1-C1 and LH1-C1 denote the transitions from the first heavy- and light-hole subband levels to first conduction-subband level, respectively.  $k_z$  increases in the direction of the arrow.

which is the property inherent in type II SLSs including the transition from well layer to barrier layer. Since the mirror plane exists in both well and barrier layers in superlattices, envelope functions in both conduction and valence subbands have different parity at  $k_z=\pi/d$  in type II SLSs even if they have the same parity at  $k_z=0$ .<sup>103,110)</sup>

These property may make possible to design a new optical device on the basis of type II SLSs. In other words, by controlling the thickness of well and barrier layers,  $W_{nmj}(\mathbf{k})$  would change, and, also by controlling the number of period, the possibility to change  $W_{nmj}(\mathbf{k})$  would be got though the symmetry of space is destroyed a little. Thus,  $W_{nmj}(\mathbf{k})$  is made to change by means of using these methods, and this change is not uniform for each transition. Accordingly, by controlling the number of period and the thickness of well and barrier layers, a special component of subband-to-subband absorption spectra may be intensified or weakened by the use of novel transition inherent in type II SLSs.

## 6.5 Conclusions

On the basis of a detailed calculation of the electronic structure in an effective-mass approximation, the optical absorption coefficient is evaluated carefully for the SLS of type II by taking explicitly the  $\mathbf{k}$  dependence of the transition matrix into account. The absorption spectrum is fully examined except for excitonic effects by an analysis of the mixing of the heavy- and light-hole states, and its dependence on the incident-photon polarization is clarified. The theoretical results are compared with the recent experiment on ZnTe-ZnSe SLSs by Shen *et al.*<sup>40)</sup>

In ZnTe(10Å)-ZnSe(10Å) SLS, it is suggested that the observed first and second absorption bumps may be ascribed to the HH1-C1 and LH1-C1 absorption spectra,

respectively. The good agreement between theory and experiment also suggests that our theory may be applied for the substance with the strain effects which is larger than that of the ZnSe-ZnS SLS. Marked differences of absorption spectra between  $TE$  and  $TM$  polarizations are not found in this particular system, because the barrier layer is very thin ( $10\text{\AA}$ ) and  $E_{cv}^{(n,m)}(\mathbf{k})$  depends on  $k_z$  strongly. If experimental studies are carried out on a thick barrier layer, substantial characters of the type II ZnTe-ZnSe SLSs will be observed.

However, by changing our views, the fact that the polarization property of absorption spectra depends on layer thickness may give us a means to control the absorption spectra. Further, a special component of subband-to-subband absorption spectra may be intensified and weakened by the use of novel transition inherent in type II SLSs resulting from the differences of the  $k_z$  dependence of parity between conduction-band and valence-band envelope functions.

# Chapter 7 Calculated Results for Absorption Spectra of ZnSe (22Å)-ZnS(23Å) Strained-Layer Superlattice and Comparison with Experiment

## 7.1 Introduction

ZnSe-ZnS strained-layer superlattices (SLSs) have attracted our attention to their applications for the optoelectronic devices in the blue-spectral region. Many recent experiments in these common-cation superlattices<sup>31-39)</sup> have demonstrated that the absorption spectra exhibit two characteristics. The first one is the appearance of two strong absorption peaks in the vicinity of the fundamental absorption edge, in addition to a few broad bands in the high-energy regime.<sup>34,35,39)</sup> The second is that a structureless increase in a background of absorption as a photon energy increases is seen, instead of a combined profile of the step-like functions (*i.e.* staircase functions) as was observed in GaAs-AlGaAs superlattices.<sup>10)</sup>

Some of experiments<sup>36,38,39)</sup> have suggested that the first and second absorption peaks are attributed to the excitonic transitions from the heavy-hole ground-subband (HH1) and light-hole ground-subband (LH1) to the conduction ground-subband (C1), respectively, whereas Fan *et al.*<sup>35)</sup> have shown that the corresponding two peaks in their spectrum come from the transitions from HH1 and heavy-hole second-subband (HH2) to the C1 and conduction second-subband (C2) with  $\Delta n=0$  selection rule. As is implied by this contradiction as well as the unaccountable second characteristic which intimates a remanence of three-dimensional nature of the density of states,

the present understanding of the excited states associated with the higher subbands remains poor. This is because of the difficulties in computing the electronic states by taking into account the vanishingly small band offset in the conduction band, the lack of knowledge of the effective masses for ZnSe-ZnS SLSs, and the effects of strains on the top of valence bands.

In this chapter, we try to calculate the absorption spectra which originate from vertical valence-band-to-conduction-band transitions in a sufficiently thick SLS sample, i.e. the type I ZnSe(22Å)-ZnS(23Å) SLS, and compare the theoretical results with the experimental results which were measured at RT by Fan *et al.*<sup>35)</sup> As a result, origins of fine structures in the observed absorption spectra can be clarified reasonably well.

Organization of this chapter is as follows. In the next section, results calculated for the electronic structures of conduction and valence bands are shown. In section 7.3, theoretical results for the absorption spectra of the ZnSe(22Å)-ZnS(23Å) SLS are shown, and compared with the experimental results. Finally, conclusions are summarized in section 7.4.

## 7.2 Results for the electronic structures

As was described in Chap.3, the electronic structure is calculated also for the ZnSe(22Å)-ZnS(23Å) SLS by using the potential parameters as shown in Table 3.1. Note that we have used the experimental value for the band gap which has been measured at RT in accordance with the optical measurement by Fan *et al.*<sup>35)</sup>

Figure 7.1 shows the electronic structures calculated for the ZnSe(22Å)-ZnS(23Å) SLS. (a) and (b) show the conduction- and valence-subband dispersions for  $k_{\parallel}=0$  as a function of  $k_z$ , respectively. In the conduction band, the  $i$ th subband is named as  $C_i$ . In the valence band,  $HH_i$  or  $LH_i$  means the subband which is reduced at  $k=0$  to the

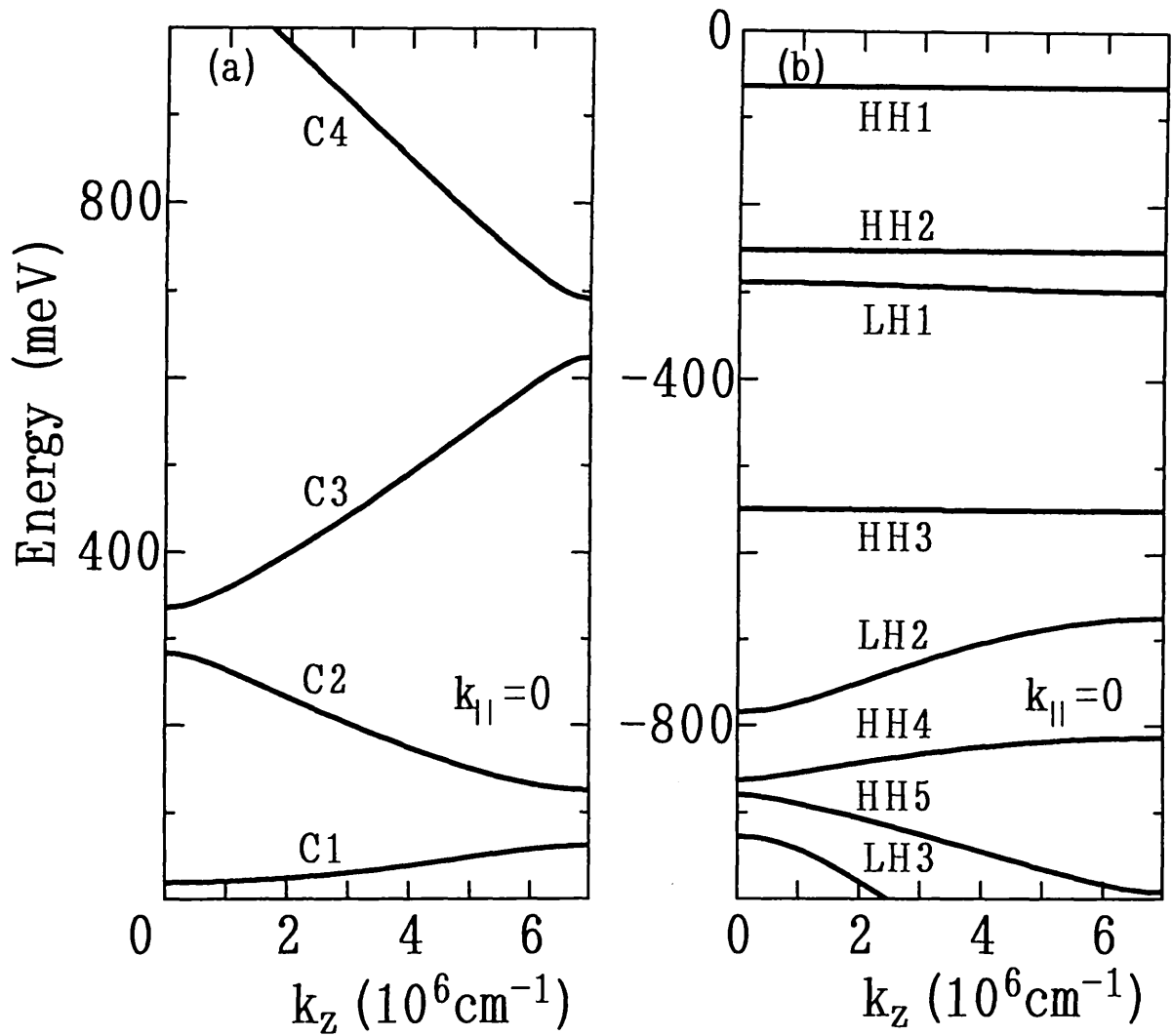


Fig. 7.1. The energy dispersions of (a) conduction subbands and (b) valence subbands in the ZnSe(22Å)-ZnS(23Å) SLS for  $k_{||}=0$  as a function of  $k_z$ . The barrier potentials are 40.3meV for the conduction band and -681.2meV for the valence band.

$i$ th heavy- or  $i$ th light-hole state, respectively. In the calculation, various potential parameters are evaluated by taking account of strain effects; barrier potentials are 40.3meV for the conduction band and  $-681.2\text{meV}$  for the valence band, and shear deformation potentials are  $-65.0\text{meV}$  for ZnSe layer and  $39.7\text{meV}$  for the ZnS layer.

As shown in Fig. 7.1, the higher conduction subband has the larger dispersion, while the valence subbands are almost dispersionless. These properties resemble those for ZnSe(27Å)-ZnS(27Å) SLS. However, for this SLS, we used the band gap measured at RT which is more narrow than that at low temperature. In result, barrier potential in the valence band become low, the energy spacings between valence subbands get narrow, and eight subband levels, therefore, are included within the energy scale from  $-1000\text{meV}$  to  $0\text{meV}$ . The strain effect is also similar to that of ZnSe(27Å)-ZnS(27Å) SLS, and the HH2 subband becomes higher than the LH1 subband because the shear deformation potential in the valence band has a large value.

Figure 7.2 shows the in-plane dispersion of the valence subband at  $k_z=0$  as a function of  $k_{\parallel}$  for ZnSe(22Å)-ZnS(23Å) SLS, respectively. The solid and dashed curves correspond to the dispersion in the [1,0] and [1,1] direction, respectively. This figure confirms the isotropic feature of the in-plane dispersions in the valence subbands.

### 7.3 Absorption spectra

Here we calculate the total absorption coefficient for type I ZnSe(22Å)-ZnS(23Å) SLS by summing over all of the individual band-to-band absorption coefficients, as was described in Chap.4, and compare the theoretical result with the experimental absorption spectrum which has been measured at RT by Fan *et al.*<sup>35)</sup>

Figure 7.3(a) shows the experimental result observed in ZnSe(22Å)-ZnS(23Å) SLS at RT on the  $TE$  polarization condition by Fan *et al.*<sup>35)</sup> They assigned  $n=i$  HH and  $n=i$  LH to the HH $i$ -C $i$  and LH $i$ -C $i$  transitions, respectively, where  $i=1$  and 2. Figures

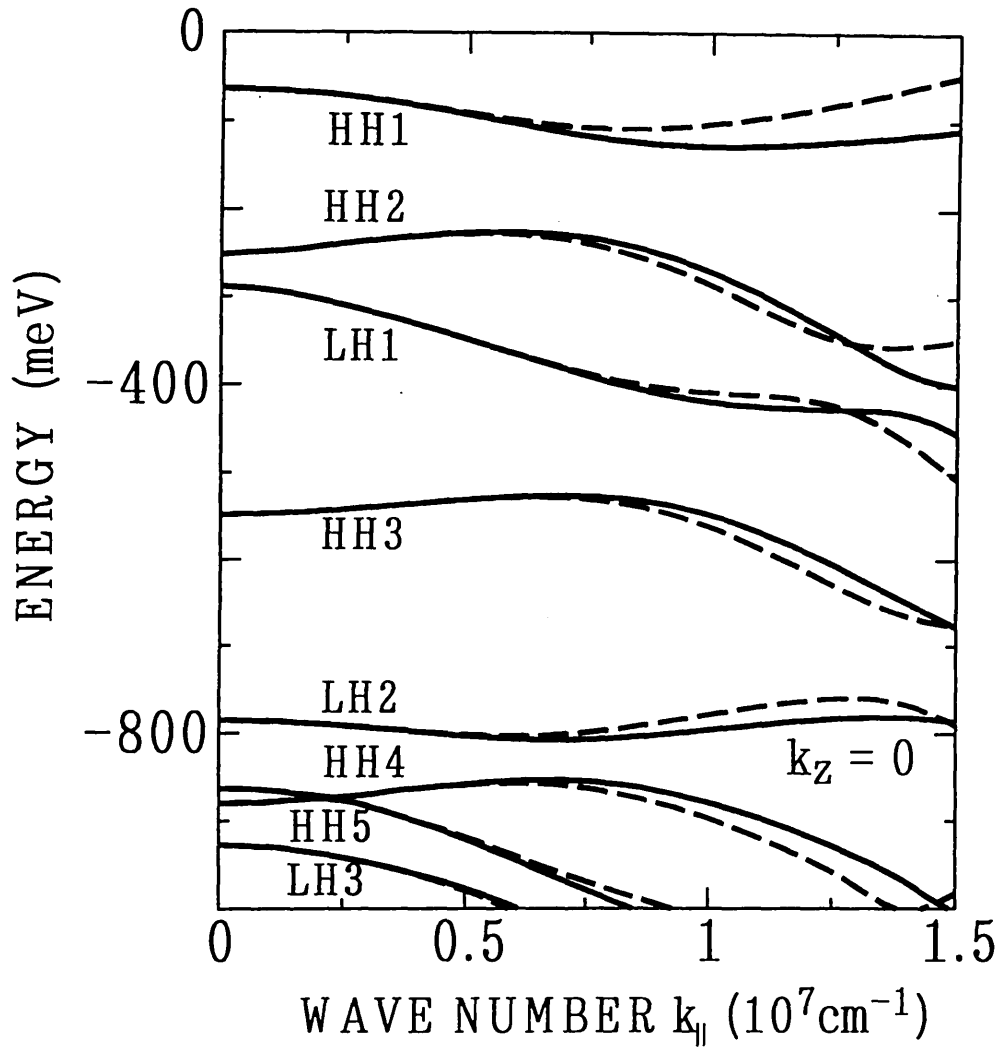


Fig. 7.2. The in-plane dispersions of valence subbands in the ZnSe (22Å)-ZnS(23Å) SLS as a function of  $k_{||}$  for  $k_z=0$ . The solid and dashed lines represent subband energies in the [1,0] and [1,1] direction, respectively.

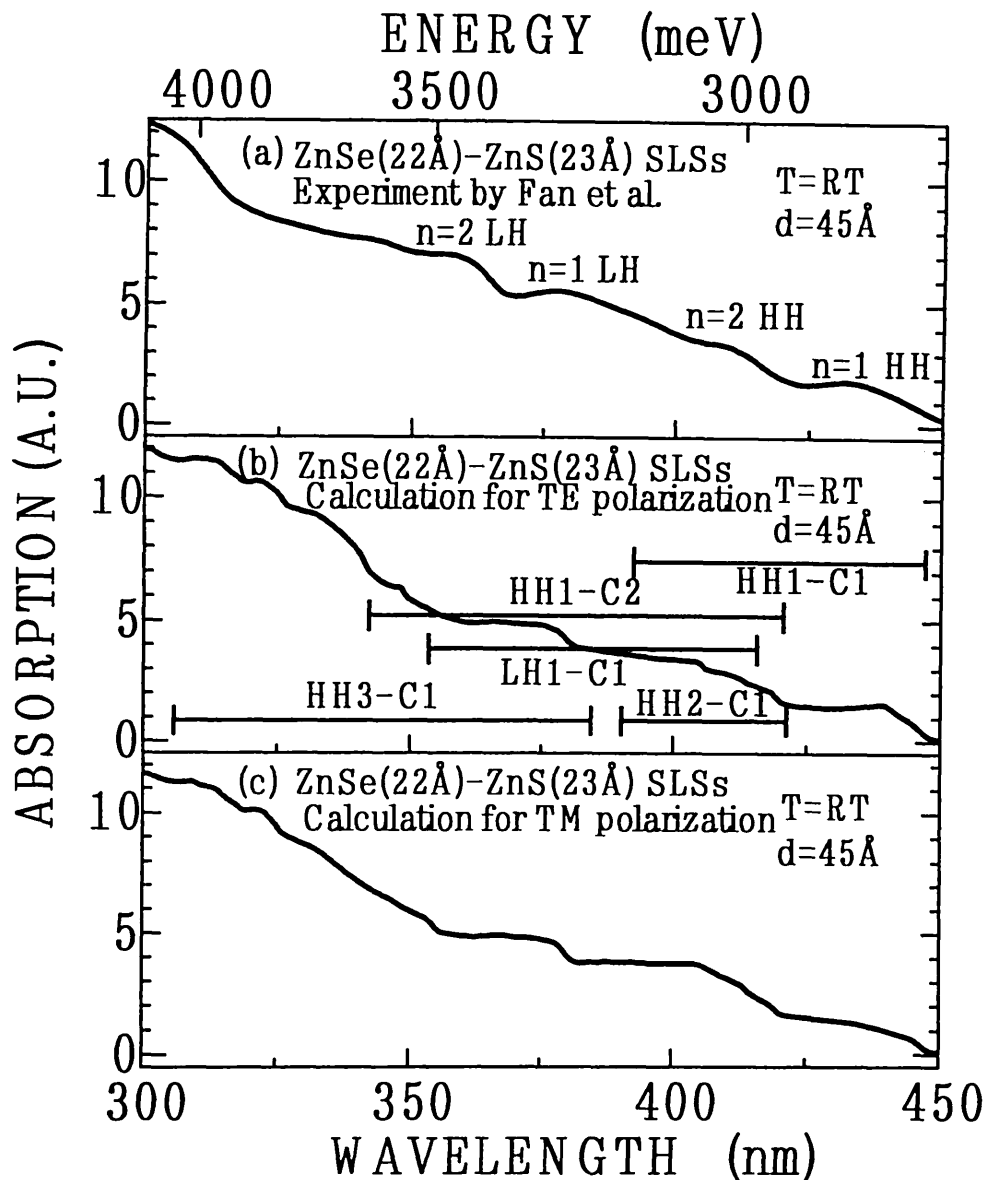


Fig. 7.3. (a) Absorption spectra observed in ZnSe(22Å)-ZnS(23Å) SLS at room temperature by Fan *et al.*(ref. 35), and absorption spectra calculated for (b) *TE* and (c) *TM* incident-photon polarizations.  $HH_j-C_i$  and  $LH_j-C_i$  denote the transitions from the  $j$ th heavy- and light-hole subband levels to  $i$ th conduction-subband level, respectively.  $n=j$  HH and  $n=j$  LH indicate the excitonic  $HH_j-C_1$  and  $LH_j-C_1$  transitions assigned by Fan *et al.*(ref. 35) The horizontal bar stands for the width of the absorption band associated with each  $HH_j(LH_j)-C_j$  transition.

7.3(b) and 7.3(c) show the total absorption coefficients calculated for ZnSe(22Å)-ZnS(23Å) SLS for  $TE$  and  $TM$  polarizations, respectively.  $HHj-Ci$  and  $LHj-Ci$  denote the transitions from the  $j$ th heavy- and light-hole subband levels to the  $i$ th conduction-subband level, respectively. The calculated absorption spectrum in Fig. 7.3(b) reproduces the features of the experimental result in a low-energy side very well.<sup>35)</sup> However, a close comparison between Figs. 7.3(a) and 7.3(b) reveals conspicuous discrepancies in a high-energy side. These discrepancies may be attributed to exceeding the limit of the effective-mass approximation and ignoring spin-orbit split-off bands in this calculation. Though they may exist in experimental absorption spectra at RT, excitonic effects<sup>45)</sup> are so small that we cannot separate them.

In Figs. 7.4(a) and 7.4(b), the total absorption spectra are decomposed into band-to-band absorption spectra for  $TE$  and  $TM$  incident-photon polarizations, respectively. Band-to-band absorption spectra corresponding to HH1-C1, LH1-C1, HH1-C2 and HH2-C1 transitions form main bumps in the total absorption spectra. We have confirmed that the first observed curve (i.e.  $n=1$  HH) can be assigned to the onset of HH1-C1 transition. The second experimental bump (i.e.  $n=2$  HH) corresponds to the onset of HH2-C1, HH1-C2 and LH1-C1 transitions, and the left shoulders of HH1-C1 transition. Though HH2-C2 transition also appears near the second experimental bump, the strength for the HH2-C2 transition is one order of magnitude less than that of the HH1-C1 band, so that it cannot contribute appreciably to the second experimental bump. HH1-C2 and HH2-C1 transitions are neglected usually, but their existence is clearly seen in Figs. 7.4(a) and 7.4(b). The third experimental bump (i.e.  $n=1$  LH) mainly consists of the left shoulder of LH1-C1 transition.

The left shoulders in HH1-C1 and LH1-C1 absorption spectra consist of the mixing between heavy- and light-hole states,<sup>49)</sup> and influence bumps in the energy range from about 375nm to about 425nm in Figs. 7.3(b) and 7.3(c). HH2-C1 and HH1-C2

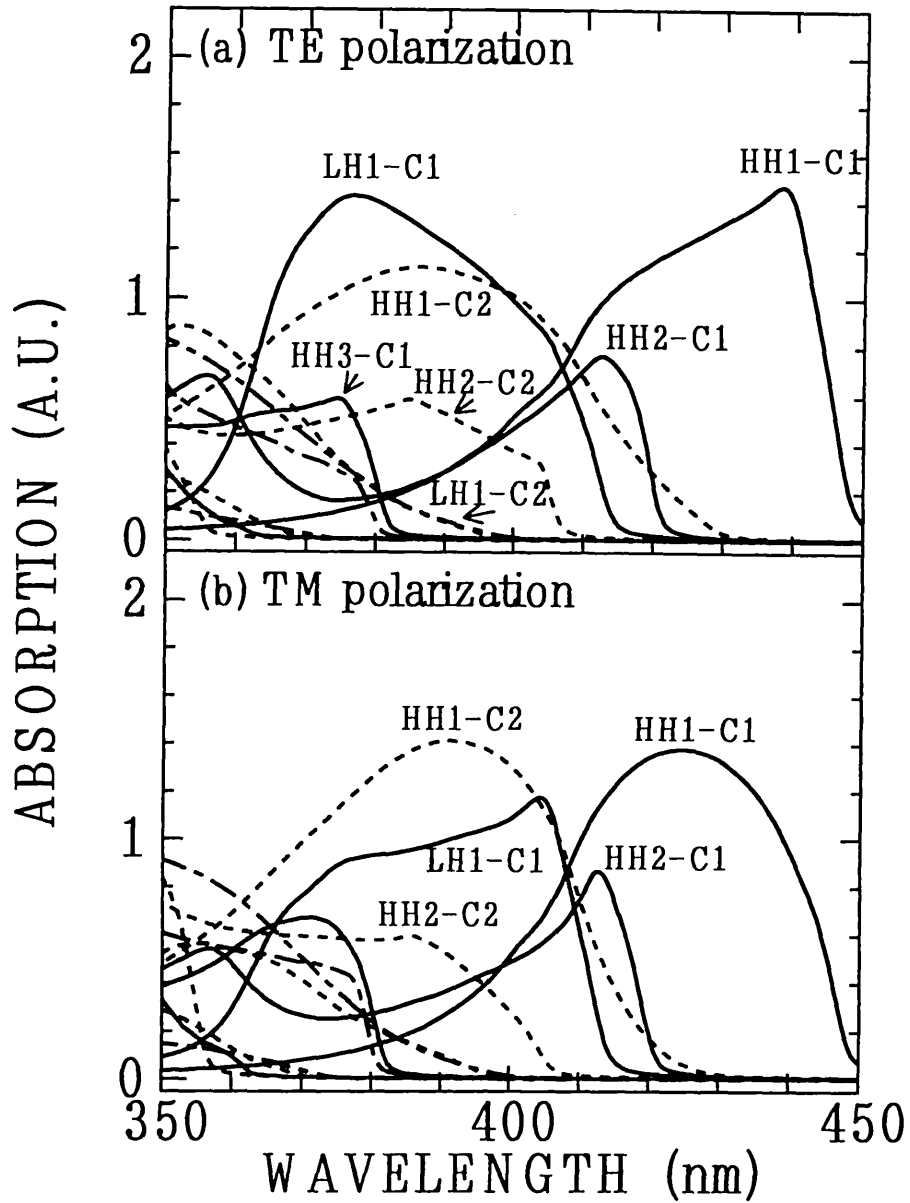


Fig. 7.4. Subband-to-subband absorption spectra in ZnSe(22Å)-ZnS (23Å) SLS corresponding to (a) *TE* and (b) *TM* incident-photon polarizations.  $HH_j-C_i$  and  $LH_j-C_i$  denote the transitions from the  $j$ th heavy- and light-hole subband levels to  $i$ th conduction-subband level, respectively.

absorption spectra influence the bumps from about 375nm to about 420nm and from about 340nm to about 420nm in the total absorption spectra, respectively.

We also examine the dependence of the main absorption components on the polarization. It is evident from Figs. 7.3(b) and 7.3(c) that the overall profile of the absorption spectrum is modified greatly by changing the polarization from  $TE$  to  $TM$ . In the absorption band around 450nm, the intensity for  $TM$  polarization is smaller than that for  $TE$  polarization. As shown in Figs. 7.4(a) and 7.4(b), LH1-C1 absorption spectra have obviously the polarization dependence which originates from the left shoulders influenced by the mixing effects. These differences are driven by the polarization properties of  $G_{Pj}$  in the integrand of eq.(4.7),<sup>49)</sup> and the heavy-hole component in  $TM$  polarization become weaker than that in  $TE$  polarization.

Further, these absorption spectra are influenced by large strain effects. The energy spacing between HH1-C1 and LH1-C1 transitions exceeds 200meV, because the splitting energy between the heavy- and light-hole states and the difference between the potential barriers which result from the shear deformation potential are very large.

## 7.4 Conclusions

The absorption spectra observed at RT for the type I ZnSe(22Å)-ZnS(23Å) SLS by Fan *et al.*<sup>35)</sup> can be explained satisfactorily by the calculation of the absorption coefficients which takes the vertical valence-band-to-conduction-band transitions into account. In a high-energy side, however, there are some conspicuous discrepancies, which may be ascribed to the limitation of the effective-mass approximation and/or the neglect of the spin-orbit split-off bands.

# Chapter 8    Calculated Results for Absorption Spectra of Type I ZnSe(20Å)-ZnS(20Å) and Type II ZnTe(20Å)-ZnSe(20Å) Strained-Layer Suparlattice

## 8.1 Introduction

Strained-layer superlattices (SLSs) composed of II-VI compounds, such as ZnS, ZnSe and ZnTe, have recently attracted considerable attention due to the possibility of the formation of blue light emitting lasers. Associated with these SLSs, there are many optical experiments<sup>31-44)</sup> and theoretical works<sup>45-51)</sup> in which the excitonic luminescence as well as the absorption are studied extensively. In this chapter, we calculate some optical absorption spectra of type I ZnSe-ZnS SLSs and type II ZnTe-ZnSe SLSs by using band gap measured at room temperature (RT) with special emphasis on the differences of absorption spectra.

A calculation of the electronic structure of the conduction and valence subbands is carried out by using the Luttinger-Kohn Hamiltonian<sup>52,53)</sup> in the Kronig-Penney model, in which the periodic change of the effective mass and the strain in the well and barrier layers is taken into account. The absorption coefficients due to the vertical valence-band-to-conduction-band transitions are evaluated by taking the electronic structure fully into account. It is expected that the type I and the type II SLSs may have different characteristic properties in the absorption spectra, because they reflect the electronic structure very sensitively.

Within this theoretical scheme, we have already calculated the absorption spectra

at low temperature for various SLSs of both types, such as the type I ZnSe(20Å)-ZnS(20Å),<sup>50)</sup> the type II ZnTe(20Å)-ZnSe(20Å),<sup>50)</sup> and the type I ZnSe(27Å)-ZnS(27Å) SLS,<sup>48,49)</sup> and found that theoretical absorption spectra can explain origins of fine structures in the experimental absorption spectra reasonably well. At low temperatures, however, it is not easy to test the validity of our theoretical results, because the experimental absorption spectra may be influenced by excitonic effects which are not taken into account in our calculation of the absorption spectra.

Though a study on excitonic effects is itself important physics, we want to explore characteristic properties of the optical absorption which originates from the vertical valence-band-to-conduction-band transitions in SLSs without being disturbed by excitonic effects. We expect that our aim may be achieved by comparing theoretical absorption spectra with experimental ones observed at high temperatures where excitonic effects are much reduced. In Chaps. 6 and 7, we have already carried out a calculation on the type II ZnTe(10Å)-ZnSe(10Å) SLS and the type I ZnSe(22Å)-ZnS(23Å) SLS, and tried to compare theoretical results with the absorption spectra observed at RT. Unfortunately, however, the well and barrier layers of this particular type II sample in Chap. 6 are so thin that any interesting characteristics cannot be found.

In this chapter, we try to calculate the absorption spectra which originate from vertical valence-band-to-conduction-band transitions in a sufficiently thick SLS sample, i.e. the type I ZnSe(20Å)-ZnS(20Å) and type II ZnTe(20Å)-ZnSe(20Å) SLSs. From results of Chaps. 6 and 7, we judge that the reliability of our theory is confirmed, so that we next apply it to the prediction of a marked difference between absorption spectra of type I and type II SLSs with the well and barrier layers of the same thickness.

The SLSs for which we calculate absorption spectra are the type I ZnSe(20Å)-

ZnS(20Å) and ZnTe(20Å)-ZnSe(20Å) SLSs whose well and barrier layers have the same thickness. As a result of a detailed analysis, a marked difference is found between absorption spectra in these type I and type II SLSs, and an origin of the main difference can be clarified on the basis of their electronic structures. We also examine the dependence of the absorption spectra on the incident-photon polarization. The polarization which we consider is a transverse electric field and a transverse magnetic field in which the electric field vector of incident light is oriented perpendicular to and along the growth direction, respectively. It is revealed that the use of these different polarizations causes a drastic change in the absorption spectra both in type I and type II SLSs.

Organization of this chapter is as follows. In section 8.2, Electronic structures are calculated and explained. In section 8.3, theoretical absorption spectra for type I and type II SLSs are explained, and characteristic differences between them are revealed. In section 8.4, we show the dependence on the incident-photon polarization of type I and type II SLSs. Finally, conclusions are summarized in section 8.5.

## 8.2 Results for the electronic structures

The electronic structure is calculated for type I ZnSe(20Å)-ZnS(20Å) and type II ZnTe(20Å)-ZnSe(20Å) SLSs within the framework of the effective-mass approximation which was described in Chap.3. In the actual calculation, we use various potential parameters which are determined by taking strain effects into account; barrier potentials are 40.3meV and 896.1meV for the conduction band and  $-678.1\text{meV}$  and 896.8meV for the valence band in the ZnSe-ZnS and the ZnTe-ZnSe SLSs, respectively, and shear deformation potentials are  $-63.7\text{meV}$  for ZnSe layer and 40.6meV for the ZnS layer in the ZnSe-ZnS SLS, and  $-117.8\text{meV}$  for the ZnTe layer and

97.3meV for the ZnSe layer in the ZnTe-ZnSe SLS. These values which we used in our calculation are shown in Table 3.1. In particular, we have used the experimental value for the band gap which has been measured at RT for each bulk material. Here we explain the results for ZnSe(20Å)-ZnS(20Å) and ZnTe(20Å)-ZnSe(20Å) SLSs with equal thickness, and try to clarify the differences between the electronic structures in these two SLSs. These results will be used to investigate the characteristic differences between absorption spectra in these SLSs in section 8.3.

Figures 8.1 ~ 8.4 show the electronic structures calculated for the ZnSe(20Å)-ZnS(20Å) and the ZnTe(20Å)-ZnSe(20Å) SLSs, respectively. In Figs. 8.1 and 8.2, (a) and (b) show the conduction- and valence-subband dispersions for  $k_{\parallel}=0$  as a function of  $k_z$ , respectively, and Figs. 8.3 and 8.4 show those for  $k_z=0$  as a function of  $k_{\parallel}$ , respectively. We choose the growth direction as the  $z$  axis. In the conduction band, the  $i$ th subband is named as  $C_i$ . In the valence band,  $HH_i$  or  $LH_i$  means the subband which is reduced at  $\mathbf{k}=0$  to the  $i$ th heavy- or  $i$ th light-hole state, respectively.

Figure 8.1 shows that in the ZnSe-ZnS SLS the higher conduction subband has the larger dispersion, while the valence subbands (i.e.  $HH_1$ ,  $HH_2$ ,  $LH_1$  and  $HH_3$ ) within the barrier potential are almost dispersionless. These band structures imply an extended nature of the conduction subbands in the SLS and a confinement of the valence-band states within the ZnSe quantum well. The optical band-to-band transitions from the confined hole states to the free-electron-like high conduction subbands may lead to the continuous absorption background. This is similar to the optical joint density of states in a three-dimensional semiconductor where both the conduction- and valence-band states are described by the parabolic energy dispersions. Furthermore, the  $HH_2$  subband becomes higher than the  $LH_1$  subband, because the shear deformation potential in the valence band has a large value.

As shown in Figs. 8.2(a) and 8.2(b), a remarkable character of the electronic

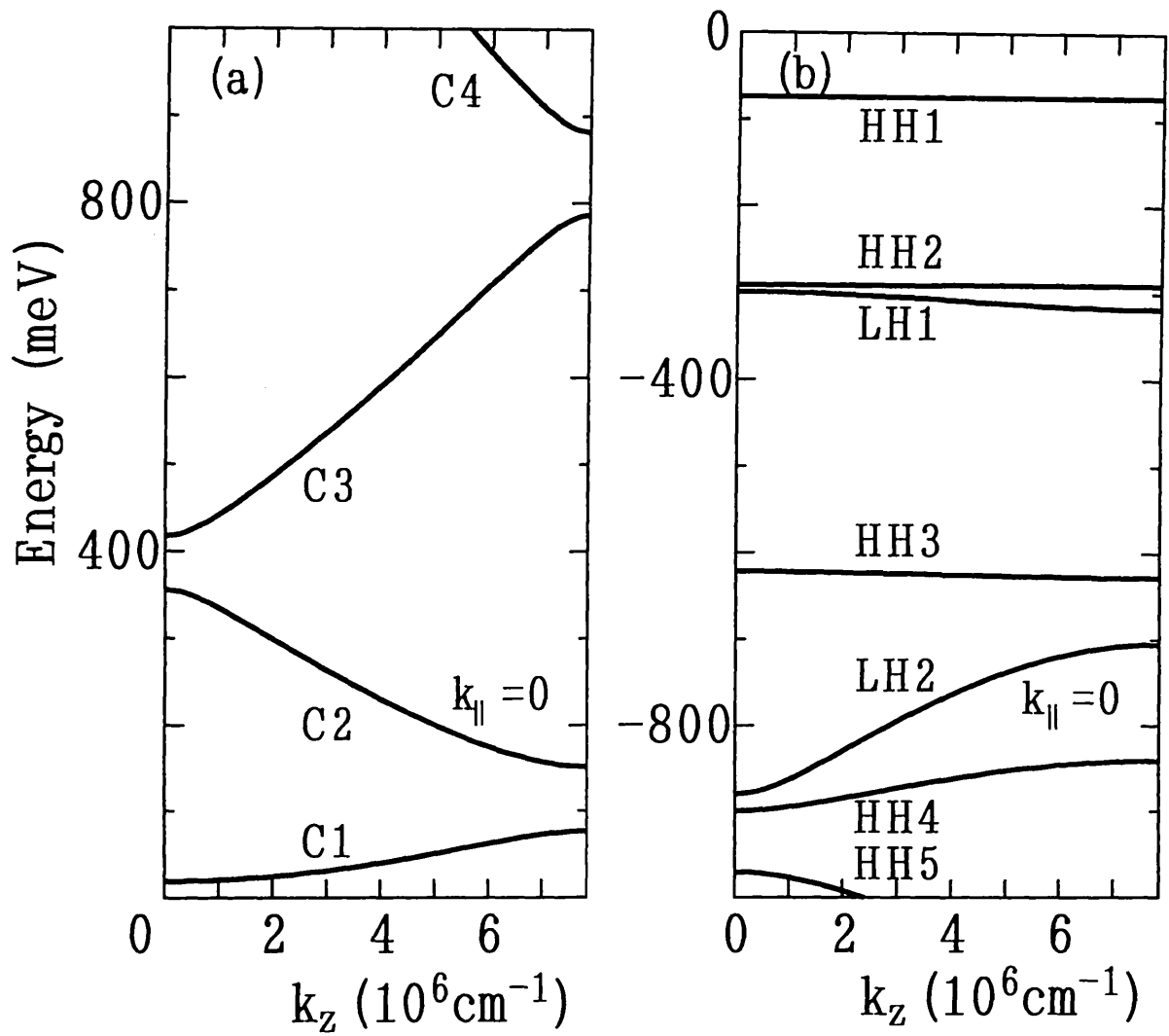


Fig. 8.1. The energy dispersions of (a) conduction subbands and (b) valence subbands in the ZnSe(20Å)-ZnS(20Å) SLS for  $k_{||}=0$  as a function of  $k_z$ . The barrier potentials are 40.3meV for the conduction band and -678.1meV for the valence band.

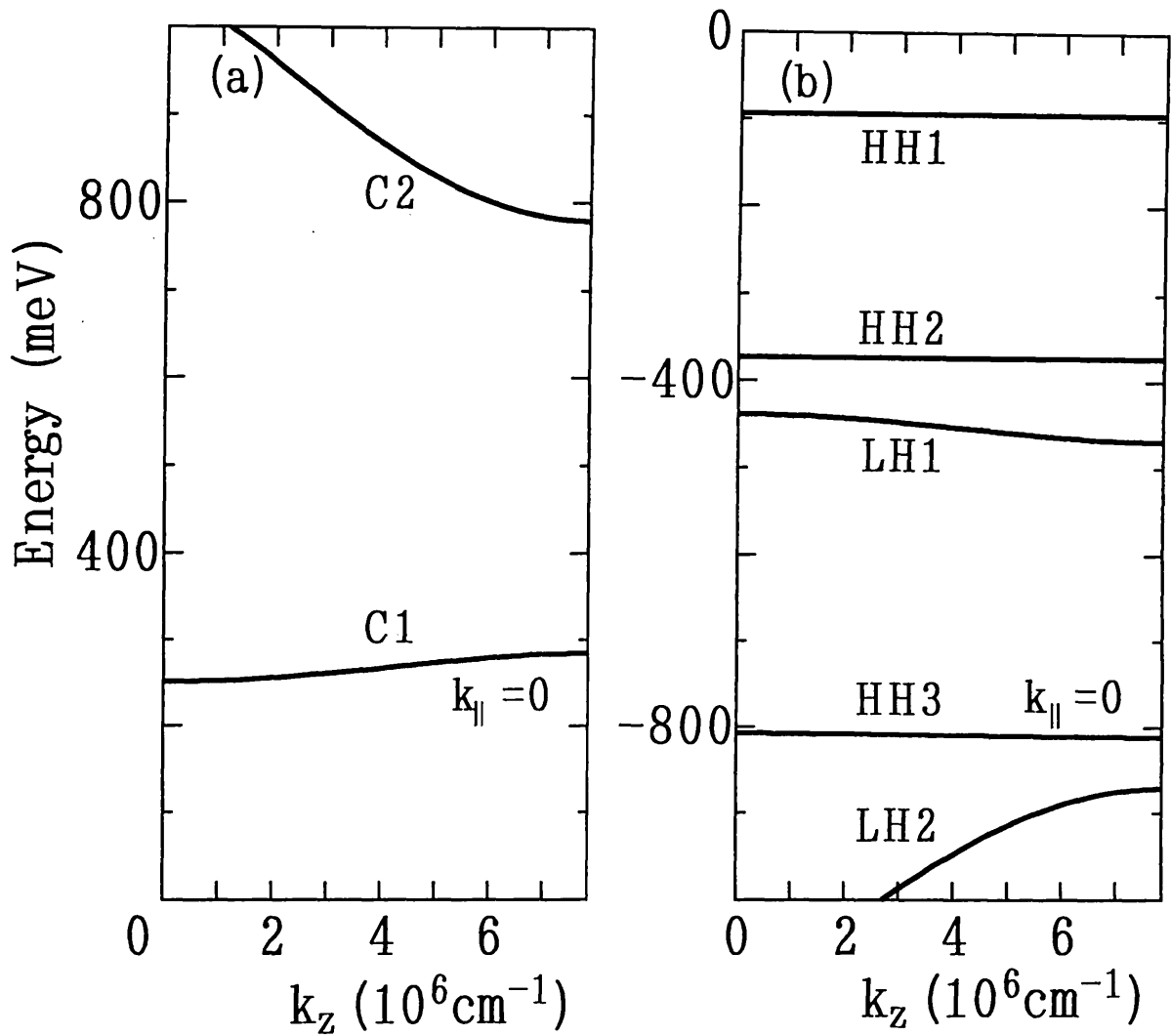


Fig. 8.2. The energy dispersions of (a) conduction subbands and (b) valence subbands in the ZnTe(20Å)-ZnSe(20Å) SLS for  $k_{\parallel}=0$  as a function of  $k_z$ . The barrier potentials are 896.1meV for the conduction band and -896.8meV for the valence band.

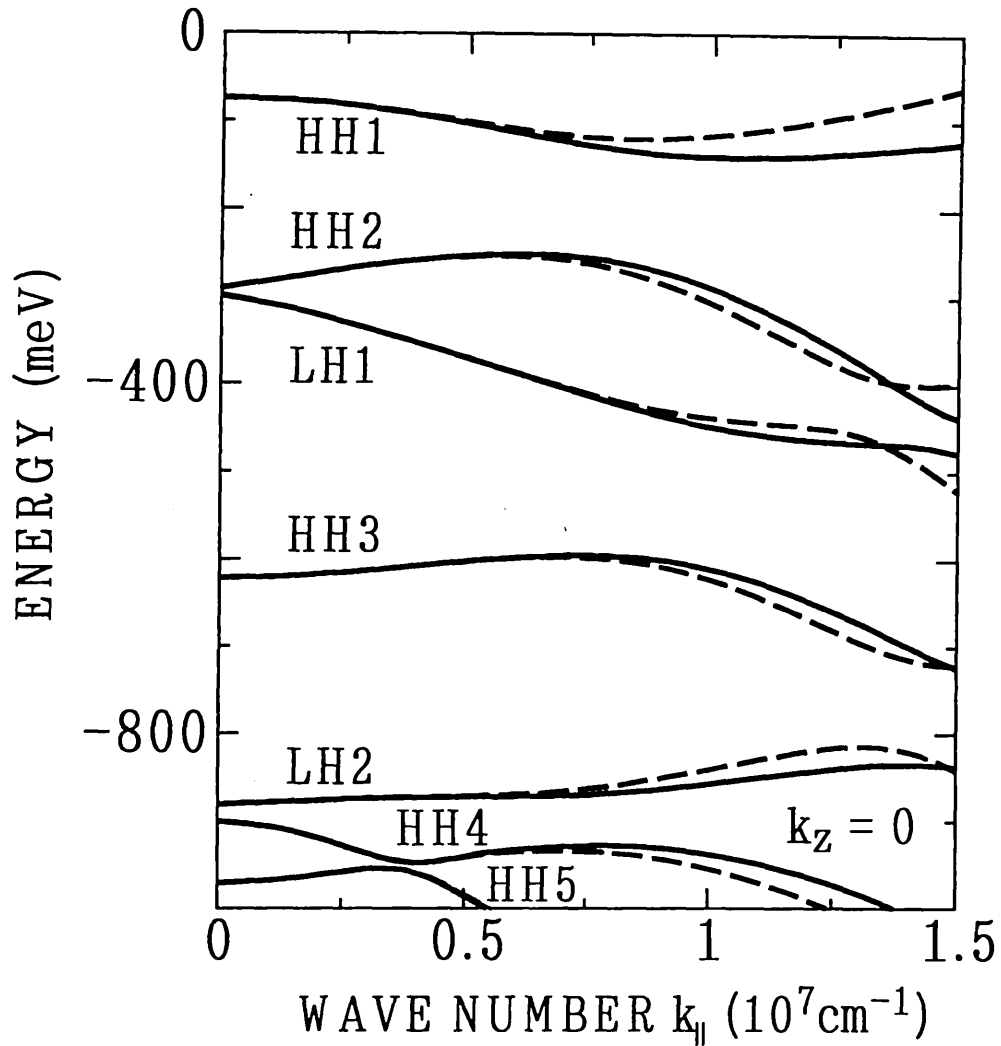


Fig. 8.3. The in-plane dispersions of valence subbands in the ZnSe(20Å)-ZnS(20Å) SLS as a function of  $k_{||}$  for  $k_z=0$ . The solid and dashed lines represent subband energies in the [1,0] and [1,1] direction, respectively.

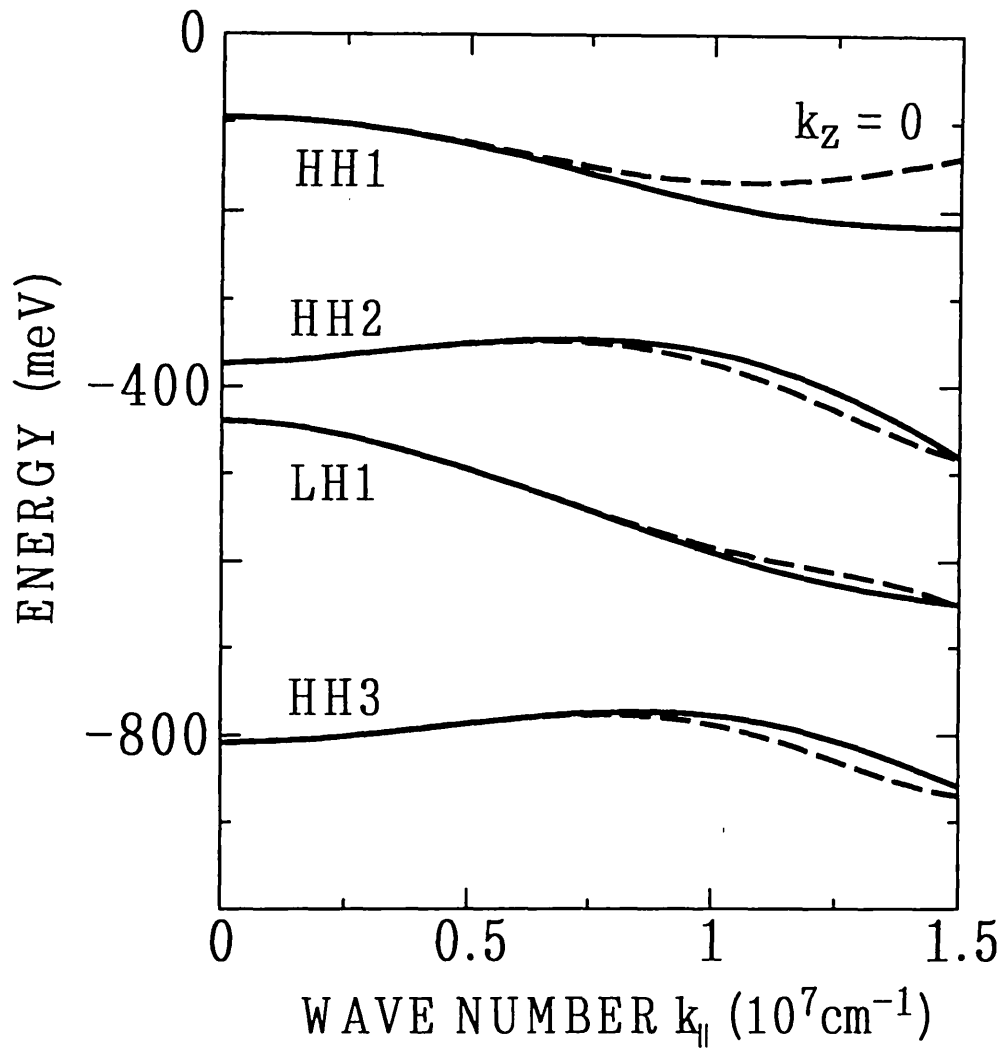


Fig. 8.4. The in-plane dispersions of valence subbands in the ZnTe(20Å)-ZnSe(20Å) SLS as a function of  $k_{||}$  for  $k_z=0$ . The solid and dashed lines represent subband energies in the [1,0] and [1,1] direction, respectively.

structure in the ZnTe-ZnSe SLS is that the dispersions of C2 and LH2 which exist above the barrier potentials are large. As in the ZnSe-ZnS SLS, the HH2 subband becomes higher than the LH1 subband also in the ZnTe-ZnSe SLS, reflecting the large shear deformation potential.

Figures 8.3 and 8.4 show the in-plane dispersion of the valence subband at  $k_z=0$  as a function of  $k_{\parallel}$  for ZnSe(20Å)-ZnS(20Å) and ZnTe(20Å)-ZnSe(20Å) SLSs, respectively. The solid and dashed curves correspond to the dispersion in the [1,0] and [1,1] direction, respectively. These figures confirm the isotropic feature of the in-plane dispersions in the valence subbands.

### 8.3 Characteristic differences between absorption spectra of Type I and Type II strained-layer superlattice

Figures 8.5 and 8.6, and Figs. 8.7 and 8.8 show the absorption spectra calculated for type I ZnSe(20Å)-ZnS(20Å) and type II ZnTe(20Å)-ZnSe(20Å) SLSs, respectively. Figures 8.5 and 8.7, and Figs. 8.6 and 8.8 show the absorption for  $P=TE$  and  $P=TM$ , respectively. (a) and (b) in these figures show the total and band-to-band absorption spectra, respectively. The graduations of a vertical line in all figures are the same. The absorption spectra for the type I SLS for both  $TE$  and  $TM$  seem rather normal, because they reflect the step-like density of states and increase roughly as  $\sqrt{E}$  as a function of energy  $E$ , while those for the type II SLS exhibit an unusual behavior, i.e. they increase rapidly as  $E^2$ . Origins of this sharp contrast are investigated in detail as follows.

The main difference between type I and type II SLSs is that the absorption in the ZnTe-ZnSe SLS is one order of magnitude less than that in the ZnSe-ZnS SLS. The

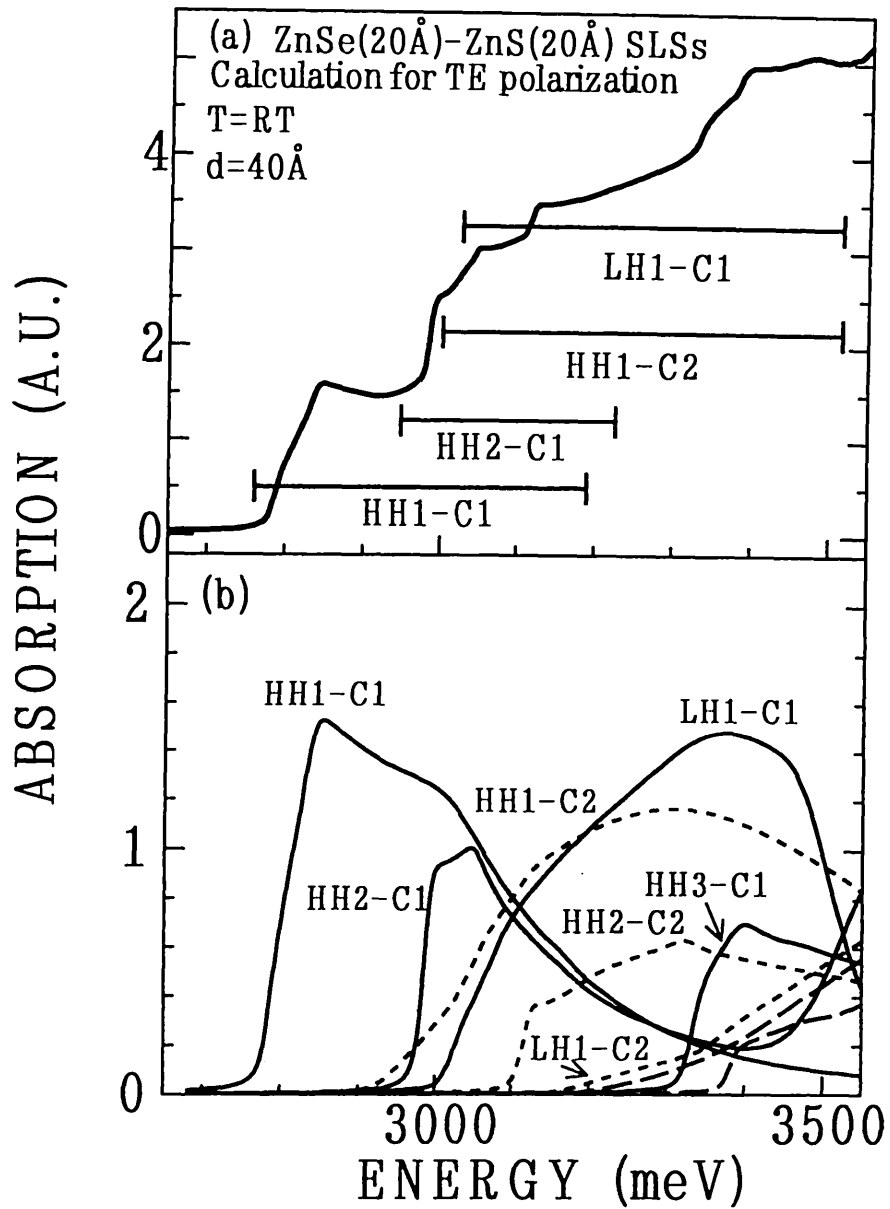


Fig. 8.5. Absorption spectra calculated for type I ZnSe(20Å)-ZnS(20Å) SLS for the *TE* incident-photon polarization. (a) and (b) correspond to the total and band-to-band absorption spectra.

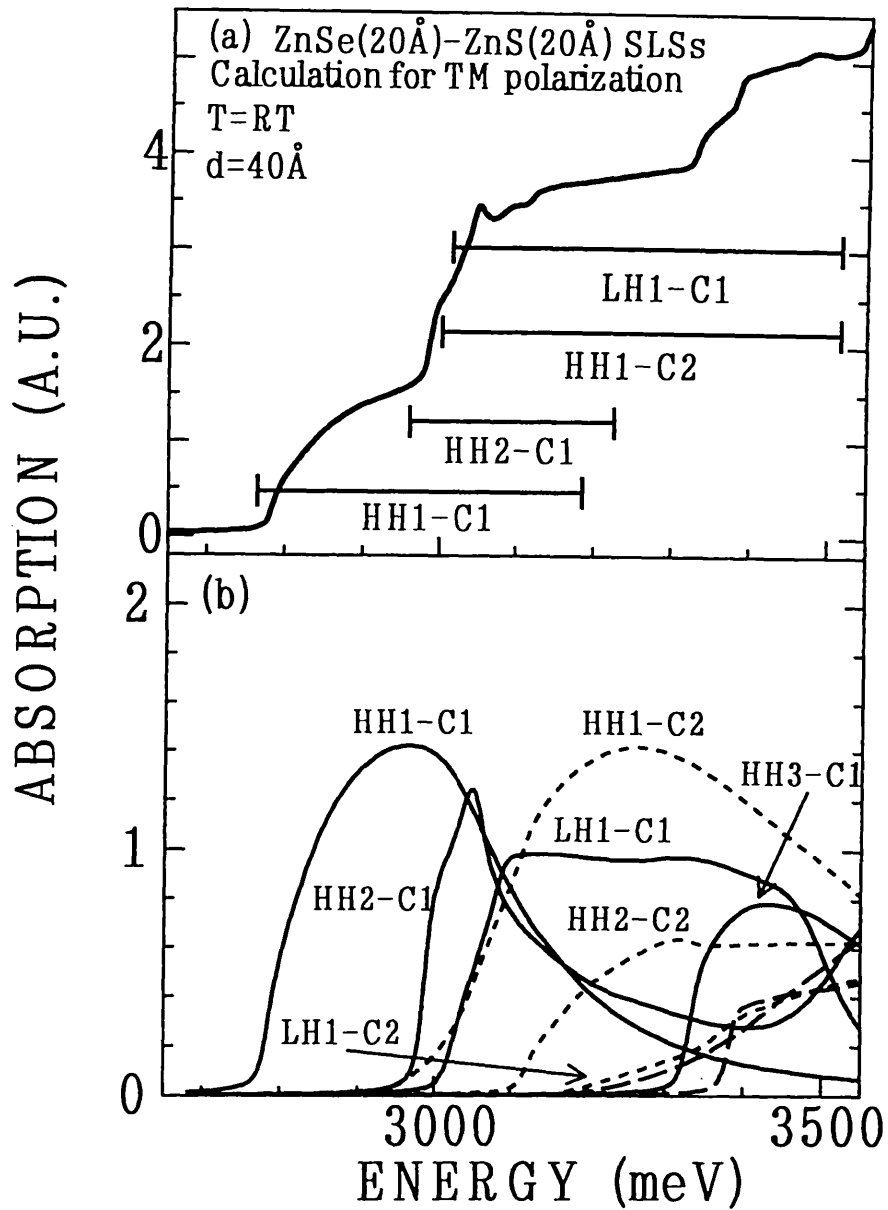


Fig. 8.6. Absorption spectra calculated for type I ZnSe(20Å)-ZnS(20Å) SLS for the *TM* incident-photon polarization. (a) and (b) correspond to the total and band-to-band absorption spectra.

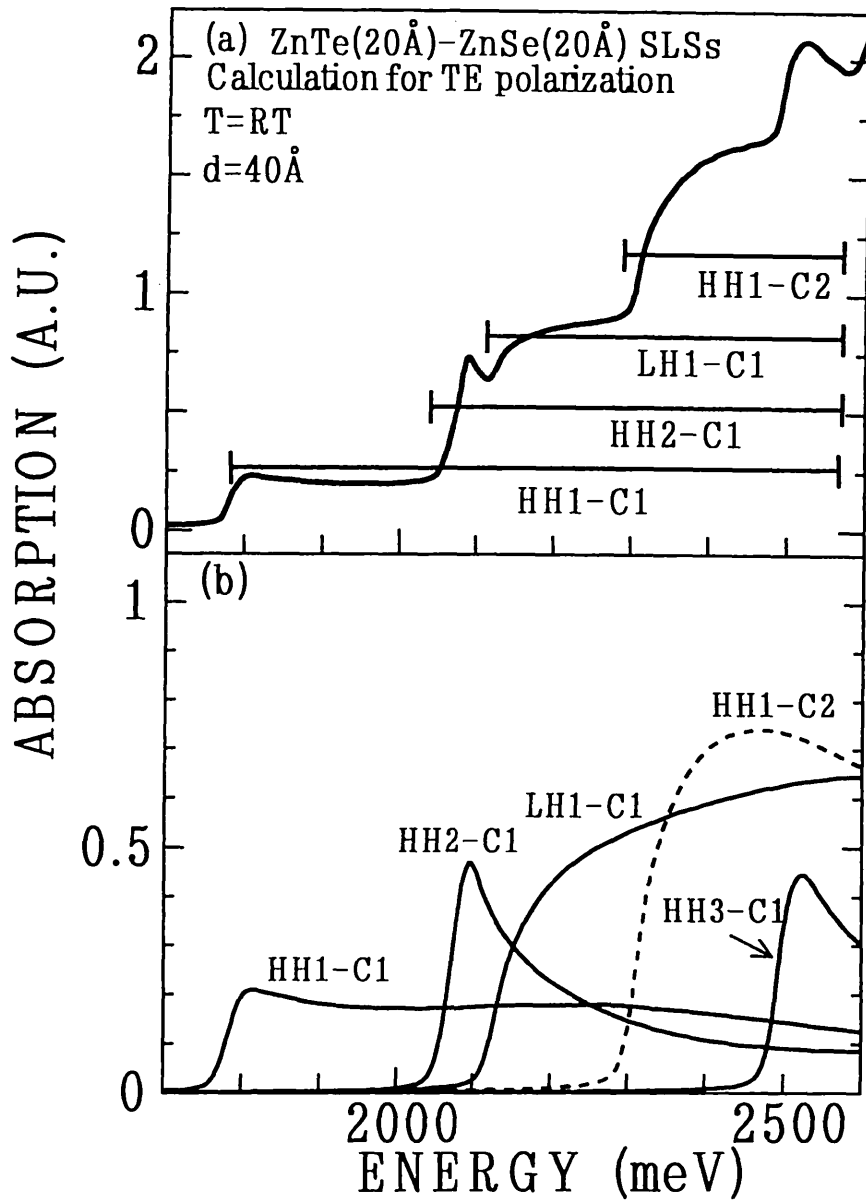


Fig. 8.7. Absorption spectra calculated for type II ZnTe(20Å)-ZnSe (20Å) SLS for the *TE* incident-photon polarization. (a) and (b) correspond to the total and band-to-band absorption spectra.

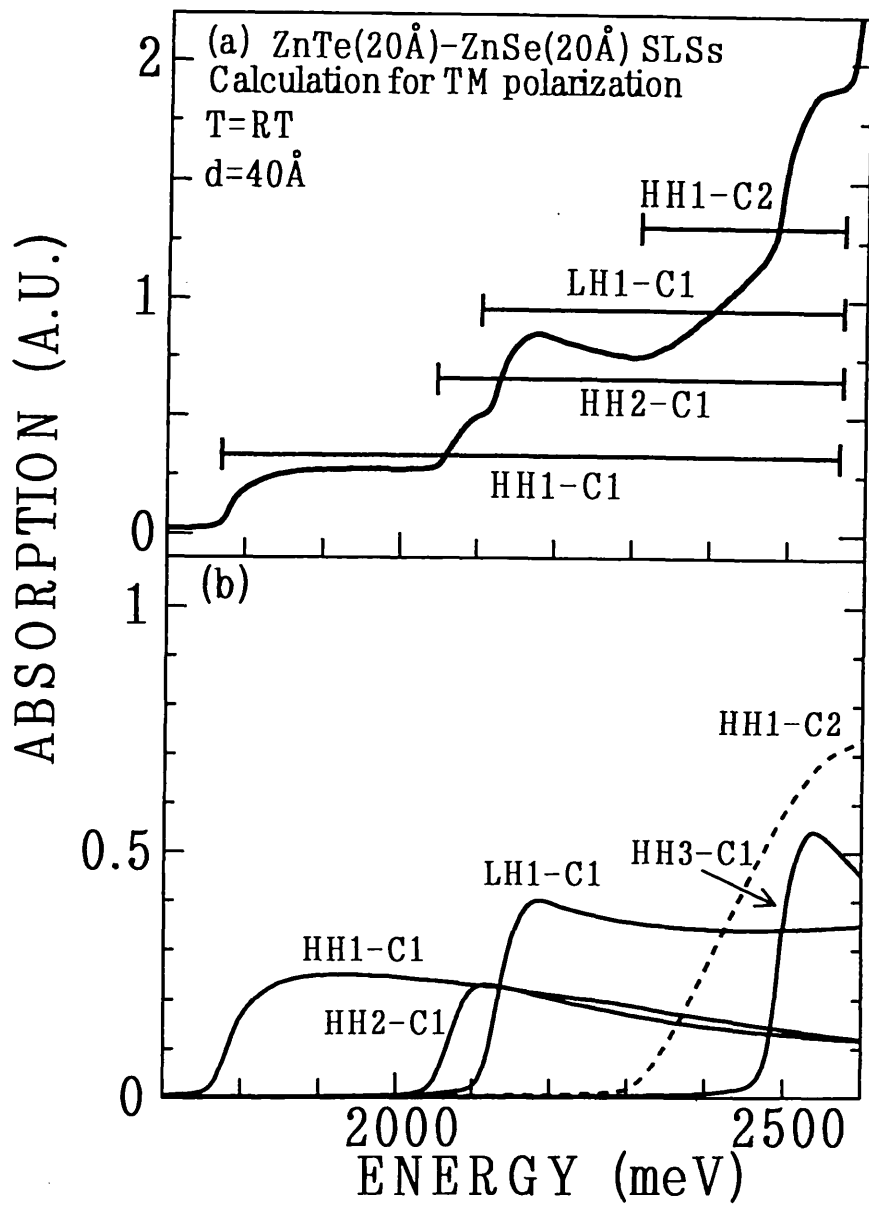


Fig. 8.8. Absorption spectra calculated for type II ZnTe(20Å)-ZnSe (20Å) SLS for the *TM* incident-photon polarization. (a) and (b) correspond to the total and band-to-band absorption spectra.

reason for this contrast is because in type II SLSs band-to-band transitions occur from the valence subbands in ZnTe well and ZnSe barrier layers to the conduction subbands in ZnTe barrier and ZnSe well layers, respectively, and are therefore weak.

Further, the ZnTe-ZnSe SLS has an interesting property. As compared with the band-to-band absorption spectra of the ZnSe-ZnS SLS in Figs. 8.5(b) and 8.6(b), those of the ZnTe-ZnSe SLSs in Figs. 8.7(b) and 8.8(b) show that the strength of  $HH_j-C_i$  and  $LH_j-C_i$  with the larger values of  $i$  and  $j$  is greater than that with the smaller values. This property is inherent to type II SLSs and opposite to that of type I SLSs, because the probability of finding an electron and a hole in the higher subband in barrier layers becomes larger than that in the lower subband, and thus the band-to-band transitions which involve higher subbands in barrier layers in type II SLSs are significantly intensified.

## 8.4 Dependence on the incident-photon polarization

Absorption spectra for  $TE$  and  $TM$  incident-photon polarizations have the characteristic difference. In  $TM$  polarization, the absorption spectra which consist of the transitions from heavy-hole state and from light-hole state stand up smoothly and sharply, respectively, while these characters are nearly inverse in  $TE$  polarization. The strength of band-to-band absorption spectra with the sharp onset is larger than that with the smooth one.

In the ZnSe-ZnS SLS, the polarization property appears in  $HH1-C1$ ,  $HH2-C1$  and  $LH1-C1$  absorption spectra remarkably. In the ZnTe-ZnSe SLS,  $HH1-C1$ ,  $HH2-C1$ ,  $LH1-C1$  and  $HH1-C2$  absorption spectra are influenced by polarization notably. Especially,  $HH2-C1$  and  $HH1-C2$  absorption spectra have a marked difference. Though

HH2-C1 absorption spectrum in  $TE$  polarization exist as a sharp peak, that in  $TM$  polarization becomes a smooth bump. HH1-C2 absorption spectra make total absorption spectra change significantly, and behave as if the main absorption transition did not exist in  $TM$  polarization.

## 8.5 Conclusions

The existence of novel properties in type II ZnTe-ZnSe SLSs has been predicted, i.e. there are two sharp contrasts between the absorption spectra of type I ZnSe-ZnS and type II ZnTe-ZnSe SLSs. One is that the absorption spectra of the ZnTe-ZnSe SLS is one order of magnitude less than those of the ZnSe-ZnS SLS, and the other is that the band-to-band transitions from the higher valence subbands and to the higher conduction subbands in the ZnTe-ZnSe SLS are enhanced significantly as compared with those in the ZnSe-ZnS SLS.

To confirm our predictions, optical measurements on these systems are highly desirable. By controlling these novel properties, it may be possible to design a new optical device based on type II SLSs whose characteristics are far different from those of an optical device designed by type I SLSs.

## Chapter 9 Conclusions

We have constructed a reliable theoretical method for an investigation of the optical absorption spectra of new SLSs. In this method, the optical absorption coefficient due to the direct valence-band-to-conduction-band transitions is derived on the basis of a detailed calculation of the electronic structure in an effective-mass approximation, and is evaluated carefully for the SLSs of type I and type II by taking explicitly the  $k$  dependence of the transition matrix into account. The calculation of the electronic structure of the conduction and valence subbands is carried out by using the Luttinger-Kohn Hamiltonian in the Kronig-Penney model, in which the periodic change of the effective mass and the strain in the well and barrier layers is taken into account.

The absorption spectrum is fully examined except for excitonic effects by an analysis of the mixing of the heavy- and light-hole states, and its dependence on the incident-photon polarization is also clarified. The SLSs treated by us are ZnSe-ZnS and ZnTe-ZnSe SLSs, which are type I and type II SLSs belonging to wide gap II-VI semiconductor, respectively, and have recently attracted our attention because of applicability to optoelectronic devices. The theoretical results have been compared with the recent experiments on ZnSe-ZnS and ZnTe-ZnSe SLSs by Shen *et al.*<sup>39,40)</sup> and Fan *et al.*,<sup>35)</sup> and it has been shown that these theoretical results agreed with the experimental results well. From these good agreements, we have predicted the characteristic differences between type I and type II SLSs, and have explored the possibility of new optical device.

In ZnSe(27Å)-ZnS(27Å) SLS, the calculated absorption spectra are compared with the experimental results by Shen *et al.*,<sup>39,40)</sup> and reproduces the overall features of the experimental result. One of the character of this SLS is that this SLS is influenced by

large strain effects where the calculated energy spacing between HH1 and LH1 sub-band states exceeds 200meV, and that the property is reflected in total absorption spectra. By means of decomposing the total absorption spectrum into the band-to-band absorption spectra, we assign the first observed line to the HH1-C1 transition. It is also clarified that the observed second absorption peak is composed of the transitions such as LH1-C1 and HH1-C2, and it is suggested that excitonic effects may give rise to a large enhancement of the absorption on the LH1-C1 transition. The mixing effects in the main HH1-C1 and LH1-C1 transitions contribute another swell in higher energy side (i.e. right shoulder) as well as initial start (i.e. left shoulder).

The characteristic differences between  $TE$  and  $TM$  incident-photon polarizations are determined mainly by HH1-C1 and LH1-C1 transitions. If a part of the absorption spectrum is mainly constructed by the transition from heavy-hole or light-hole state, its part of absorption spectrum is significantly intensified for  $TE$  or  $TM$  incident-photon polarization rather than for  $TM$  or  $TE$  incident-photon polarization, respectively. Therefore, experiments for the two different polarizations can provide a key to explore the nature of the optical absorption bands in ZnSe-ZnS SLSs.

As for ZnSe(22Å)-ZnS(23Å) SLS, the absorption spectra observed at RT by Fan *et al.*<sup>35)</sup> can be explained satisfactorily by the calculation of the absorption coefficients which takes the vertical valence-band-to-conduction-band transitions into account. In a high-energy side, however, there are some conspicuous discrepancies, which may be ascribed to the limitation of the effective-mass approximation and/or the neglect of the spin-orbit split-off bands. Though the dependence of incident-photon polarization and the effects of mixing between heavy- and light-hole states are also examined, these results are nearly similar to those in ZnSe(27Å)-ZnS(27Å) SLS.

For ZnTe(10Å)-ZnSe(10Å) SLS, the theoretical results have been compared with the recent experiments on the ZnTe-ZnSe SLS by Shen *et al.*,<sup>40)</sup> and have agreed with

the experimental results very well. It is suggested that the observed first and second absorption bumps may be ascribed to the HH1-C1 and LH1-C1 absorption spectra, respectively, and our theoretical result supports the validity of their assignment. The good agreement between theory and experiment also suggests that our theory may be applied for the substance with the strain effects which is larger than that of the ZnSe-ZnS SLS.

Marked differences of absorption spectra between  $TE$  and  $TM$  polarizations are not found in this particular system, because the barrier layer is very thin ( $10\text{\AA}$ ) and  $E_{cv}^{(n,m)}(\mathbf{k})$  depends on  $k_z$  strongly. If experimental studies are carried out on a thick barrier layer, substantial characters of the type II ZnTe-ZnSe SLSs will be observed. Because the absorption spectra calculated for ZnTe( $20\text{\AA}$ )-ZnSe( $20\text{\AA}$ ) SLS depend on incident-photon polarization. However, by changing our views, the fact that the polarization property of absorption spectra depends on layer thickness may give us a means to control the absorption spectra. This property would not depend on the kind of superlattice, since it depends on only layer thickness. In the future, we will examine this property.

$W_{nmj}(\mathbf{k})$  in HH1-C1 and LH1-C1 transitions depends on  $k_z$  largely in contrast to that of type I ZnSe-ZnS SLS, which is the property inherent in type II SLSs including the transition from well layer to barrier layer. This property results from the differences of the  $k_z$  dependence of parity between conduction-band and valence-band envelope functions in the same layer, and may make possible to design a new optical device on the basis of type II SLSs. In other words, by controlling the thickness of well and barrier layers,  $W_{nmj}(\mathbf{k})$  would change, and, also by controlling the number of period, the possibility to change  $W_{nmj}(\mathbf{k})$  would be got though the symmetry of space is destroyed a little.  $W_{nmj}(\mathbf{k})$  is made to change by means of using these methods, and this change is not uniform for each transition. Accordingly, by controlling the

number of period and the thickness of well and barrier layers, a special component of subband-to-subband absorption spectra may be intensified or weakened by the use of novel transition inherent in type II SLSs.

By taking account of the results for Chaps. 6 and 7, we have predicted characteristic differences in the absorption spectra at RT for both type I ZnSe(20Å)-ZnS(20Å) and type II ZnTe(Å)-ZnSe(20Å) SLSs in Chap. 8. We have revealed two marked characteristic differences between absorption spectra of type I ZnSe-ZnS and type II ZnTe-ZnSe SLSs. One is that the absorption spectra of the ZnTe-ZnSe SLS is one order of magnitude less than those of the ZnSe-ZnS SLS, and the other is that the band-to-band transitions from higher valence subbands and to the higher conduction subbands in the ZnTe-ZnSe SLS are enhanced significantly as compared with those in the ZnSe-ZnS SLS. If experiments are carried out for these system at RT, the results which we predict in this thesis will be confirmed. To confirm our predictions, optical measurements on these systems are, therefore, highly desirable. Further, these properties are also important to design a new optical device based on type II SLSs, if the control of these properties is realizable.

In above results, we have explored the absorption spectra for type I ZnSe-ZnS SLSs and type II ZnTe-ZnSe SLSs, and have got the interesting properties. As for common character in type I and type II SLSs, we have revealed that the difference of incident-photon polarization is strongly reflected in absorption spectra as the layer thickness is thickened. As for different character between type I and type II SLSs, we have found that properties of absorption spectra in type II SLSs were significantly different from those in the type I SLSs through the comparison for strength of  $W_{nmj}(\mathbf{k})$ , total absorption spectra and band-to-band absorption spectra. Though these properties in type II SLSs are likely to be difficult to treat, actually, these properties may be easy to use as optical device since these properties offer a means to change the strength

of absorption spectra. By controlling these novel properties, it also may be possible to design a new optical device based on type II SLSs whose characteristics are far different from those of an optical device designed by type I SLSs.

Though our theory has proved to be useful for investigating the origins of the experimental absorption spectra of typical new SLSs, it is far from complete in many respects. In particular, excitonic effects, quantitative evaluations of  $p_{cv}$  and the effect due to the spin-orbit split-pff state are not treated in this thesis. Theoretical studies on these important problems are now in progress.

# APPENDIX

## Appendix A Formalism of optical absorption coefficient

We suppose that the conduction band and the valence band consist of two states and four states, respectively. As the result, the wave functions are

$$\begin{aligned}\Psi_c^{(n)}(\mathbf{k}, \mathbf{r}) &= f_c^{(n)}(\mathbf{k}, \mathbf{r}) \sum_{i=1}^2 u_{ic}(\mathbf{r}) \\ &\equiv \sum_{i=1}^2 \varphi_{ic}^{(n)}(\mathbf{k}, \mathbf{r})\end{aligned}\tag{A.1}$$

and

$$\begin{aligned}\Psi_v^{(m)}(\mathbf{k}, \mathbf{r}) &= \sum_{j=1}^4 f_{jv}^{(m)}(\mathbf{k}, \mathbf{r}) u_{jv}(\mathbf{r}) \\ &\equiv \sum_{j=1}^4 \varphi_{jv}^{(m)}(\mathbf{k}, \mathbf{r}),\end{aligned}\tag{A.2}$$

which are shown in eqs.(4.2) and (4.4). Where  $f_c^{(n)}(\mathbf{k}, \mathbf{r})$  and  $f_{jv}^{(m)}(\mathbf{k}, \mathbf{r})$  are shown by eqs.(3.12) and (3.25), and  $u_{ic}(\mathbf{r})$  and  $u_{jv}(\mathbf{r})$  are shown by eqs.(4.1a)~(4.1b) and (4.3a)~(4.3d), respectively. The perturbation due to incident-photon is shown by

$$H' = \frac{i\hbar e}{2mc} A_0 [\hat{a}^\dagger e^{i\mathbf{k}\cdot\mathbf{r}} + \hat{a} e^{i\mathbf{k}\cdot\mathbf{r}}] (\boldsymbol{\pi}_l \cdot \nabla),\tag{A.3}$$

where

$$A_0 = \left( \frac{8\pi\hbar c^2}{\varepsilon V \omega_l} \right)^{\frac{1}{2}}.\tag{A.4}$$

$\omega_l$  is the frequency of photon, and  $\boldsymbol{\pi}_l$  is a unit vector which shows the direction of incident-photon polarization. We suggest that the optical transition consists of only

two states *i.e.*  $\varphi_{ic}^{(n)}(\mathbf{k}, \mathbf{r})$  and  $\varphi_{jv}^{(m)}(\mathbf{k}, \mathbf{r})$ . The transition matrix element is given by

$$\begin{aligned}
\lambda_{civj}^{(n,m)} &= \langle \varphi_{ic}^{(n)} | H' | \varphi_{jv}^{(m)} \rangle \\
&= \langle f_c^{(n)} u_{ic} | H' | f_{jv}^{(m)} u_{jv} \rangle \\
&= \frac{i\hbar e A_0}{2mc} \sum_l C_{cl}^{(n)*}(\mathbf{k}) C_{jvl}^{(m)}(\mathbf{k}) \int_{-\infty}^{\infty} d\mathbf{r} u_{ic}^*(\mathbf{k}, \mathbf{r}) \boldsymbol{\pi}_l \cdot (\nabla u_{jv}(\mathbf{k}, \mathbf{r})) \\
&= -\frac{e A_0}{2mc} \sum_l C_{cl}^{(n)*}(\mathbf{k}) C_{jvl}^{(m)}(\mathbf{k}) \boldsymbol{\pi}_l \cdot \mathbf{p}_{civj},
\end{aligned} \tag{A.5}$$

where

$$\begin{aligned}
\mathbf{p}_{civj} &= -i\hbar \int_{-\infty}^{\infty} d\mathbf{r} u_{ic}^*(\mathbf{k}, \mathbf{r}) \nabla u_{jv}(\mathbf{k}, \mathbf{r}) \\
&= \int_{-\infty}^{\infty} d\mathbf{r} u_{ic}^*(\mathbf{k}, \mathbf{r}) (-i\hbar \nabla) u_{jv}(\mathbf{k}, \mathbf{r}) \\
&= \int_{-\infty}^{\infty} d\mathbf{r} u_{ic}^*(\mathbf{k}, \mathbf{r}) \mathbf{p} u_{jv}(\mathbf{k}, \mathbf{r}) \\
&= \langle u_{ic} | \mathbf{p} | u_{jv} \rangle,
\end{aligned} \tag{A.6}$$

with  $\mathbf{p} = -i\hbar \nabla$ . The evaluation of  $\mathbf{p}_{civj}$  is straightforward and  $\mathbf{p}_{civj}$  is given by

$$p_{c1v1} = \frac{1}{\sqrt{2}} p'_{cv}(1, i, 0) \tag{A.7}$$

$$p_{c2v1} = 0 \tag{A.8}$$

$$p_{c1v2} = -\frac{2i}{\sqrt{6}} p'_{cv}(0, 0, 1) \tag{A.9}$$

$$p_{c2v2} = \frac{i}{\sqrt{6}} p'_{cv}(1, i, 0) \tag{A.10}$$

$$p_{c1v3} = \frac{1}{\sqrt{6}} p'_{cv}(1, -i, 0) \tag{A.11}$$

$$p_{c2v3} = \frac{2}{\sqrt{6}} p'_{cv}(0, 0, 1) \tag{A.12}$$

$$p_{c1v4} = 0 \tag{A.13}$$

$$p_{c2v4} = \frac{i}{\sqrt{2}} p'_{cv}(1, -i, 0). \tag{A.14}$$

Here we use the orthonormality of the spin states  $\alpha$  and  $\beta$ , and the fact that under the symmetry properties of the group  $O_h$ ,  $\langle s|p_x|X \rangle = \langle s|p_y|Y \rangle = \langle s|p_z|Z \rangle \equiv p'_{cv}$ , while such other matrix elements completely vanish.

As shown in Fig. A.1, we consider a relation between the coordinate axis  $(x,y,z)$  of superlattice grown along  $z$ -axis and  $\mathbf{k}$  which is taken in  $Z$  direction of Bloch basis shown by  $(X,Y,Z)$ . We use the following matrix including  $\theta$  and  $\phi$ , and transform  $(X,Y,Z)$ -axis into  $(x,y,z)$ -axis.

$$\begin{bmatrix} x \\ y \\ z \end{bmatrix} = - \begin{bmatrix} \cos \theta \cos \phi & \cos \theta \sin \phi & -\sin \theta \\ -\sin \phi & \cos \phi & 0 \\ \sin \theta \cos \phi & \sin \theta \sin \theta & \cos \theta \end{bmatrix} \begin{bmatrix} X \\ Y \\ Z \end{bmatrix} \quad (\text{A.15})$$

Then,  $p_{civj}$  in eqs.(A.7)~(A.14) are

$$p_{c1v1} = \frac{1}{\sqrt{2}} p'_{cv} (\cos \theta \cos \phi - i \sin \phi, \cos \theta \cos \phi + i \sin \phi, -\sin \theta) \quad (\text{A.16})$$

$$p_{c2v1} = 0 \quad (\text{A.17})$$

$$p_{c1v2} = -\frac{2i}{\sqrt{6}} p'_{cv} (\sin \theta \cos \phi, \sin \theta \sin \phi, \cos \theta) \quad (\text{A.18})$$

$$p_{c2v2} = \frac{i}{\sqrt{6}} p'_{cv} (\cos \theta \cos \phi - i \sin \phi, \cos \theta \sin \phi + i \cos \phi, -\sin \theta) \quad (\text{A.19})$$

$$p_{c1v3} = \frac{1}{\sqrt{6}} p'_{cv} (\cos \theta \cos \phi + i \sin \phi, \cos \theta \sin \phi - i \cos \phi, -\sin \theta) \quad (\text{A.20})$$

$$p_{c2v3} = \frac{2}{\sqrt{6}} p'_{cv} (\sin \theta \cos \phi, \sin \theta \sin \phi, \cos \phi) \quad (\text{A.21})$$

$$p_{c1v4} = 0 \quad (\text{A.22})$$

$$p_{c2v4} = \frac{i}{\sqrt{2}} p'_{cv} (\cos \theta \cos \phi + i \sin \phi, \cos \theta \sin \phi - i \cos \phi, -\sin \theta), \quad (\text{A.23})$$

and  $\lambda_{civj}^{(n,m)}$  is

$$\lambda_{civj}^{(n,m)} = g_{ij}(\theta, \phi) \lambda_{civj}^{(n,m)'} \quad (\text{A.24})$$

with

$$\lambda_{civj}^{(n,m)'} = -\frac{eA_0}{2mc} \sum_l C_{icl}^{(n)*}(\mathbf{k}) C_{jvl}^{(m)}(\mathbf{k}) p'_{cv} \quad (\text{A.25})$$

$(i = 1, 2 \quad j = 1, 2, 3, 4),$

and

$$g_{11}(\theta, \phi) = \frac{1}{\sqrt{2}} \{ \cos \gamma \cos \theta \sin \phi - \sin \gamma \sin \theta + i \cos \gamma \cos \phi \} \quad (\text{A.26})$$

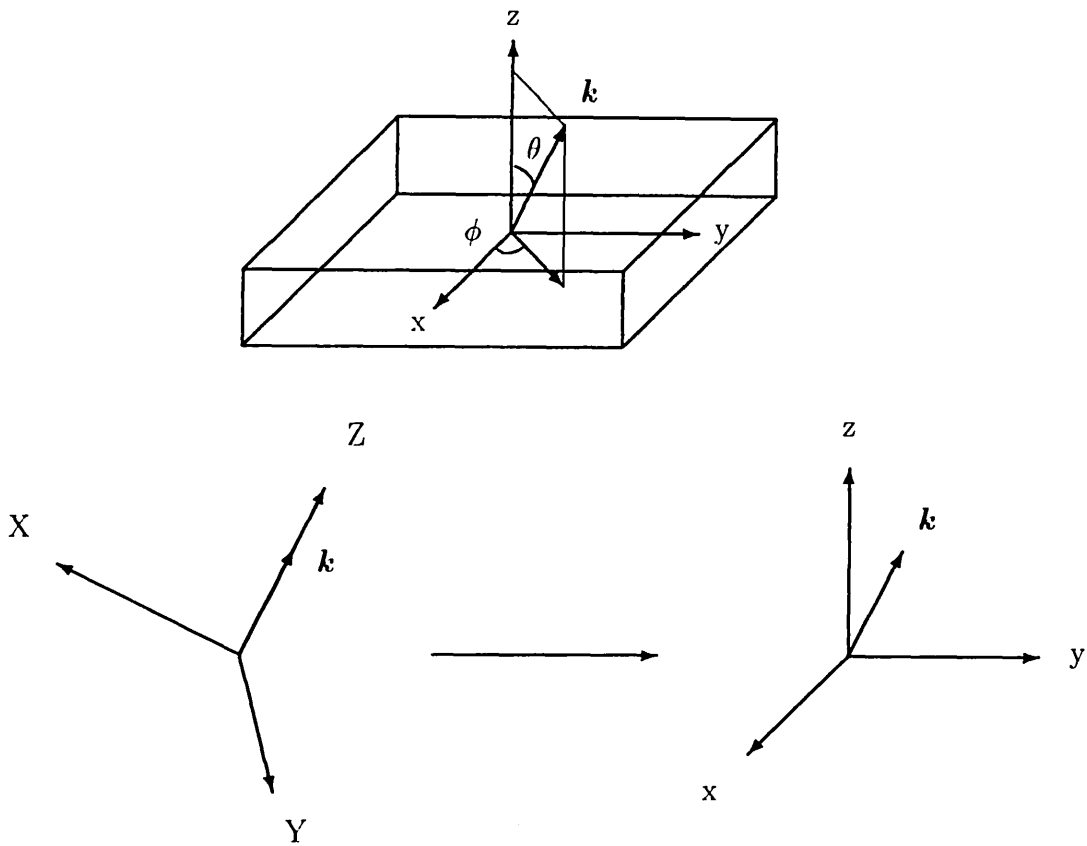


Fig. A.1. The circumstances transforming  $(X,Y,Z)$ -axis indicating Bloch basis into  $(x,y,z)$ -axis of superlattice grown along  $z$ -axis are shown.  $\theta$  and  $\phi$  represent parameters in sphere coordinate, and  $k$  is wave vector.

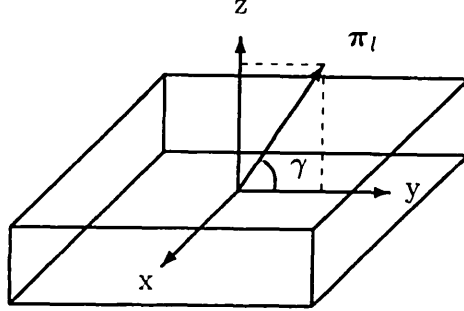


Fig. A.2.  $\gamma$  is an angle measured from  $y$ -axis in  $y$ - $z$  plane which is introduced to indicate incident-photon polarization, and an electric field vector of incident photon is selected in agreement with the direction of  $\pi_l$ .

$$g_{21}(\theta, \phi) = 0 \quad (\text{A.27})$$

$$g_{12}(\theta, \phi) = -\frac{2i}{\sqrt{6}} \{ \cos \gamma \sin \theta \sin \phi + \sin \gamma \cos \theta \} \quad (\text{A.28})$$

$$g_{22}(\theta, \phi) = \frac{i}{\sqrt{6}} \{ \cos \gamma \cos \theta \sin \phi - \sin \gamma \sin \theta + i \cos \gamma \cos \phi \} \quad (\text{A.29})$$

$$g_{13}(\theta, \phi) = \frac{1}{\sqrt{6}} \{ \cos \gamma \cos \theta \sin \phi - \sin \gamma \sin \theta - i \cos \gamma \cos \phi \} \quad (\text{A.30})$$

$$g_{23}(\theta, \phi) = \frac{2}{\sqrt{6}} \{ \cos \gamma \sin \theta \sin \phi + \sin \gamma \cos \theta \} \quad (\text{A.31})$$

$$g_{14}(\theta, \phi) = 0 \quad (\text{A.32})$$

$$g_{24}(\theta, \phi) = \frac{i}{\sqrt{2}} \{ \cos \gamma \cos \theta \sin \phi - \sin \gamma \sin \theta - i \cos \gamma \cos \phi \}. \quad (\text{A.33})$$

$\gamma$  is an angle measured from  $y$ -axis in  $y$ - $z$  plane which is introduced to indicate incident-photon polarization, and an electric field vector of incident photon is selected in agreement with  $\pi_l$ . The direction of  $\gamma$  is shown in Fig. A.2, and  $\gamma = 0$  (*i.e.*  $\pi_l = (0, 1, 0)$ ) and  $\gamma = \frac{\pi}{2}$  (*i.e.*  $\pi_l = (0, 0, 1)$ ) correspond to *TE* and *TM* incident-photon polarizations, respectively.

The Fermi's golden rule is shown by

$$W_{cvj}^{(n,m)} = \frac{2\pi}{\hbar} |\chi_{cvj}^{(n,m)}|^2 \delta(E_{cv}^{(n,m)}(\mathbf{k}) - \hbar\omega). \quad (\text{A.34})$$

Where we suppose that

$$|\chi_{c1vj}^{(n,m)'}|^2 = |\chi_{c2vj}^{(n,m)'}|^2 \equiv |\chi_{cvj}^{(n,m)'}|^2, \quad (\text{A.35})$$

and

$$|\chi_{cvj}^{(n,m)}|^2 = \{|g_{1j}(\theta, \phi)|^2 + |g_{2j}(\theta, \phi)|^2\} |\chi_{cvj}^{(n,m)'}|^2, \quad (\text{A.36})$$

and band gap between the  $n$ th conduction subband and  $m$ th valence subband for  $\mathbf{k}$  is given by

$$E_{cv}^{(n,m)}(\mathbf{k}) = E_g + E_c^{(n)}(\mathbf{k}) - E_v^{(m)}(\mathbf{k}). \quad (\text{A.37})$$

Here, total absorption coefficient  $\alpha^{P(\gamma)}(\omega)$  is given by summing over all of the individual band-to-band absorption coefficients  $\alpha_{nm}^{P(\gamma)}(\omega)$ , and shown by

$$\begin{aligned} \alpha^{P(\gamma)}(\omega) &= \sum_{nm} \alpha_{nm}^{P(\gamma)}(\omega) \\ &= \sum_{nm} \sum_j \alpha_{nmj}^{P(\gamma)}(\omega), \end{aligned} \quad (\text{A.38})$$

where  $P(\gamma)$  depending on  $\gamma$  indicates the direction of polarization for incident photon, and is simply replaced by  $P$  (i.e.  $P(\gamma) \equiv P$ ). By using eq.(A.34),  $\alpha_{nmj}^P(\omega)$  in eq.(A.38) is given by

$$\begin{aligned} \alpha_{nmj}^P(\omega) &= \frac{4\hbar}{\pi\epsilon\omega A_0^2} \sum_{k_z} \int d\mathbf{k}_{\parallel} W_{cvj}^{(n,m)} \\ &= \frac{4\pi e^2}{\epsilon m^2 c^2 \omega} \sum_{k_z} \int dk_{\parallel} k_{\parallel} \left| \sum_l C_{cl}^{(n)*}(\mathbf{k}) C_{jvl}^{(m)}(\mathbf{k}) \right|^2 \\ &\quad \times |p'_{cv}|^2 G_{P,j}(k_{\parallel}, k_z) \delta(E_{cv}^{(n,m)}(\mathbf{k}) - \hbar\omega), \end{aligned} \quad (\text{A.39})$$

where

$$G_{P,j=1,4}(k_{\parallel}, k_z) = \frac{1}{4} \left\{ \left(1 + \frac{k_z^2}{k^2}\right) \cos^2 \gamma + 2 \frac{k_{\parallel}^2}{k^2} \sin^2 \gamma \right\}, \quad (\text{A.40a})$$

$$G_{P,j=2,3}(k_{\parallel}, k_z) = \frac{1}{6} \left\{ \left(1 + \frac{3k_{\parallel}^2}{2k^2}\right) \cos^2 \gamma + \left(1 + \frac{3k_z^2}{k^2}\right) \sin^2 \gamma \right\}. \quad (\text{A.40b})$$

$\gamma=0$  (*i.e.*  $\boldsymbol{\pi}_l = (0, 1, 0)$ ) and  $\gamma=\frac{\pi}{2}$  (*i.e.*  $\boldsymbol{\pi}_l = (0, 0, 1)$ ) correspond to *TE* and *TM* incident-photon polarizations, respectively. When we consider *TE* and *TM* incident-photon polarizations,  $G_{Pj}$  in the absorption coefficient is given by

$$G_{TE,j=1,4}(k_{\parallel}, k_z) = \frac{1}{4} \left(1 + \frac{k_z^2}{k^2}\right), \quad (\text{A.41a})$$

$$G_{TE,j=2,3}(k_{\parallel}, k_z) = \frac{1}{6} \left(1 + \frac{3k_{\parallel}^2}{2k^2}\right), \quad (\text{A.41b})$$

for  $P=TE$ , and

$$G_{TM,j=1,4}(k_{\parallel}, k_z) = \frac{1}{2} \frac{k_{\parallel}^2}{k^2}, \quad (\text{A.42a})$$

$$G_{TM,j=2,3}(k_{\parallel}, k_z) = \frac{1}{6} \left(1 + \frac{3k_z^2}{k^2}\right), \quad (\text{A.42b})$$

for  $P=TM$ .

## Acknowledgments

The author would like to express his sincere gratitude to Professor Akira Hasegawa for continuous advices and encouragements throughout the course of this study. The author also would like to express his thanks to Professor Shin-ichi Katayama, Japan Advanced Institute of Science and Technology, for providing a opportunity to study the semiconductor superlattices.

The author is also sincerely grateful to Professors M. Goda, M. Kobayashi, H. Kaga and M. Azuma for their valuable advices and encouragements. The author is also sincerely grateful to Professor S. Tamaki for his encouragements. The author also gratefully acknowledges Dr. Y. Tanaka for his useful comments concerning magnetism. The author also gratefully acknowledges Dr. Y. Shirakawa for his continuous encouragements.

The author would like to express his thanks to Honary Professor Bun-iti Saito for guiding author's interest toward physical optics.

The author thanks all members of the physics of Niigata University for their valuable discussions and encouragements.

The numerical calculations were done on ACOS 2010 and CONVEX C3440 computers at the Information Processing Center, Niigata University.

## References

- 1) L. Esaki and R. Tsu: IBM Reserch Note RC-2418 (1969).
- 2) L. Esaki and R. Tsu: IBM J. Res. Dev. **14** (1970) 61.
- 3) D. Bohm: *Quantum Theory* (Prentice Hall, Englewood Cliffs, N.J. 1951),p.283.
- 4) R. Tsu and L. Esaki: Appl. Phys. Lett. **22** (1973) 562.
- 5) L. L. Chang, L. Esaki and R. Tsu: Appl. Phys. Lett. **24** (1974) 593.
- 6) L. Esaki and L. L. Chang: Phys. Rev. Lett. **33** (1974) 495.
- 7) L. L. Chang, H. Sakaki, C. A. Chang and L. Esaki: Phys. Rev. Lett. **38** (1977) 1489.
- 8) H. Sakaki, L. L. Chang, and L. Esaki: *Proc. 14-th Int. Conf. Phys. Semiconductors, Edinburgh, 1978*, ed. B. L. H. Wilson (The Institute of Physics, Bristol, 1978) p.737.
- 9) R. Dingle, W. Wiegmann and C. H. Henry: Phys. Rev. Lett. **33** (1974) 827.
- 10) R. Dingle, A. C. Gossard and W. Wiegmann: Phys. Rev. Lett. **34** (1975) 1327.
- 11) R. Tsu, A. Koma and L. Esaki: J. Appl. Phys. **46** (1975) 842.
- 12) R. Tsu, L. L. Chang, G. A. Sai-Halasz and L. Esaki: Phys. Rev. Lett. **34** (1975) 1509.
- 13) P. Manuel, G. A. Sai-Halasz, L. L. Chang C. Chang and L. Esaki: Phys. Rev. Lett. **37** (1976) 1701.

- 14) G. A. Sai-Halasz, A. Pinczuk, P. Y. Yu and L. Esaki: *Solid State Commun.* **25** (1978) 381.
- 15) R. M. Park, M. B. Troofer, C. M. Rouleau, J. M. DePuydt and M. A. Haase: *Appl. Phys. Lett.* **57** (1990) 2127.
- 16) A. Harwit, C. Hsu, F. Agullo-Rueda and L. L. Chang: *Appl. Phys. Lett.* **57** (1990) 1769.
- 17) T. Yokogawa: *Physica B* **191** (1993) 102.
- 18) Z. Yu, J. Ren, J. W. Cook Jr. and J. F. Schetzina: *Physica B* **191** (1993) 119.
- 19) I. S. Hauksson, S. Y. Wang, J. Simpson, M. R. Taghizadeh, K. A. Prior and B. C. Cavenett: *Physica B* **191** (1993) 124.
- 20) A. Tsujimura, S. Yoshii, S. Hayashi, K. Ohkawa, T. Mitsuyu and T. Takeishi: *Physica B* **191** (1993) 130.
- 21) A. Akimoto, H. Okuyama, T. Miyajima, Y. Morinaga, F. Hiei and M. Ozawa: *Physica B* **191** (1993) 133.
- 22) T. Taguchi, Y. Yamada, T. Ohno, J. T. Mullins and Y. Masumoto: *Physica B* **191** (1993) 136.
- 23) Doyeol Ahn: *Physica B* **191** (1993) 140.
- 24) J. P. Faurie, A. Million and J. Piagnet: *Appl. Phys. Lett.* **41** (1982) 713.
- 25) Y. Guldner, G. Basterd, J. P. Vieren, M. Voos, J. P. Faurie and A. Million: *Phys. Rev. Lett.* **51** (1983) 907.

- 26) H. Fujiyasu, A. Ishida, H. Kuwabara, S. Shinohara and H. Murase: *Surf. Sci.* **142** (1984) 579, and  
H. Fujiyasu, H. Takahashi, H. Shimizu, S. Sasaki and H. Kuwabara: *Proc. 17th Int. Conf. Physics of Semiconductors*, eds. J. D. Chadi and W. A. Harrison (Springer-Verlag, New York, 1985), p.539, and  
H. Fujiyasu, K. Mochizuki, Y. Yamazaki, M. Aoki, H. Kuwabara, Y. Nakanishi and G. Shimaoka: *Surface Sci.* **174** (1986) 543.
- 27) A. M. Glass, K. Tai, R. B. Byisma, R. D. Feldman, D. H. Olson and R. F. Austin: *Appl. Phys. Lett.* **53** (1988) 834.
- 28) H. Jeon, J. Ding, A. V. Nurmikko, H. Luo, N. Samarth, J. K. Furdina, W. A. Bonner and R. E. Nahory: *Appl. Phys. Lett.* **57** (1990) 2413.
- 29) M. A. Haase, J. Qiu, J. M. DePuydt and H. Cheng: *Appl. Phys. Lett.* **59** (1991) 1272.
- 30) H. Jeon, J. Ding, A. V. Nurmikko, W. Xie, D. C. Grillo, M. Kobayashi, R. L. Gunshur, G. C. Hau and N. Otuka: *Appl. Phys. Lett.* **60** (1992) 2045.
- 31) T. Yokogawa, M. Ogura and T. Kajiwara: *Appl. Phys. Lett.* **49** (1986) 1702.
- 32) H. Kuwabara and H. Fujiyasu: *J. Cryst. Growth* **72** (1985) 299.
- 33) A. Taike, N. Teraguchi, M. Konagai and K. Takahashi: *Jpn. J. Appl. Phys.* **26** (1987) L989.
- 34) F. Yang, P. J. Parbrook, K. P. O' Donnell, P. J. Wright and B. Cockayne: *Appl. Phys. Lett.* **59** (1991) 2142.

- 35) X. W. Fan, G. H. Fan, F. Y. Jiang and Z. P. Guan: *Proc. of Sino-Soviet Seminar, Spectroscopy and Optoelectronics in Semiconductors and Related Materials* (World Scientific, 1990), p.154.
- 36) Y. Kawakami, T. Taguchi and A. Hiraki: *J. Cryst. Growth* **93** (1988) 714.
- 37) T. Taguchi, Y. Kawakami and Y. Yamada: *Physica B* **191** (1993) 23.
- 38) Y. Yamada, Y. Masumoto, T. Taguchi and S. Takeda: *Proc. 20th Intern. Conf. on Physics of Semiconductors*, ed. E. M. Anastassakis and J. D. Joannopoulos (World Scientific, Singapore, 1990), p.941.
- 39) A. Shen, H. Wang, Z. Wang and S. Lü: *Appl. Phys. Lett.* **60** (1992) 21, and  
A. Shen, J. Cui, H. Wang and Z. Wang: *Superlattices and Microstructures* **12** (1992) 347.
- 40) A. Shen, L. Xu, H. Wang, Y. Chen, Z. Wang and A. Z. Li: *J. Cryst. Growth* **127** (1993) 383.
- 41) H. Yang, A. Ishida, H. Fujiyasu and H. Kuwabara: *J. Appl. Phys.* **65** (1989) 2838.
- 42) F. S. Turco-Sandroff, R. E. Nahory, M. J. S. P. Brasil, R. J. Martin, R. Beserman, L. A. Farrow, J. M. Worlock and A. L. Weaver: *J. Cryst. Growth* **127** (1991) 762.
- 43) N. Briot, T. Cloitre, O. Briot, B. Gil, D. Bertho, C. Jouanin, R. L. Aulombard, J. P. Hirtz and A. Huber: *J. Electron. Materials* **22** (1993) 537.
- 44) M. Kobayashi, N. Mino, H. Katagiri, R. Kimura M. Konagai and K. Takahasi: *J. Appl. Phys.* **60** (1986) 773, and

- M. Konagai, M. Kobayashi, R. Kimura and K. Takahasi: *J. Cryst. Growth.* **86** (1988) 290.
- 45) H. Hayashi and S. Katayama: *Phys. Rev. B* **39** (1989) 8743.
- 46) L. Quiroga, F. J. Rodríguez, A. Camacho and C. Tejedor: *Phys. Rev. B* **42** (1990) 11198.
- 47) T. Nakayama: *J. Phys. Soc. Jpn.* **61** (1992) 2434.
- 48) S. Hohnoki, S. Katayama and A. Hasegawa: *Solid State Commun.* **89** (1994) 41.
- 49) S. Hohnoki, S. Katayama and A. Hasegawa: *J. Phys. Soc. Jpn.* **63** (1994) 4082.
- 50) S. Hohnoki, S. Katayama and A. Hasegawa: *Jpn. J. Appl. Phys.* **34** suppl. 34-1 (1995) 65.
- 51) S. Hohnoki and A. Hasegawa: to be published in *J. Phys. Soc. Jpn.* **64** no.5.
- 52) J. M. Luttinger and W. Kohn: *Phys. Rev.* **97** (1955) 869.
- 53) J. M. Luttinger: *Phys. Rev.* **102** (1956) 1030.
- 54) M. Shinada and S. Sugano: *J. Phys. Soc. Jpn.* **21** (1966) 1936.
- 55) Y. Shinozuka and M. Matsuura: *Phys. Rev. B* **28** (1983) 4878.
- 56) R. L. Greene, K. K. Bajaj and D. E. Phelps: *Phys. Rev. B* **29** (1984) 1807.
- 57) J. A. Brum and G. Bastard: *J. Phys. C* **18** (1985) L789.
- 58) D. A. Broido and L. J. Sham: *Phys. Rev. B* **34** (1986) 3917.
- 59) T. Hiroshima: *Phys. Rev. B* **36** (1987) 4518.

- 60) M. M. Dignam and J. E. Sipe: Phys. Rev. B **41** (1990) 2865.
- 61) G. D. Sanders and Y.-C. Chang: Phys. Rev. B **35** (1987) 1300.
- 62) H. Chu and Y.-C. Chang: Phys. Rev. B **39** (1989) 10861.
- 63) N. F. Johson, H. Ehrenreich, P. M. Hui and P.M. Young: Phys. Rev. B **41** (1990) 3655.
- 64) N. F. Johson: J. Phys. Condens. Matter **2** (1990) 2099.
- 65) P.M. Young, P. M. Hui and H. Ehrenreich: Phys. Rev. B **44** (1991) 12969.
- 66) S.-C. Hong, G. P. Kothiyal, N. Debbar, P. Battacharya and J. Singh: Phys. Rev. B **37** (1988) 878.
- 67) J. W. Mathews and A. E. Blakeslee: J. Cryst. Growth **27** (1974) 118.
- 68) R. People and S. A. Jackson: *Strained-Layer Superlattices: Physics*, ed. T. P. Pearsall (Semiconductors and Semimetals, **32**, 1990), Chap.4 p.119
- 69) K. Oe, Y. Shinoda and K. Sugiyama: Appl. Phys. Lett. **33** (1978) 962.
- 70) I. J. Fritz, S. T. Picraux, L. R. Dawson and K. Sugiyama: Appl. Phys. Lett. **46** (1985) 967.
- 71) J. Saraie, N. Matsumura, M. Tsubokura K. Miyagawa and N. Nakamura: Jpn. J. Appl. Phys. **28** (1989) L108.
- 72) T. Yao: Optoelectronics-Devices and Technologies **6** (1991) 37.
- 73) J. Zou, D. J. H. Cockayne and B. F. Usher: J. Appl. Phys. **73** (1993) 619.

- 74) T. Ando and S. Mori: J. Phys. Soc. Jpn. **47** (1979) 1518, and  
T. Ando: J. Phys. Soc. Jpn. **54** (1985) 1528.
- 75) K. Shahzad, D. J. Olego, C. G. Van de Walle and D. A. Cammack: J. Luminescence **46** (1990) 109.
- 76) H. Fujiyasu and K. Mochizuki: J. Appl. Phys. **57** (1985) 2960.
- 77) H. Fujiyasu and K. Murase: Kotaibutsuri **21** no. 8 (1986) 469 [in Japanese].
- 78) Y. Kawakami, T. Taguchi and A. Hiraki: Kotaibutsuri **23** no. 7 (1988) 454 [in Japanese].
- 79) R. N. Bhargava: Optoelectronics-Devices and Technologies **7** (1992) 19.
- 80) R. C. Weast and R. B. Pamplin: *Handbook of Chemistry and Physics*, 57th ed. (CRC, OH, 1976) p.E-104.
- 81) B. Sermage and M. Voss: Phys. Rev. B **15** (1977) 3935.
- 82) A. Baldereschi and N. O. Lipari: Phys. Rev. B **3** (1971) 439.
- 83) F. T. J. Smith: Solid State Commun. **9** (1971) 957.
- 84) P. Lawaetz: Phys. Rev. B **4** (1971) 3460.
- 85) Y. K. Velikov and A. P. Rusukov: Fiz. Tverd. Tela. (Leningrad) **13** (1971) 1157 [Sov. Phys.-Solid State **13** (1972) 956].
- 86) D. Berlicourt, H. Jaffe and L. R. Shiozawa: Phys. Rev. **129** (1963) 1009.
- 87) Y. F. Tsay, S. S. Mitra and B. Bendow: Phys. Rev. B **10** (1974) 1476.

- 88) D. W. Langer, R. N. Euveman, K. Era and T. Koda: Phys. Rev. B **2** (1970) 4005.
- 89) M. Cardona: J. Appl. Phys. **32** (1961) 2151.
- 90) M. Cardona, K. L. Shaklee and F. H. Pollack: Phys. Rev. **154** (1967) 696.
- 91) W. H. Kleiner and L. M. Roth: Phys. Rev. Lett. **2** (1959) 334.
- 92) G. E. Pikus and G. L. Bir: Fiz. Tverd. Tela. **1** (1959) 1642. [Sov. Phys. -Solid State **1** (1959) 1502.]
- 93) J. C. Hensel and G. Feher: Phys. Rev. **129** (1963) 1041.
- 94) K. Suzuki and J. C. Hensel: Phys. Rev. B **9** (1974) 4184.
- 95) H. Hasegawa: Phys. Rev. **129** (1963) 1029.
- 96) G. C. Osbourn: J. Vac. Sci. Technol. B **1** (1983) 379.
- 97) C. G. Van de Walle and R. M. Martine: Phys. Rev. B **34** (1986) 5621.
- 98) R. A. Morrow and K. R. Brownstein: Phys. Rev. B **30** (1984) 678,  
R. A. Morrow and K. R. Brownstein: Phys. Rev. B **31** (1985) 1135, and  
R. A. Morrow: Phys. Rev. B **35** (1987) 8074.
- 99) D. J. BenDaniel and C. B. Duke: Phys. Rev. **152** (1966) 152.
- 100) T. Gora and F. Williams: Phys. Rev. **177** (1969) 1179.
- 101) D. Mukherji and B. R. Nag: Phys. Rev. B **12** (1975) 4338.
- 102) O. von Roos: Phys. Rev. B **27** (1983) 7547.

- 103) T. Ando and S. Mori: Surf. Sci. **113** (1982) 124.
- 104) A. Ishibashi, Y. Mori, K. Kaneko and N. Watanabe: J. Appl. Phys. **59** (1986) 4087.
- 105) K. B. Kahen and J. P. Leburton: Phys. Rev. B **33** (1986) 5465.
- 106) M. Altareli, U. Kenberg and A. Fasolino: Phys. Rev. B **32** (1985) 5138.
- 107) R. Eppenga, M. F. H. Schurmmas and S. Colak: Phys. Rev. B **36** (1987) 1554,  
and R. Eppenga and M. F. H. Schurmmas: Phys. Rev. B **37** (1988) 10923.
- 108) Z. Ikonić, V. Milanović and D. Tjapkin: Phys. Rev. B **46** (1992) 4285.
- 109) M. Asada, A. Kameyama and Y. Suematsu: IEEE. J. Quantum Electron. **QE-20** (1984) 745.
- 110) P. Voisin, G. Bastard and M. Voos: Phys. Rev. B **29** (1984) 935.